

UNIVERSITY OF CALIFORNIA

Los Angeles

Calculation of Conjugate Heat Transfer in a Heat Sink

Using Volume Averaging Technique (VAT)

**A thesis submitted in partial satisfaction of the
requirements for the degree Master of Science
in Mechanical Engineering**

by

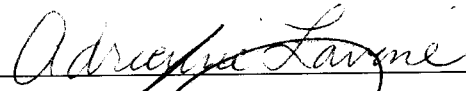
Andrej Horvat

2002

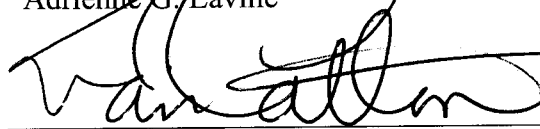
The thesis of Andrej Horvat is approved.



John Kim



Adrienne G. Lavine



Ivan Catton, Committee Chair

University of California, Los Angeles

2002

DEDICATION

To my father, who shaped my determination.

TABLE OF CONTENTS

List of Figures	vii
List of Tables	xi
List of Symbols	xii
Acknowledgements	xiv
Abstract	xv
I Introduction	1
I.1 Past Developments in Heat Exchanger Design.....	1
I.2 Generalization of Computational Approach.....	3
I.3 Volume Averaging Technique.....	4
I.4 Porous Media Flow Models.....	5
I.5 Heat Exchanger Thermal Effectiveness.....	7
I.6 Subject of Thesis Work.....	8
II Volume Averaging Technique	12
II.1 Fundamentals.....	13
II.2 Time and Space Derivatives.....	15
II.3 Convection Terms.....	16
II.4 Diffusion Terms.....	17
III Derivation of Separate Phase Porous Media Flow Equations	19
III.1 Mass Transport Equation.....	19
III.2 Momentum Transport Equation.....	20
III.3 Energy Transport Equation for Fluid.....	23
III.4 Energy Transport Equation for Solid.....	25
IV Experimental Test Section	27

V	Governing Equations for Uniform Flow within a Heat Sink	31
V.1	Momentum Transport in Fluid Flow.....	31
V.2	Energy Transport in Fluid Flow.....	32
V.3	Energy Transport in the Solid Structure.....	34
V.4	Energy Transport in the Solid Base.....	35
VI	Scaling Procedure for Governing Equations	37
VI.1	Scaling Factors.....	37
VI.2	Momentum Transport in Fluid Flow.....	38
VI.3	Energy Transport in Fluid Flow.....	39
VI.4	Energy Transport in the Solid Structure.....	41
VI.5	Energy Transport in the Solid Base.....	42
VII	Galerkin Solution Method	44
VII.1	Channel Flow.....	44
VII.2	Porous Media Flow.....	50
VIII	Finite Volume Solution Method	59
IX	Interphase Transfer Coefficients	64
IX.1	Drag Coefficient.....	64
IX.2	Heat Transfer Coefficient.....	65
X	Results	67
X.1	Comparison of Whole-Section Values.....	68
	X.1.1 Thermal Power 50 W.....	70
	X.1.2 Thermal Power 125 W.....	72
	X.1.2 Thermal Power 220 W.....	74
X.2	Temperature Distribution in Heat Sink.....	77
X.3	Surface Augmentation and Heat Transfer Enhancement.....	91
XI	Conclusions	99
	Appendix A Heat Sink Velocity and Temperature Fields, 50W	103
A.1	Velocity Fields.....	103
A.2	Temperature Fields.....	104

Appendix B Heat Sink Velocity and Temperature Fields, 125W	112
B.1 Velocity Fields.....	112
B.2 Temperature Fields.....	113
Appendix C Heat Sink Velocity and Temperature Fields, 220W	121
C.1 Velocity Fields.....	121
C.2 Temperature Fields.....	122
Appendix D Heat Transfer in Channel and Porous Media Flow	130
D.1 Velocity Fields.....	130
D.2 Temperature Fields.....	131
References	139

LIST OF FIGURES

II-1	Averaging over REV.....	12
IV-1	Experimental test section.....	27
IV-2	Pin-fins arrangement.....	28
X-1	Whole-section drag coefficient C_d , 50W of thermal power.....	70
X-2	Whole-section Nusselt number Nu , 50W of thermal power.....	71
X-3	Test section thermal effectiveness Q/W , 50W of thermal power.....	72
X-4	Whole-section drag coefficient C_d , 125W of thermal power.....	73
X-5	Whole-section Nusselt number Nu , 125W of thermal power.....	73
X-6	Test section thermal effectiveness Q/W , 125W of thermal power.....	74
X-7	Whole-section drag coefficient C_d , 220W of thermal power.....	75
X-8	Whole-section Nusselt number, 220W of thermal power.....	76
X-9	Test section thermal effectiveness Q/W , 220W of thermal power.....	76
X-10	Fluid velocity cross-section, $Q = 125W$, GM.....	78
X-11	Fluid velocity cross-section, $Q = 125W$, FVM.....	78
X-12	Temperature field in fluid (a) and in solid (b), $Re_h = 159$, $Q = 125W$, GM.....	79
X-13	Temperature field in fluid (a) and in solid (b), $Re_h = 159$, $Q = 125W$, FVM.....	80
X-14	Temperature field in fluid (a) and in solid (b), $Re_h = 253$, $Q = 125W$, GM.....	81
X-15	Temperature field in fluid (a) and in solid (b), $Re_h = 253$, $Q = 125W$, FVM.....	81
X-16	Temperature field in fluid (a) and in solid (b), $Re_h = 371$, $Q = 125W$, GM.....	82
X-17	Temperature field in fluid (a) and in solid (b), $Re_h = 371$, $Q = 125W$, FVM.....	83
X-18	Temperature field in fluid (a) and in solid (b), $Re_h = 543$, $Q = 125W$, GM.....	84
X-19	Temperature field in fluid (a) and in solid (b), $Re_h = 544$, $Q = 125W$, FVM.....	84
X-20	Temperature field in fluid (a) and in solid (b), $Re_h = 766$, $Q = 125W$, GM.....	85
X-21	Temperature field in fluid (a) and in solid (b), $Re_h = 768$, $Q = 125W$, FVM.....	86
X-22	Temperature field in fluid (a) and in solid (b), $Re_h = 1255$, $Q = 125W$, GM.....	87
X-23	Temperature field in fluid (a) and in solid (b), $Re_h = 1259$, $Q = 125W$, FVM.....	87

X-24	Temperature field in fluid (a) and in solid (b), $Re_h = 1593$, $Q = 125W$, GM.....	88
X-25	Temperature field in fluid (a) and in solid (b), $Re_h = 1598$, $Q = 125W$, FVM...	89
X-26	Temperature field in fluid (a) and in solid (b), $Re_h = 1861$, $Q = 125W$, GM.....	90
X-27	Temperature field in fluid (a) and in solid (b), $Re_h = 1868$, $Q = 125W$, FVM...	90
X-28	Fluid velocity cross-section in channel flow.....	92
X-29	Fluid velocity in heat sink.....	93
X-30	Temperature field at $Re_h = 379$ in channel flow; $Q = 0.358W$	94
X-31	Temperature field at $Re_h = 378$ in channel flow; $Q = 26.1W$	94
X-32	Heat flow Q , $T_{in} = 23^\circ C$ and $T_g = 30.3^\circ C$	95
X-33	Nusselt number Nu , $T_{in} = 23^\circ C$ and $T_g = 30.3^\circ C$	96
X-34	Thermal effectiveness Q/W , $T_{in} = 23^\circ C$ and $T_g = 30.3^\circ C$	97
A-1	Fluid velocity cross-section, $Q = 50W$, GM.....	102
A-2	Fluid velocity cross-section, $Q = 50W$, FVM.....	102
A-3	Temperature in fluid (a) and in solid (b), $Q = 50W$, $Re_h = 164$, GM.....	103
A-4	Temperature in fluid (a) and in solid (b), $Q = 50W$, $Re_h = 164$, FVM.....	103
A-5	Temperature in fluid (a) and in solid (b), $Q = 50W$, $Re_h = 258$, GM.....	104
A-6	Temperature in fluid (a) and in solid (b), $Q = 50W$, $Re_h = 258$, FVM.....	104
A-7	Temperature in fluid (a) and in solid (b), $Q = 50W$, $Re_h = 378$, GM.....	105
A-8	Temperature in fluid (a) and in solid (b), $Q = 50W$, $Re_h = 379$, FVM.....	105
A-9	Temperature in fluid (a) and in solid (b), $Q = 50W$, $Re_h = 554$, GM.....	106
A-10	Temperature in fluid (a) and in solid (b), $Q = 50W$, $Re_h = 555$, FVM.....	106
A-11	Temperature in fluid (a) and in solid (b), $Q = 50W$, $Re_h = 782$, GM.....	107
A-12	Temperature in fluid (a) and in solid (b), $Q = 50W$, $Re_h = 784$, FVM.....	107
A-13	Temperature in fluid (a) and in solid (b), $Q = 50W$, $Re_h = 1258$, GM.....	108
A-14	Temperature in fluid (a) and in solid (b), $Q = 50W$, $Re_h = 1261$, FVM.....	108
A-15	Temperature in fluid (a) and in solid (b), $Q = 50W$, $Re_h = 1585$, GM.....	109
A-16	Temperature in fluid (a) and in solid (b), $Q = 50W$, $Re_h = 1590$, FVM.....	109
A-17	Temperature in fluid (a) and in solid (b), $Q = 50W$, $Re_h = 1898$, GM.....	110
A-18	Temperature in fluid (a) and in solid (b), $Q = 50W$, $Re_h = 1904$, FVM.....	110
B-1	Fluid velocity cross-section, $Q = 125W$, GM.....	111

B-2	Fluid velocity cross-section, $Q = 125\text{W}$, FVM.....	111
B-3	Temperature in fluid (a) and in solid (b), $Q = 125\text{W}$, $Re_h = 159$, GM.....	112
B-4	Temperature in fluid (a) and in solid (b), $Q = 125\text{W}$, $Re_h = 159$, FVM.....	112
B-5	Temperature in fluid (a) and in solid (b), $Q = 125\text{W}$, $Re_h = 253$, GM.....	113
B-6	Temperature in fluid (a) and in solid (b), $Q = 125\text{W}$, $Re_h = 253$, FVM.....	113
B-7	Temperature in fluid (a) and in solid (b), $Q = 125\text{W}$, $Re_h = 371$, GM.....	114
B-8	Temperature in fluid (a) and in solid (b), $Q = 125\text{W}$, $Re_h = 371$, FVM.....	114
B-9	Temperature in fluid (a) and in solid (b), $Q = 125\text{W}$, $Re_h = 543$, GM.....	115
B-10	Temperature in fluid (a) and in solid (b), $Q = 125\text{W}$, $Re_h = 544$, FVM.....	115
B-11	Temperature in fluid (a) and in solid (b), $Q = 125\text{W}$, $Re_h = 766$, GM.....	116
B-12	Temperature in fluid (a) and in solid (b), $Q = 125\text{W}$, $Re_h = 768$, FVM.....	116
B-13	Temperature in fluid (a) and in solid (b), $Q = 125\text{W}$, $Re_h = 1255$, GM.....	117
B-14	Temperature in fluid (a) and in solid (b), $Q = 125\text{W}$, $Re_h = 1259$, FVM.....	117
B-15	Temperature in fluid (a) and in solid (b), $Q = 125\text{W}$, $Re_h = 1593$, GM.....	118
B-16	Temperature in fluid (a) and in solid (b), $Q = 125\text{W}$, $Re_h = 1598$, FVM.....	118
B-17	Temperature in fluid (a) and in solid (b), $Q = 125\text{W}$, $Re_h = 1861$, GM.....	119
B-18	Temperature in fluid (a) and in solid (b), $Q = 125\text{W}$, $Re_h = 1868$, FVM.....	119
C-1	Fluid velocity cross-section, $Q = 220\text{W}$, GM.....	120
C-2	Fluid velocity cross-section, $Q = 220\text{W}$, FVM.....	120
C-3	Temperature in fluid (a) and in solid (b), $Q = 220\text{W}$, $Re_h = 154$, GM.....	121
C-4	Temperature in fluid (a) and in solid (b), $Q = 220\text{W}$, $Re_h = 154$, FVM.....	121
C-5	Temperature in fluid (a) and in solid (b), $Q = 220\text{W}$, $Re_h = 247$, GM.....	122
C-6	Temperature in fluid (a) and in solid (b), $Q = 220\text{W}$, $Re_h = 247$, FVM.....	122
C-7	Temperature in fluid (a) and in solid (b), $Q = 220\text{W}$, $Re_h = 361$, GM.....	123
C-8	Temperature in fluid (a) and in solid (b), $Q = 220\text{W}$, $Re_h = 362$, FVM.....	123
C-9	Temperature in fluid (a) and in solid (b), $Q = 220\text{W}$, $Re_h = 530$, GM.....	124
C-10	Temperature in fluid (a) and in solid (b), $Q = 220\text{W}$, $Re_h = 531$, FVM.....	124
C-11	Temperature in fluid (a) and in solid (b), $Q = 220\text{W}$, $Re_h = 747$, GM.....	125
C-12	Temperature in fluid (a) and in solid (b), $Q = 220\text{W}$, $Re_h = 749$, FVM.....	125
C-13	Temperature in fluid (a) and in solid (b), $Q = 220\text{W}$, $Re_h = 1245$, GM.....	126

C-14	Temperature in fluid (a) and in solid (b), $Q = 220\text{W}$, $Re_h = 1248$, FVM.....	126
C-15	Temperature in fluid (a) and in solid (b), $Q = 220\text{W}$, $Re_h = 1594$, GM.....	127
C-16	Temperature in fluid (a) and in solid (b), $Q = 220\text{W}$, $Re_h = 1599$, FVM.....	127
C-17	Temperature in fluid (a) and in solid (b), $Q = 220\text{W}$, $Re_h = 1841$, GM.....	128
C-18	Temperature in fluid (a) and in solid (b), $Q = 220\text{W}$, $Re_h = 1847$, FVM.....	128
D-1	Fluid velocity cross-section in channel flow.....	129
D-2	Fluid velocity cross-section in porous media flow.....	129
D-3	Temperature field; channel flow (left), $Q = 0.266\text{W}$, $Re_h = 164$; porous media flow (b), $Q = 11.5\text{W}$, $Re_h = 164$	130
D-4	Temperature field; channel flow (left), $Q = 0.312\text{W}$, $Re_h = 256$; porous media flow (b), $Q = 18.1\text{W}$, $Re_h = 258$	131
D-5	Temperature field; channel flow (left), $Q = 0.358\text{W}$, $Re_h = 379$; porous media flow (b), $Q = 26.1\text{W}$, $Re_h = 378$	132
D-6	Temperature field; channel flow (left), $Q = 0.408\text{W}$, $Re_h = 553$; porous media flow (b), $Q = 37.3\text{W}$, $Re_h = 554$	133
D-7	Temperature field; channel flow (left), $Q = 0.467\text{W}$, $Re_h = 819$; porous media flow (b), $Q = 52.4\text{W}$, $Re_h = 812$	134
D-8	Temperature field; channel flow (left), $Q = 0.527\text{W}$, $Re_h = 1167$; porous media flow (b), $Q = 71.9\text{W}$, $Re_h = 1189$	135
D-9	Temperature field; channel flow (left), $Q = 0.605\text{W}$, $Re_h = 1741$; porous media flow (b), $Q = 96.4\text{W}$, $Re_h = 1742$	136
D-10	Temperature field; channel flow (left), $Q = 0.690\text{W}$, $Re_h = 2260$; porous media flow (b), $Q = 125.8\text{W}$, $Re_h = 2551$	137

LIST OF TABLES

IV-1	Pressure and heating power for experimental cases.....	30
V-1	Whole-section pressure drop Δp [Pa] at 50W, 125W and 220W.....	32
V-2	Inflow temperature T_{in} [°C] at 50W, 125W and 220W.....	34
V-3	Solid base bottom temperature T_g [°C] at 50W, 125W and 220W.....	36
X-1	Boundary conditions at heating power $Q = 50W$	67
X-2	Boundary conditions at heating power $Q = 125W$	67
X-3	Boundary conditions at heating power $Q = 220W$	68
X-4	Boundary conditions for channel flow calculations.....	91
X-5	Boundary conditions for heat sink flow calculations.....	92

LIST OF SYMBOLS

Latin letters

A	area, coefficient vector of the solution expansion
B	constants of energy equation for solid base-plate
c	specific heat
C	coefficient vector of the solution expansion
C_d	drag coefficient
d	diameter
D	constants of combined energy equation for fluid flow and solid structure
f	arbitrary function
F	constants of energy equation for fluid flow
FVM	finite volume method
g	arbitrary function
GM	Galerkin method
h	arbitrary function, heat transfer coefficient
H	height
I, J	matrices of integrals
K	linearized drag coefficient
L	length of the test section
m	mass flow
M	constants of momentum equation
Nu	Nusselt number
p	pressure, pitch between pin-fins
Pr	Prandtl number
Q	heat flow
Re	Reynolds number
REV	representative elementary volume
S	specific surface, constants of energy equation for solid structure
t	time
T	temperature
u	velocity in streamwise direction
U	velocity scale
v	velocity
V	volume
W	width of the test section, mechanical work
x	general spatial coordinate, streamwise coordinate
X	x -direction part of the solution
y	horizontal spanwise coordinate

z	vertical spanwise coordinate
Z	z -direction part of the solution

Greek letters

α	volumetric fraction
β	arbitrary scalar, solution eigenvalue
γ	solution coefficient
Δ	finite difference
λ	thermal diffusivity
Λ	area of integration
μ	dynamic viscosity
ν	kinematic viscosity
ρ	density
Ω	cell volume

Subscript/Superscript

b	base
c	contact flow area of the test section
f	fluid phase
g	ground, $z = -H_b$ position
h	hydraulic diameter
k	phasic variable
i, j, n, m	indexes
if	bottom, $z = 0$ position
in	inflow, $x = 0$ position
o	interphase variable
out	outflow
s	solid phase
x	streamwise direction
y	horizontal spanwise direction

Symbols

$\langle \rangle$	expression "interphase average"
'	discrepancy from the intraphase average
-	intraphase average
^	dimensional form of variables
\perp	perpendicular to the flow in channel

ACKNOWLEDGEMENTS

First I would like to thank Prof. Dr. Ivan Catton of University of California, Los Angeles for his guidance and long discussions. I am also grateful to Prof. Dr. Borut Mavko of Institute "Jožef Stefan", Ljubljana, for professional support.

My stay and work at University of California, Los Angeles would not be possible without a financial support received from the Kerze-Cheyovich scholarship and the Ministry of Education, Science and Sport of RS, which is gratefully acknowledged. I would also like to acknowledge the DARPA HERETIC program for its support of research at UCLA in the area of heat sink optimization.

At the end I would like to thank my wife Fitri, who carried the burden when things went wrong.

ABSTRACT OF THE THESIS

Calculation of Conjugate Heat Transfer in a Heat Sink

Using Volume Averaging Technique (VAT)

by

Andrej Horvat

Master of Science in Mechanical Engineering

University of California, Los Angeles, 2002

Professor Ivan Catton, Chair

A fast running computational algorithm based on Volume Averaging Technique (VAT) is developed and solutions obtained using the Finite Volume Method (FVM) and the Galerkin Method (GM). The goal is to improve computational capability in the area of heat exchangers and help eliminate some of the empiricism involved in their design that leads to overly constrained designs with resulting economic penalties.

VAT is tested and applied to a simulation of air-flow through an aluminum (Al) chip heat sink. Using VAT, the computational algorithm is fast running, but still able to

present a detailed picture of temperature fields in the air-flow as well as in the solid structure of the heat sink. The calculated whole-section drag coefficient, Nusselt number and thermal effectiveness were compared with the experimental data to verify the computational model and validate numerical code. The comparison also shows a good agreement between GM and FVM results although different thermal boundary conditions at the bottom were used.

The constructed computational algorithm enables prediction of cooling capabilities for the selected geometry. It also offers possibility for geometry improvements and optimization, to achieve higher thermal effectiveness.

I. Introduction

Heat exchangers are found in a number of different industrial sectors where need to transport heat from media to media exists. They also have an important role in everyday life as they are one of the basic elements of heating, cooling, refrigerating and air-conditioning installations.

Despite the crucial role of heat exchangers, there is still a lot of empiricism involved in their design. Although present guidelines provide an ad-hoc solution to the design problems, at present, a unified approach based on simultaneous modeling of thermal hydraulics and structural behavior has not been developed and utilized. As a consequence, designs are overly constrained with a resulting economic penalty. Therefore, the optimization of a heat exchanger design can bring significant cost reduction to industry.

The objective of the thesis is to develop a unified fast running numerical algorithm for the calculation of heat exchanger morphologies using hierarchic modeling of the coolant thermal hydraulics as well as the thermal behavior of the structure.

I.1 Past Developments in Heat Exchanger Design

In the past heat exchanger development was clearly dominated by interests of

the military and power industries (Kays and London, 1998). As the amount of heat transported through the heat exchangers is highest in nuclear installations, steam generators and heat exchangers in nuclear power reactors have been the focus of researchers' attention and the reason why the most experimental work was done with isothermal circular tubes (Lauder and Massey, 1978, Johnson et al., 1983, Fujii et al., 1984, Noghrehkar et al. 1999, Žukauskas, 1972 and 1987, Žukauskas and Ulinskas, 1985 etc.). Although some of the work is very comprehensive (Žukauskas, 1972 and 1987), most of these studies favored a circular geometry and did not include any other form of internal structures.

The emphasis was on the experimental work because of the absence of today's powerful computers and lack of suitable numerical methods (Antonopoulos, 1979, Barsamian and Hassan, 1997). The nature of experimental work limited researchers to study only a few heat exchanger geometries and few variations in their geometry parameters. Furthermore, the flow conditions were often limited by available experimental setups. These disadvantages, compared to numerical modeling, did not allow researchers to explore a wide range of parameters in order to find an optimal geometry. They rather limited the engineer's choices to well-tested and proven designs.

During the past few years, the electronics industry has been demanding more and more efficient heat exchanger designs. In particular, the speed of electronic chips is seriously bounded by the thermal power that the chips produce. As a consequence,

electronic chips have to be intensively cooled using specially designed heat exchangers submerged into air or water flow (Al-Jamal and Khashashneh, 1998, Bejan, 1995, Bejan and Sciubba, 1992, Fabbri, 1999, Ledezma and Bejan, 1996, Yüncü and Anbar, 1998).

Partly due to described technological needs and partly due to extraordinary dynamics of computer industry, state-of-the-art knowledge of fluid dynamics and heat transfer have been employed to design cooling structures (Bejan, 1995, Bejan and Sciubba, 1992). Besides the classical forms of heat exchanging surfaces, advanced forms originating mostly from aerospace applications have also been used (Fabbri, 1999, Ledezma and Bejan, 1996). In contrast to the latter case, where the heat exchanging structures are isothermal (Horvat and Catton, 2001), the heat exchangers in electronic industry consist mostly of heat conducting materials. This further complicates numerical calculations as well as experimental work due to the conjugate nature of heat transfer (Horvat et al., 2002).

I.2 Generalization of Computational Approach

The wide spread use of heat exchangers across many industrial sectors has caused their development to take place in a piecemeal fashion in a number of rather unrelated areas. Much of the technology, familiar in one sector, moved only slowly over the boundaries into another sector (Hesselgreaves, 2001).

To overcome historic differences, a unified description for fluid and heat flow through a solid matrix has to be found. One of the suitable options is Volume Averaging Technique (VAT), where transport processes in a heat exchanger are modeled as a porous media flow (Travkin and Catton, I., 1995, Horvat et al., 2002). This generalization allows us to unify the heat transfer calculation techniques for different kinds of heat exchangers and their structures. The case-specific geometrical arrangements, material properties and fluid flow conditions enter the computational algorithm only as series of precalculated coefficients. This clear separation between the model and the case-specific coefficients simplifies the procedures for determining the optimum heat transfer conditions.

I.3 Volume Averaging Technique

In this work attention will be focused on volume averaging and on the underlying Volume Averaging Technique (VAT). Applying VAT, the flow variables are averaged over a Representative Elementary Volume (REV). The variations, which are smaller than the averaged volume, have to be modeled separately in a form of closure models. Although the details of the modeled flow are lost due to the averaging procedure, the hierarchical modeling principle of VAT represents a theoretically rigorous methodology for simulation of multi-component flow systems. Porous media flows, which are the subject of this thesis, are only one representation of such systems.

VAT was initially proposed in the 1960s by Anderson and Jackson (1967), Slattery

(1967), Marle (1967), Whitaker (1967), and Zolotarev and Redushkevich (1968). Many of the important details and examples of applications can be also found in books by Dullien (1979), Kheifets and Neimark (1982), and Adler (1992). The method was expanded to problems of turbulent transport in porous media by Primak et al. (1986), Sheherban et al. (1986), Travkin et. al (1993, 1994, 1999) and Travkin and Catton (1992, 1994, 1995). Travkin and Catton (1999) also worked further on development of VAT for heterogeneous media applicable to nonlinear physical phenomena in thermal science and fluid mechanics. Their mathematically strict derivation of separate phase porous media transport equations also represents the theoretical foundation of this thesis.

An example of VAT applied to heat exchanger calculations was given by Nelson and Bejan (1998), where they tried to obtain an optimized heat transfer point. Hu (2001), in his thesis, showed a calculation of flow in a channel across square tube banks. Horvat and Catton (2001) collected experimental results and demonstrated that for cross-flow in heat exchangers with circular tubes, VAT can give accurate results. In addition, the application of VAT was further extended to conjugate heat transfer problems by Horvat et al. (2002).

I.4 Porous Media Flow Models

Calculation of fluid and heat flow variables in a heterogeneous media is a demanding task. Although direct numerical simulation of transport phenomena in each

material phase (or component) is theoretically possible, it demands enormous computational resources even for simple geometries. This is the reason why direct approaches are rarely seen in practical engineering applications.

In order to resolve most of the flow features and at the same time keep the model simple enough to serve as an engineering tool, an averaging of fluid and heat flow variables has to be performed. Although different averaging procedures are possible (e.g. spatial, time, or ensemble averaging), their goal is to smear out heterogeneities in flow variables. Due to such averaging procedure, the resulting transport equations are not closed. To solve them, it requires an introduction of additional porous media flow models.

The first, and most-well known, porous media flow model was introduced by Darcy in 1856, when he investigated the hydrology of the fountains in Dijon, France (Niedl and Bejan, 1992). He linearly related pressure drop with flow velocity using dynamic viscosity and specific permeability as two additional constants. Darcy's law has been verified by a number of results and different experiments. Theoretical backing for it has been obtained in various ways with the aid of either deterministic or statistical models (e.g. Whitaker, 1986).

Darcy's linear relation holds when flow velocity is small. In practice this means that the related Reynolds number, based on a typical pore or particle diameter, is of order

unity or smaller. As velocity increases the transition to nonlinear drag is quite smooth; there is no sudden transition. Due to drag non-linearity, the quadratic term, often referred as Forchheimer term, is added to Darcy's relation (Joseph et al., 1982). An alternative to Darcy's model is what is commonly known as Brinkman's model, where additional viscous term in the form of Laplacian of velocity is added to the momentum transport equation. Nevertheless, it has to be noted that experimental checks of Brinkman's theory have been indirect and few in number (Nield and Bejan, 1992).

In the present work a quadratic relation is used for the momentum equation closure and a linear relation for the energy equation closure. The form of the equations does not differ much from the known models (Darcy's, Forchheimer's or Brinkman's model), although the meaning of the introduced closure relations and the techniques to treat them are significantly changed. Namely, empirical model constants are replaced with mapped parametric values. These parametric values are Reynolds number dependent, which brings additional flexibility in presented model approach.

I.5 Heat Exchanger Thermal Effectiveness

The design of a heat exchanger involves consideration of both the heat transfer rates and the mechanical pumping power expended to overcome fluid friction and move the fluids through the heat exchanger. For a heat exchanger operating with high-density fluids, the friction-power expenditure is generally small relative to the heat transfer rate.

This means that the friction-power expenditure is seldom a controlling influence. However, for low-density fluids, such as gases, it is very easy to expend as much mechanical energy in overcoming friction as the amount of transferred heat (Kays and London, 1998).

The quality of a heat exchanger is defined with a thermal effectiveness defined as the ratio between transferred heat and mechanical energy needed for coolant transport. This means that a higher quality heat exchanger will transfer more heat from one media to another for the same amount of mechanical energy spent to move the fluid. Keeping this criterion in mind, the selection of heat exchangers as well as the regime of operation becomes a very sensitive issue.

Although the lower velocities bring higher effectiveness, the resulting low heat transfer rates have to be compensated with a larger heat transfer surface and consequently with a larger size of a heat sink. In some cases this is not possible due to economics and size limitations.

I.6 Subject of Thesis Work

Due to its importance, the design of heat exchangers is a well-studied subject. Nevertheless, the proposed Volume Averaging Technique (VAT), which is based on rigorous scientific methodology, has rarely been applied to conjugate heat transfer

problems in heat exchangers. Therefore, this thesis presents the VAT formulation and solution of conjugate heat transfer problem for an aluminum (Al) heat sink used as a cooling device.

In order to understand the separate phase porous media flow model and the solutions to the conjugate problem, the VAT used to average the transport equations has to be presented in details. Therefore, chapter II explains the fundamentals of Volume Averaging Technique (VAT) and the derivation of the gradient, convection and diffusion terms.

In chapter III, the VAT procedure is applied to the transport equations to obtain the separate phase porous media flow equations. This chapter presents derivation of mass, momentum and energy transport equations for fluid and solid phase.

The results from numerical simulations are compared with experimental data taken in the Morrin-Martinelli-Gier Memorial Heat Transfer Laboratory at University of California, Los Angeles. Chapter IV presents the geometry and the boundary conditions of the experimental test section. Later described numerical models are used to capture basic features of the experiments.

Based on the derivation of separate phase porous media flow equations, chapter V describes the derivation of governing equations for uniform flow through the examined

heat sink. Together with the dimensional form of the equations, the boundary conditions are given for all simulated cases.

In order to be able to apply the same numerical methods for calculation of heat transfer processes in the heat sink and the channel flow, the transport equations and their boundary conditions are transformed into dimensionless form as described in chapter VI.

Chapter VII presents Galerkin method (GM), which is used to solve semi-analytically two-dimensional heat transfer problem in the channel as well as in the heat sink. Full three-dimensional heat transfer problem is solved with Finite Volume Method (FVM) as described in chapter VIII.

As the flow and heat transfer behavior fundamentally depends on exchange of momentum and heat between the solid and fluid phase, the selection of interphase transfer coefficients (i.e. drag and heat transfer coefficients) has to be very careful. Chapter IX reveals sources of the experimental data and correlations for drag and heat transfer coefficients, which are introduced in the calculations.

The results of the performed simulations are summarized in chapter X. The first part of the chapter presents the comparison of the whole-section drag coefficient, Nusselt number and thermal effectiveness for experimental data, GM and FVM results. Further, detailed distributions of temperature in air-flow and solid structure are given for different

Reynolds numbers. It is also explained, how increasing Reynolds number influences the developed temperature field and consequently the heat transfer processes in the heat sink. The last part of chapter X compares the channel flow and heat sink results obtained at the same Reynolds number. Such comparison explains the influence of surface augmentation on heat transfer enhancement.

In conclusions, the summary of the performed work is given. It also describes the most important achievements of my thesis work.

II. Volume Averaging Technique

Fluid-structure interactions and heat transfer in a heat exchanger can be described by basic mass, momentum and heat transport equations. For a model to have short computing times, the transport equations are averaged over a Representative Elementary Volume (REV) as presented in Fig. 1.

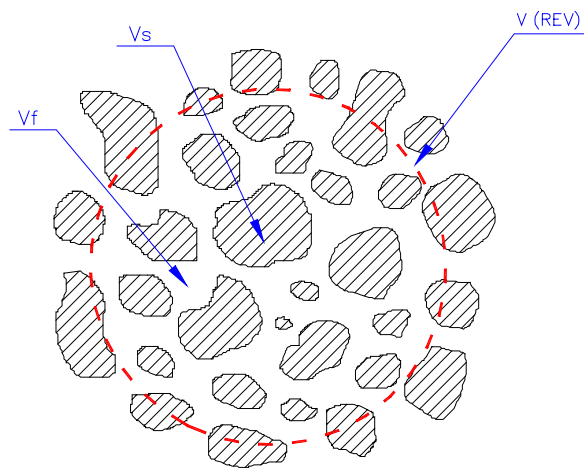


Figure II-1: Averaging over REV.

The method is known as Volume Averaging Technique (VAT) and produces separate phase porous media flow equations (Travkin and Catton, 1999). To understand later heat exchanger modeling and its solutions, the theoretical foundations of VAT are given in this chapter.

Although porous media flow is a representation of multicomponent flows, the expression "multiphase" will be used in order to be consistent with descriptions of more general numerical methods.

II.1 Fundamentals

In the present work, the phase k volume fraction is defined as the ratio between the portion of the REV occupied by phase k and the total REV:

$$\alpha_k = \frac{V_k}{V} . \quad (\text{II.1})$$

In the following developments, two kinds of averaging are used. If the variable h , which is defined in the phase k , is averaged over the total REV (eq. II.2), the expression "interphase average" is used,

$$\langle h \rangle_k = \langle h_k \rangle = \frac{1}{V} \int_{V_k} h d\Omega . \quad (\text{II.2})$$

It is often more convenient is to use the average of variable h over the phase k control volume V_k (II.3). In this case the expression "intrapphase average" is used.

$$\bar{h}_k = \frac{1}{V_k} \int_{V_k} h d\Omega, \quad (\text{II.3})$$

where $\bar{h}_k = h - h_k'$. Thus h_k' is defined as a discrepancy from the intraphase average \bar{h}_k in the volume V_k , which is occupied by the phase k . From the definitions (II.2) and (II.3), the relationship between interphase and intraphase average is

$$\langle h \rangle_k = \alpha_k \bar{h}_k. \quad (\text{II.4})$$

When the phase-interface is fixed in space, the volume averaging is a linear operator:

$$\begin{aligned} \langle h + g \rangle_k &= \langle h \rangle_k + \langle g \rangle_k, \\ \langle \beta h \rangle_k &= \beta \langle h \rangle_k \end{aligned} \quad (\text{II.5})$$

and

$$\begin{aligned} \overline{(h + g)}_k &= \bar{h}_k + \bar{g}_k, \\ \overline{(\beta h)}_k &= \beta \bar{h}_k. \end{aligned} \quad (\text{II.6})$$

where h and g are two independent functions and β is a constant.

II.2 Time and Space Derivatives

If the composition of the multiphase media is steady, the average of the time derivative can be treated as

$$\left\langle \frac{\partial h}{\partial t} \right\rangle_k = \frac{\partial}{\partial t} \langle h \rangle_k \quad (\text{II.7})$$

and

$$\overline{\left(\frac{\partial h}{\partial t} \right)_k} = \frac{\partial}{\partial t} \bar{h}_k. \quad (\text{II.8})$$

Applying volume averaging to a spatial derivative produces two terms:

$$\left\langle \frac{\partial h}{\partial x_j} \right\rangle_k = \frac{\partial}{\partial x_j} \langle h \rangle_k + \frac{1}{V} \int_{A_o} h d\Lambda_j \quad (\text{II.9})$$

and

$$\overline{\left(\frac{\partial h}{\partial x_j} \right)_k} = \frac{\partial}{\partial x_j} \bar{h}_k + \frac{1}{V_k} \int_{A_o} h' d\Lambda_j, \quad (\text{II.10})$$

where the last term in both cases is an interface exchange term.

II.3 Convection Terms

Convection terms for porous media flow transport equations can be now constructed using the VAT basic rules (II.1-II.10). The interphase average of a nonlinear convection term, composed of functions h and g , is expanded as

$$\begin{aligned}
 \left\langle \frac{\partial hg}{\partial x_j} \right\rangle_k &= \frac{\partial}{\partial x_j} \langle hg \rangle_k + \frac{1}{V} \int_{A_o} hg d\Lambda_j & (II.11) \\
 &= \frac{\partial}{\partial x_j} \alpha_k \overline{(hg)}_k + \frac{1}{V} \int_{A_o} hg d\Lambda_j \\
 &= \frac{\partial}{\partial x_j} (\alpha_k \bar{h}_k \bar{g}_k + \alpha_k \overline{h'_k g'_k}) + \frac{1}{V} \int_{A_o} hg d\Lambda_j \\
 &= \alpha_k \bar{h}_k \frac{\partial \bar{g}_k}{\partial x_j} + \alpha_k \bar{g}_k \frac{\partial \bar{h}_k}{\partial x_j} + \frac{\partial}{\partial x_j} \langle h'_k g'_k \rangle_k + \frac{1}{V} \int_{A_o} hg d\Lambda_j \\
 &= \alpha_k \bar{h}_k \frac{\partial \bar{g}_k}{\partial x_j} + \alpha_k \bar{g}_k \left(\frac{\partial h}{\partial x_j} \right)_k - \frac{\alpha_k \bar{g}_k}{V_k} \int_{A_o} h' d\Lambda_j + \frac{\partial}{\partial x_j} \langle h'_k g'_k \rangle_k + \frac{1}{V} \int_{A_o} hg d\Lambda_j .
 \end{aligned}$$

II.4 Diffusion Terms

The derivation of the interphase average of a diffusion term at constant diffusivity λ_k is presented using only VAT basic rules (II.1-II.10):

$$\begin{aligned}
 \left\langle \lambda \frac{\partial h}{\partial x_j} \right\rangle_k &= \lambda_k \frac{\partial}{\partial x_j} \langle h \rangle_k + \frac{\lambda_k}{V} \int_{A_o} h d\Lambda_j & (II.12) \\
 &= \lambda_k \frac{\partial}{\partial x_j} (\alpha_k \bar{h}_k) + \frac{\lambda_k}{V} \int_{A_o} (\bar{h} + h') d\Lambda_j \\
 &= \lambda_k \alpha_k \frac{\partial \bar{h}_k}{\partial x_j} + \lambda_k \bar{h}_k \frac{\partial \alpha_k}{\partial x_j} + \frac{\lambda_k}{V} \int_{A_o} \bar{h} d\Lambda_j + \frac{\lambda_k}{V} \int_{A_o} h' d\Lambda_j \\
 &= \lambda_k \alpha_k \frac{\partial \bar{h}_k}{\partial x_j} + \lambda_k \bar{h}_k \frac{\partial \alpha_k}{\partial x_j} + \frac{\lambda_k}{V} \bar{h}_k \int_{A_o} d\Lambda_j + \frac{\lambda_k}{V} \int_{A_o} h' d\Lambda_j \\
 &= \lambda_k \alpha_k \frac{\partial \bar{h}_k}{\partial x_j} + \lambda_k \bar{h}_k \frac{\partial \alpha_k}{\partial x_j} + \lambda_k \bar{h}_k \left(- \frac{\partial \alpha_k}{\partial x_j} \right) + \frac{\lambda_k}{V} \int_{A_o} h' d\Lambda_j \\
 &= \lambda_k \alpha_k \frac{\partial}{\partial x_j} \bar{h}_k + \frac{\lambda_k}{V} \int_{A_o} h' d\Lambda_j
 \end{aligned}$$

Furthermore, the interphase average of a diffusion term spatial derivative is introduced to simplify the derivation of the porous media flow transport equations:

$$\begin{aligned}
\left\langle \frac{\partial}{\partial x_j} \left(\lambda \frac{\partial h}{\partial x_j} \right) \right\rangle_k &= \lambda_k \frac{\partial}{\partial x_j} \left\langle \frac{\partial h}{\partial x_j} \right\rangle_k + \frac{\lambda_k}{V} \int_{A_o} \frac{\partial h}{\partial x_j} d\Lambda_j & (\text{II.13}) \\
&= \lambda_k \frac{\partial}{\partial x_j} \left(\frac{\partial}{\partial x_j} \langle h \rangle_k + \frac{1}{V} \int_{A_o} h d\Lambda_j \right) + \frac{\lambda_k}{V} \int_{A_o} \frac{\partial h}{\partial x_j} d\Lambda_j \\
&= \lambda_k \frac{\partial}{\partial x_j} \left(\frac{\partial}{\partial x_j} \alpha_k \bar{h}_k + \frac{1}{V} \int_{A_o} (\bar{h} + h') d\Lambda_j \right) + \frac{\lambda_k}{V} \int_{A_o} \frac{\partial h}{\partial x_j} d\Lambda_j \\
&= \lambda_k \frac{\partial}{\partial x_j} \left(\bar{h}_k \frac{\partial \alpha_k}{\partial x_j} + \alpha_k \frac{\partial \bar{h}_k}{\partial x_j} + \frac{1}{V} \int_{A_o} \bar{h} d\Lambda_j + \frac{1}{V} \int_{A_o} h' d\Lambda_j \right) + \frac{\lambda_k}{V} \int_{A_o} \frac{\partial h}{\partial x_j} d\Lambda_j \\
&= \lambda_k \frac{\partial}{\partial x_j} \left(\bar{h}_k \frac{\partial \alpha_k}{\partial x_j} + \alpha_k \frac{\partial \bar{h}_k}{\partial x_j} + \bar{h}_k \left(-\frac{\partial \alpha_k}{\partial x_j} \right) + \frac{1}{V} \int_{A_o} h' d\Lambda_j \right) + \frac{\lambda_k}{V} \int_{A_o} \frac{\partial h}{\partial x_j} d\Lambda_j \\
&= \lambda_k \frac{\partial}{\partial x_j} \left(\alpha_k \frac{\partial \bar{h}_k}{\partial x_j} + \frac{1}{V} \int_{A_o} h' d\Lambda_j \right) + \frac{\lambda_k}{V} \int_{A_o} \frac{\partial h}{\partial x_j} d\Lambda_j
\end{aligned}$$

III. Derivation of Separate Phase Porous Media Flow Equations

This chapter presents a derivation of the mass, momentum and energy transport equations for porous media flow using the VAT basic rules (II.1-II.10) and those developed for the convection (II.11) and diffusion terms (II.13).

III.1 Mass Transport Equation

Mass as well as other transport equations are developed for laminar steady-state flow. The index f , when marking intraphase average velocity, is omitted to avoid double indexing. Starting from the mass transport equation for incompressible flow

$$\frac{\partial v_i}{\partial x_i} = 0, \quad (\text{III.1})$$

the mass transport equation is averaged over the Representative Elementary Volume (REV):

$$\left\langle \frac{\partial v_i}{\partial x_i} \right\rangle_f = 0. \quad (\text{III.2})$$

When the spatial differential rule (II.9) together with (II.4) are applied, the mass transport equation can be written as:

$$\frac{\partial}{\partial x_i} \langle v_i \rangle_f + \frac{1}{V} \int_{A_o} v_i d\Lambda_i = 0 , \quad (\text{III.3})$$

$$\frac{\partial}{\partial x_i} (\alpha_f \bar{v}_i) + \frac{1}{V} \int_{A_o} v_i d\Lambda_i = 0 .$$

As v_i is 0 on the fluid-solid interface and α_f is constant, the expression (III.3) is further simplified to:

$$\alpha_f \frac{\partial \bar{v}_i}{\partial x_i} = 0 . \quad (\text{III.4})$$

III.2 Momentum Transport Equation

Derivation of the momentum transport equation for porous media flow starts from the momentum equation for steady-state incompressible flow, where the effect of gravity is neglected:

$$\rho \frac{\partial}{\partial x_j} (v_j v_i) = - \frac{\partial p}{\partial x_i} + \frac{\partial}{\partial x_j} \left(\mu \frac{\partial v_i}{\partial x_j} \right) . \quad (\text{III.5})$$

After interphase averaging

$$\left\langle \rho \frac{\partial}{\partial x_j} (v_j v_i) \right\rangle_f = - \left\langle \frac{\partial p}{\partial x_i} \right\rangle_f + \left\langle \frac{\partial}{\partial x_j} \left(\mu \frac{\partial v_i}{\partial x_j} \right) \right\rangle_f, \quad (\text{III.6})$$

the derivations for the spatial differential (II.9), the convection (II.11) and the diffusion (II.13) terms are introduced to yield:

$$\begin{aligned} & \alpha_f \rho_f \bar{v}_j \frac{\partial \bar{v}_i}{\partial x_j} + \alpha_f \rho_f \bar{v}_i \left(\frac{\partial v_j}{\partial x_j} \right) - \frac{\alpha_f \rho_f \bar{v}_i}{V_f} \int_{A_o} v_j' d\Lambda_j + \rho_f \frac{\partial}{\partial x_j} \langle v_j' v_i' \rangle_f + \frac{\rho_f}{V} \int_{A_o} v_j v_i d\Lambda_j = \\ & = - \frac{\partial}{\partial x_i} (\alpha_f \bar{p}_f) - \frac{1}{V} \int_{A_o} p d\Lambda_i + \mu_f \frac{\partial}{\partial x_j} \left(\alpha_f \frac{\partial \bar{v}_i}{\partial x_j} + \frac{1}{V} \int_{A_o} v_i' d\Lambda_j \right) + \frac{\mu_f}{V} \int_{A_o} \frac{\partial v_i}{\partial x_j} d\Lambda_j \end{aligned} \quad (\text{III.7})$$

Next, the continuity equation (III.4) and the rigid wall assumption (v_i is 0 on the fluid-solid interface) are used to significantly simplify the equation (III.7):

$$\begin{aligned} & \alpha_f \rho_f \bar{v}_j \frac{\partial \bar{v}_i}{\partial x_j} + \rho_f \frac{\partial}{\partial x_j} \langle v_j' v_i' \rangle_f = \\ & = - \frac{\partial}{\partial x_i} (\alpha_f \bar{p}_f) - \frac{1}{V} \int_{A_o} p d\Lambda_i + \mu_f \frac{\partial}{\partial x_j} \left(\alpha_f \frac{\partial \bar{v}_i}{\partial x_j} \right) + \frac{\mu_f}{V} \int_{A_o} \frac{\partial v_i}{\partial x_j} d\Lambda_j \end{aligned} \quad (\text{III.8})$$

As the considered solid structure is uniform in space, the phase fraction α_f is constant allowing one to write:

$$\alpha_f \rho_f \bar{v}_j \frac{\partial \bar{v}_i}{\partial x_j} = -\alpha_f \frac{\partial \bar{p}_f}{\partial x_i} + \alpha_f \mu_f \frac{\partial^2 \bar{v}_i}{\partial x_j^2} - \frac{1}{V} \int_{A_o} p d\Lambda_i + \frac{\mu_f}{V} \int_{A_o} \frac{\partial v_i}{\partial x_j} d\Lambda_j \quad . \quad (\text{III.9})$$

The integrals in (III.9) are a consequence of the volumetric averaging. They capture momentum transport at the fluid-solid interface. Similar to turbulent flow, a separate model in the form of a closure relation is needed. In the present case, the integrals are replaced with the following empirical drag relation,

$$\frac{1}{2} C_d \rho_f \bar{v}_i^2 A_o = - \int_{A_o} p d\Lambda_i + \mu_f \int_{A_o} \frac{\partial v_i}{\partial x_j} d\Lambda_j \quad , \quad (\text{III.10})$$

where C_d is a drag coefficient and it depends on a local Reynolds number. Inserting the empirical correlation (III.10) into (III.9), the momentum equation for porous media flow is given by

$$\alpha_f \rho_f \bar{v}_j \frac{\partial \bar{v}_i}{\partial x_j} = -\alpha_f \frac{\partial \bar{p}_f}{\partial x_i} + \alpha_f \mu_f \frac{\partial^2 \bar{v}_i}{\partial x_j^2} + \frac{1}{2} C_d \rho_f \bar{v}_i^2 S \quad , \quad (\text{III.11})$$

where S is the specific surface of the structure.

III.3 Energy Transport Equation for Fluid

The energy transport equation for porous media flow is developed from the energy transport equation for steady-state incompressible flow:

$$\rho c \frac{\partial}{\partial x_j} (v_j T) = \frac{\partial}{\partial x_j} \left(\lambda \frac{\partial T}{\partial x_j} \right). \quad (\text{III.12})$$

When the interphase averaging is applied,

$$\left\langle \rho c \frac{\partial}{\partial x_j} (v_j T) \right\rangle_f = \left\langle \frac{\partial}{\partial x_j} \left(\lambda \frac{\partial T}{\partial x_j} \right) \right\rangle_f, \quad (\text{III.13})$$

the convection (II.11) and diffusion (II.13) terms are introduced to obtain

$$\begin{aligned} & \alpha_f \rho_f c_f \bar{v}_j \frac{\partial \bar{T}_f}{\partial x_j} + \alpha_f \rho_f c_f \bar{T}_f \left(\frac{\partial v_j}{\partial x_j} \right) - \frac{\alpha_f \rho_f c_f \bar{T}_f}{V_f} \int_{A_o} v_j' d\Lambda_j + \rho_f c_f \frac{\partial}{\partial x_j} \langle v_j' T' \rangle_f \\ & + \frac{\rho_f c_f}{V} \int_{A_o} v_j T d\Lambda_j = \lambda_f \frac{\partial}{\partial x_j} \left(\alpha_f \frac{\partial \bar{T}_f}{\partial x_j} + \frac{1}{V} \int_{A_o} T' d\Lambda_j \right) + \frac{\lambda_f}{V} \int_{A_o} \frac{\partial T}{\partial x_j} d\Lambda_j \end{aligned} \quad (\text{III.14})$$

Like the momentum equation development, the continuity equation (III.4) and the rigid wall assumption simplify the equation (III.14) to

$$\alpha_f \rho_f c_f \bar{v}_j \frac{\partial \bar{T}_f}{\partial x_j} + \rho_f c_f \frac{\partial}{\partial x_j} \langle v_j' T' \rangle_f = \lambda_f \frac{\partial}{\partial x_j} \left(\alpha_f \frac{\partial \bar{T}_f}{\partial x_j} + \frac{1}{V} \int_{A_o} T' d\Lambda_j \right) + \frac{\lambda_f}{V} \int_{A_o} \frac{\partial T}{\partial x_j} d\Lambda_j \quad (\text{III.15})$$

Spatial uniformity reduces (III.15) to

$$\alpha_f \rho_f c_f \bar{v}_j \frac{\partial \bar{T}_f}{\partial x_j} = \alpha_f \lambda_f \frac{\partial^2 \bar{T}_f}{\partial x_j^2} + \frac{\lambda_f}{V} \int_{A_o} \frac{\partial T}{\partial x_j} d\Lambda_j . \quad (\text{III.16})$$

The integral term in (III.16) represents the interfacial heat exchange between fluid flow and the solid structure and, requires additional modeling. In the present case an empirical linear relation between the fluid and the solid temperature is taken as an appropriate model for the interphase heat flow:

$$h(\bar{T}_f - \bar{T}_s) A_o = -\lambda_f \int_{A_o} \frac{\partial T}{\partial x_j} d\Lambda_j \quad , \quad (\text{III.17})$$

where h is a heat transfer coefficient that depends on the local Reynolds number. By substituting the relation given by (III.17) into (III.16), the porous media flow energy transport equation can be written as:

$$\alpha_f \rho_f c_f \bar{v}_j \frac{\partial \bar{T}_f}{\partial x_j} = \alpha_f \lambda_f \frac{\partial^2 \bar{T}_f}{\partial x_j^2} - h(\bar{T}_f - \bar{T}_s) S \quad . \quad (\text{III.18})$$

III.4 Energy Transport Equation for Solid

In the solid phase, thermal diffusion is the only heat transport mechanism. Therefore, the energy transport equation is reduced to the simple diffusion equation:

$$0 = \frac{\partial}{\partial x_j} \left(\lambda \frac{\partial T}{\partial x_j} \right). \quad (\text{III.19})$$

After performing the interphase averaging:

$$0 = \left\langle \frac{\partial}{\partial x_j} \left(\lambda \frac{\partial T}{\partial x_j} \right) \right\rangle_s \quad (\text{III.20})$$

and substituting the diffusion term derivative given by (II.13),

$$0 = \lambda_s \frac{\partial}{\partial x_j} \left(\alpha_s \frac{\partial \bar{T}_s}{\partial x_j} + \frac{1}{V} \int_{A_b} T' d\Lambda_j \right) + \frac{\lambda_s}{V} \int_{A_b} \frac{\partial T}{\partial x_j} d\Lambda_j \quad (\text{III.21})$$

The spatial uniformity reduces the equation (III.21) to

$$0 = \alpha_s \lambda_s \frac{\partial^2 \bar{T}_s}{\partial x_j^2} + \frac{\lambda_s}{V} \int_{A_b} \frac{\partial T}{\partial x_j} d\Lambda_j, \quad (\text{III.22})$$

where the integral captures the interphase heat exchange. Closure is obtained by substituting the linear relation:

$$h(\bar{T}_f - \bar{T}_s)A_o = \lambda_s \int_{A_o} \frac{\partial T}{\partial x_j} d\Lambda_j \quad (\text{III.23})$$

into (III.22). The VAT energy transport equation in solid structure is written as

$$0 = \alpha_s \lambda_s \frac{\partial^2 \bar{T}_s}{\partial x_j^2} + h(\bar{T}_f - \bar{T}_s)S. \quad (\text{III.24})$$

IV. Experimental Test Section

In order to understand the model boundary conditions and further simplification of the porous media flow model (III.4, III.11, III.18 and III.24), the experimental test section has to be described in more details.

The geometry of the simulation domain follows the geometry of the experimental test section used in the Morrin-Martinelli-Gier Memorial Heat Transfer Laboratory at University of California, Los Angeles, where experimental data described in Rizzi et al. (2001) were taken.

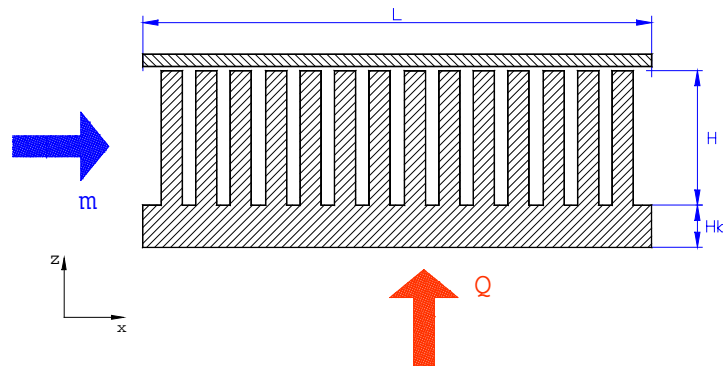


Figure IV-1: Experimental test section.

The general arrangement of the heat sink pin-fins is given in Fig. IV-1. The length L as well as the width W of the heat sink is 0.1145m (4.5"), whereas the height H is 0.0381m (1.5"). The conductive base plate, which connects pin-fins, is 0.00635m (0.25") high.

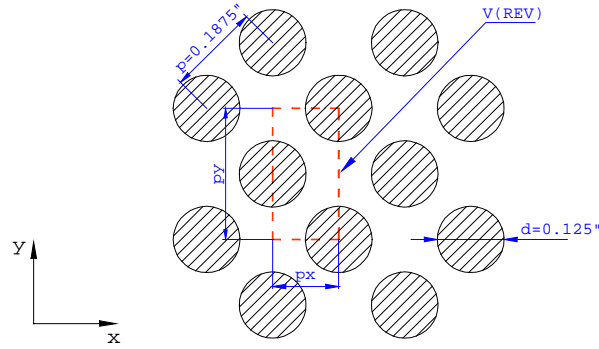


Figure IV-2: Pin-fins arrangement.

The simulation domain consists of 31 rows of pin-fins in the streamwise direction and 31 rows of pin-fins in the transverse direction. The diameter of the pin-fins is $d = 0.003175\text{m}$ (0.125"). The pitch-to-diameter ratio in the streamwise direction is set to $p_x/d = 1.06$ and in the transverse direction to $p_y/d = 2.12$.

Based on the geometrical measures, the fluid-phase fraction or the porosity of the test section is calculated to be

$$\alpha_f = \frac{V_f}{V} = 0.3491, \quad (\text{IV.1})$$

and the hydraulic diameter of the test section is

$$d_h = 4 \frac{V_f}{A_c} = 0.005522 \text{ m} , \quad (\text{IV.2})$$

where A_c is the contact flow area of the test section.

The specific surface of REV is found to be

$$S = \frac{A_o}{V} = 439.77 \text{ m}^{-1}. \quad (\text{IV.3})$$

The material properties are taken from the experimental cases. The heat sink consists of cast aluminum alloy 195 (cast) and it is exposed to air cross-flow. The entering flow profile is uniform due to two rows of honeycomb flow-straighteners that are placed in front of the test section. A thermal isolation layer placed between the heater and the aluminum base sets the isothermal conditions of the base bottom.

The experimental data were taken at 3 different heating rates (approximately 50W, 125W and 220W) and at 4 different whole-section pressure drops (approximately 75 Pa, 175 Pa, 275 Pa and 360 Pa). The exact values are summarized in Table IV-1.

Table IV-1: Pressure and heating power for experimental cases.

Power [W]	Pressure drop [Pa]
48.96	74.72
48.96	175.6
50.37	266.5
50.53	368.6
125.2	74.72
124.4	179.3
125.2	274.0
125.2	361.1
224.3	74.72
221.6	180.6
232.7	280.2
232.7	361.1

V. Governing Equations for Uniform Flow within a Heat Sink

The mathematical model of the flow through the heat sink is based on a description of the separate phase porous media flow given in chapter II. It consists of a mass transport equation, a momentum transport equation, an energy transport equation for the fluid flow, an energy transport equation for the solid structure and an energy transport equations for the heat conductive base-plate, which are developed from (III.4, III.11, III.18 and III.24). As all of the equation variables are already averaged over the appropriate V_k , the averaging symbol $\bar{}$ is omitted. Furthermore, to distinguish dimensional from non-dimensional forms of the equations, the caret symbol $\hat{}$ is used to mark dimensional variables.

V.1 Momentum Transport in Fluid Flow

The momentum transport equation for the fluid flow is developed from (III.11) with the additional assumption that the volume average velocity through the heat sink is unidirectional: $v=\{u,0,0\}$. As a consequence, the velocity changes only transverse to the flow direction. This means that the pressure force across the entire simulation domain is balanced with shear forces. As a result, the momentum transport equation is reduced to

$$-\alpha_f \hat{\mu}_f \left(\frac{\partial^2 \hat{u}}{\partial \hat{y}^2} + \frac{\partial^2 \hat{u}}{\partial \hat{z}^2} \right) + \frac{1}{2} C_d \hat{\rho}_f \hat{u}^2 \hat{S} = \frac{\Delta \hat{p}}{\hat{L}} \quad , \quad (\text{V.1})$$

where S is the specific surface (IV.3) and L is the length of the entire simulation domain.

The boundary conditions for the model equations attempt to represent the experimental conditions described in chapter IV. For the momentum transport equation (V.1), no-slip boundary conditions are implemented at all four walls parallel to the flow direction:

$$\begin{aligned} \hat{u}(0, \hat{z}) = 0, \quad \hat{u}(\hat{W}, \hat{z}) = 0, \\ \hat{u}(\hat{y}, 0) = 0, \quad \hat{u}(\hat{y}, \hat{H}) = 0. \end{aligned} \quad (\text{V.2})$$

The preset values of pressure drop Δp are summarized in Table V-1.

Table V-1: Whole-section pressure drop Δp [Pa] at 50W, 125W and 220W.

Δp [Pa] at 50W	5.0	10.0	20.0	40.0	74.72	175.6	266.5	368.6
Δp [Pa] at 125W	5.0	10.0	20.0	40.0	74.72	179.3	274.0	361.1
Δp [Pa] at 220W	5.0	10.0	20.0	40.0	74.72	180.6	280.2	361.1

V.2 Energy Transport in Fluid Flow

The energy transport equation for the fluid flow is developed from (III.18) with the unidirectional velocity assumption. The temperature field in the fluid results from a balance between thermal convection in the streamwise direction, thermal diffusion and the heat transferred from the solid structure to the fluid flow.

Thus, the differential form of the energy equation for the fluid is:

$$\alpha_f \hat{\rho}_f \hat{c}_f \hat{u} \frac{\partial \hat{T}_f}{\partial \hat{x}} = \alpha_f \hat{\lambda}_f \left(\frac{\partial^2 \hat{T}_f}{\partial \hat{x}^2} + \frac{\partial^2 \hat{T}_f}{\partial \hat{y}^2} + \frac{\partial^2 \hat{T}_f}{\partial \hat{z}^2} \right) - \hat{h}(\hat{T}_f - \hat{T}_s) \hat{S} \quad (\text{V.3})$$

For the fluid-phase energy transport equation (V.3), the simulation domain inflow and the bottom wall are taken as isothermal:

$$\hat{T}_f(0, \hat{y}, \hat{z}) = \hat{T}_m, \quad \hat{T}_f(\hat{x}, \hat{y}, 0) = \hat{T}_{if}(\hat{x}, \hat{y}, 0) \quad (\text{V.4})$$

whereas the other boundary conditions are adiabatic:

$$\begin{aligned} \frac{\partial \hat{T}_f}{\partial \hat{x}}(\hat{L}, \hat{y}, \hat{z}) &= 0, \\ \frac{\partial \hat{T}_f}{\partial \hat{y}}(\hat{x}, 0, \hat{z}) &= 0, \quad \frac{\partial \hat{T}_f}{\partial \hat{y}}(\hat{x}, \hat{W}, \hat{z}) = 0, \\ \frac{\partial \hat{T}_f}{\partial \hat{z}}(\hat{x}, \hat{y}, \hat{H}) &= 0. \end{aligned} \quad (\text{V.5})$$

The inflow boundary values T_{in} for the fluid temperature T_f are summarized in Table V-2.

Table V-2: Inflow temperature T_{in} [°C] at 50W, 125W and 220W.

T_{in} [°C] at 50W	23.0	23.0	23.0	23.00	23.02	23.02	23.04	22.85
T_{in} [°C] at 125W	23.0	23.0	23.0	23.0	23.16	23.21	23.05	22.81
T_{in} [°C] at 220W	23.0	23.0	23.0	23.0	23.07	22.96	22.97	22.90

It should be noted that the interface temperature T_{if} is influenced by the heat distribution in the conductive base-plate and is therefore position dependent.

V.3 Energy Transport in the Solid Structure

The energy transport equation in the solid structure is developed from (III.24). The heat sink structure in each REV is only loosely connected in horizontal directions (see Fig. IV-2). As a consequence, only the thermal diffusion in the vertical direction is in balance with the heat leaving the structure through the fluid-solid interface, whereas the thermal diffusion in the horizontal directions can be neglected. This simplifies the energy equation for the solid structure to:

$$0 = \alpha_s \hat{\lambda}_s \frac{\partial^2 \hat{T}_s}{\partial z^2} + \hat{h} (\hat{T}_f - \hat{T}_s) \hat{S} \quad (\text{V.6})$$

where α_s is the solid fraction and is equal to $1 - \alpha_f$.

For the solid-phase energy transport equation (V.6), the bottom wall is prescribed as isothermal, whereas the top wall was assumed to be adiabatic:

$$\hat{T}_s(\hat{x}, \hat{y}, 0) = \hat{T}_{if}(\hat{x}, \hat{y}, 0), \quad \frac{\partial \hat{T}_s}{\partial \hat{z}}(\hat{x}, \hat{y}, \hat{H}) = 0 . \quad (\text{V.7})$$

V.4 Energy Transport in the Solid Base

The energy transport equation in the solid base-plate is developed from (III.24). As there is no heat transfer between solid and fluid phase except on the upper boundary, the interphase heat exchange term is omitted. Therefore, the energy transport equation reduces to the thermal diffusion equation in all three dimensions:

$$0 = \hat{\lambda}_s \left(\frac{\partial^2 \hat{T}_b}{\partial \hat{x}^2} + \frac{\partial^2 \hat{T}_b}{\partial \hat{y}^2} + \frac{\partial^2 \hat{T}_b}{\partial \hat{z}^2} \right). \quad (\text{V.8})$$

The boundary conditions for the solid base-plate show the coupled nature of heat transfer between the homogenous porous media flow (V.3 and V.6) and the base (V.8). Namely, the heat flux at the interface between the porous media and the base must be equal:

$$\lambda_s \frac{\partial \hat{T}_b}{\partial \hat{z}}(\hat{x}, \hat{y}, 0) = \alpha_f \lambda_f \frac{\partial \hat{T}_f}{\partial \hat{z}}(\hat{x}, \hat{y}, 0) + \alpha_s \lambda_s \frac{\partial \hat{T}_s}{\partial \hat{z}}(\hat{x}, \hat{y}, 0) . \quad (\text{V.9})$$

The calculated solid base temperature T_b on the boundary is equal to the interface temperature T_{if} , which is used as a boundary condition (V.4 and V.7) in the energy transport equations (V.3 and V.6). At the bottom of the base-plate, isothermal boundary conditions are prescribed

$$\hat{T}_b(\hat{x}, \hat{y}, -\hat{H}_b) = \hat{T}_g \quad , \quad (\text{V.10})$$

whereas the horizontal walls are taken to be adiabatic

$$\frac{\partial \hat{T}_b}{\partial \hat{x}}(0, \hat{y}, \hat{z}) = 0, \quad \frac{\partial \hat{T}_b}{\partial \hat{x}}(\hat{L}, \hat{y}, \hat{z}) = 0 \quad , \quad (\text{V.11})$$

$$\frac{\partial \hat{T}_b}{\partial \hat{y}}(\hat{x}, 0, \hat{z}) = 0, \quad \frac{\partial \hat{T}_b}{\partial \hat{y}}(\hat{x}, \hat{W}, \hat{z}) = 0 \quad .$$

The bottom boundary values T_g for the solid base temperature T_b are summarized in Table V-3.

Table V-3: Solid base bottom temperature T_g [°C] at 50W, 125W and 220W.

T_g [°C] at 50W	54.9	43.43	37.2	33.0	30.3	27.9	27.3	26.64
T_g [°C] at 125W	103.8	74.6	58.8	48.15	41.8	35.73	33.6	32.25
T_g [°C] at 220W	168.0	114.8	87.0	68.0	56.4	45.2	42.3	40.4

VI. Scaling Procedure for Governing Equations

The transport equations (V.1, V.3, V.6, V.8) and their boundary conditions (V.2, V.4, V.5, V.7, V.9, V.10, V.11) need to be transformed into dimensionless form. The dimensionless form eases identification of different mechanisms as well as comparison of results with other authors. Moreover, the dimensionless form of equations also enables one to use more general numerical algorithms that are already developed and are publicly accessible.

VI.1 Scaling Factors

The scaling laws that are used for transformation of the equations to dimensionless form are summarized in (VI.1-VI.3). Equation (VI.1) presents scaling factors for the spatial coordinates x , y and z .

$$\hat{x} = \hat{L} x, \quad \hat{y} = \hat{W} y, \quad \hat{z} = \hat{H} z \quad \text{and} \quad \hat{z} = \hat{H}_b z. \quad (\text{VI.1})$$

Scaling factors for the kinematic variables are presented in (VI.2).

$$\hat{u} = \hat{U} u, \quad \hat{p} = \hat{\rho}_f \hat{U}^2 p, \quad \Delta \hat{p} = \hat{\rho}_f \hat{U}^2, \quad Re_s = \frac{\hat{U} \hat{d}_h}{\nu_f}. \quad (\text{VI.2})$$

Newly defined is the pore Reynolds number Re_s , which is based on the velocity scale U

and hydraulic diameter d_h (IV.2). The scaling relations for the fluid, solid and base plate temperatures are given in (VI.3):

$$\hat{T}_g - \hat{T}_f = (\hat{T}_g - \hat{T}_{in}) T_f, \quad \hat{T}_g - \hat{T}_s = (\hat{T}_g - \hat{T}_{in}) T_s, \quad \hat{T}_g - \hat{T}_b = (\hat{T}_g - \hat{T}_{in}) T_b \quad . \quad (\text{VI.3})$$

VI.2 Momentum Transport in Fluid Flow

Applying the scaling laws (VI.1, VI.2) to the momentum transport equation (V.1), yields

$$-\alpha_f \hat{\rho}_f \hat{\nu}_f \left(\frac{\hat{U}}{\hat{W}^2} \frac{\partial^2 u}{\partial y^2} + \frac{\hat{U}}{\hat{H}^2} \frac{\partial^2 u}{\partial z^2} \right) + \frac{1}{2} C_d \hat{\rho}_f \hat{U}^2 u^2 \hat{S} = \frac{\hat{\rho}_f \hat{U}^2}{\hat{L}} \quad (\text{VI.4})$$

The scaling factors are then grouped into dimensionless parameters:

$$-\frac{\alpha_f}{Re_s} \left(\frac{\hat{d}_h^2}{\hat{W}^2} \right) \frac{\partial^2 u}{\partial y^2} - \frac{\alpha_f}{Re_s} \left(\frac{\hat{d}_h^2}{\hat{H}^2} \right) \frac{\partial^2 u}{\partial z^2} + \frac{1}{2} C_d (\hat{d}_h \hat{S}) u^2 = \frac{\hat{d}_h}{\hat{L}} \quad (\text{VI.5})$$

Finally, the momentum transport equation can be written as

$$-M_1 \frac{\partial^2 u}{\partial y^2} - M_2 \frac{\partial^2 u}{\partial z^2} + M_3 u^2 = M_4 \quad , \quad (\text{VI.6})$$

where M_1 , M_2 , M_3 and M_4 are constants, defined as follows:

$$M_1 = \alpha_f / Re_s (\hat{d}_h^2 / \hat{W}^2), \quad M_2 = \alpha_f / Re_s (\hat{d}_h^2 / \hat{H}^2), \quad (VI.7)$$

$$M_3 = 1/2 C_d (\hat{d}_h \hat{S}), \quad M_4 = \hat{d}_h / \hat{L}.$$

Based on the scaling laws (VI.1-VI.3), the boundary conditions (V.2) change to

$$u(0, z) = 0, \quad u(1, z) = 0, \quad (VI.8)$$

$$u(y, 0) = 0, \quad u(y, 1) = 0.$$

VI.3 Energy Transport in Fluid Flow

When the scaling laws (VI.1-VI.3) are introduced into the fluid-phase energy transport equation (V.3), the equation is changed to:

$$\alpha_f \hat{\rho}_f \hat{c}_f \frac{\hat{U}}{\hat{L}} u \frac{\partial T_f}{\partial x} = \alpha_f \hat{\lambda}_f \left(\frac{1}{\hat{L}^2} \frac{\partial^2 T_f}{\partial x^2} + \frac{1}{\hat{W}^2} \frac{\partial^2 T_f}{\partial y^2} + \frac{1}{\hat{H}^2} \frac{\partial^2 T_f}{\partial z^2} \right) - \hat{h} (T_f - T_s) \hat{S}. \quad (VI.9)$$

When the dimensionless parameters are formed:

$$\begin{aligned} \alpha_f Pr Re_s \left(\frac{\hat{d}_h}{\hat{L}} \right) u \frac{\partial T_f}{\partial x} &= \tag{VI.10} \\ &= \alpha_f \left(\frac{\hat{d}_h^2}{\hat{L}^2} \right) \frac{\partial^2 T_f}{\partial x^2} + \alpha_f \left(\frac{\hat{d}_h^2}{\hat{W}^2} \right) \frac{\partial^2 T_f}{\partial y^2} + \alpha_f \left(\frac{\hat{d}_h^2}{\hat{H}^2} \right) \frac{\partial^2 T_f}{\partial z^2} - Nu_s (\hat{d}_h \hat{S}) (T_f - T_s) \end{aligned}$$

where Nu_s is the Nusselt number based on the hydraulic diameter. Equation (VI.10) can be further simplified to

$$F_1 u \frac{\partial T_f}{\partial x} = F_2 \frac{\partial^2 T_f}{\partial x^2} + F_3 \frac{\partial^2 T_f}{\partial y^2} + F_4 \frac{\partial^2 T_f}{\partial z^2} - F_5 (T_f - T_s), \tag{VI.11}$$

where F_1, F_2, F_3, F_4 and F_5 are constants. These constants are defined as

$$\begin{aligned} F_1 &= \alpha_f Pr Re_s (\hat{d}_h / \hat{L}), & F_2 &= \alpha_f (\hat{d}_h^2 / \hat{L}^2), & \tag{VI.12} \\ F_3 &= \alpha_f (\hat{d}_h^2 / \hat{W}^2), & F_4 &= \alpha_f (\hat{d}_h^2 / \hat{H}^2), & F_5 &= Nu_s (\hat{d}_h \hat{S}). \end{aligned}$$

Based on the scaling laws (VI.1-VI.3) the boundary conditions (V.4, V.5) change to

$$\begin{aligned}
 T_f(0, y, z) &= 1, & \frac{\partial T_f}{\partial x}(1, y, z) &= 0, \\
 \frac{\partial T_f}{\partial y}(x, 0, z) &= 0, & \frac{\partial T_f}{\partial y}(x, 1, z) &= 0, \\
 T_f(x, y, 0) &= T_{if}(x, y, 0), & \frac{\partial T_f}{\partial z}(x, y, 1) &= 0.
 \end{aligned} \tag{VI.13}$$

VI.4 Energy Transport in the Solid Structure

As in the previous case, applying the scaling laws (VI.1, VI.3) to the solid-phase energy transport equation (V.6) gives the following form:

$$0 = \alpha_s \hat{\lambda}_s \left(\frac{1}{\hat{H}^2} \frac{\partial^2 T_s}{\partial z^2} \right) + \hat{h} (T_f - T_s) \hat{S} \quad . \tag{VI.14}$$

When the scaling factors are grouped into dimensionless parameters,

$$0 = \alpha_s \left(\frac{\hat{d}_h^2}{\hat{H}^2} \right) \frac{\partial^2 T_s}{\partial z^2} + Nu_s \left(\frac{\hat{\lambda}_f}{\hat{\lambda}_s} \right) (\hat{d}_h \hat{S}) (T_f - T_s) \quad . \tag{VI.15}$$

and the solid-phase energy transport equation (VI.15) is reduced to

$$0 = S_1 \frac{\partial^2 T_s}{\partial z^2} + S_2 (T_f - T_s) \quad , \quad (\text{VI.16})$$

where S_1 and S_2 are constants defined as

$$S_1 = \alpha_s (\hat{d}_h^2 / \hat{H}^2) \quad \text{and} \quad S_2 = Nu_s (\hat{\lambda}_f / \hat{\lambda}_s) (\hat{d}_h \hat{S}) . \quad (\text{VI.17})$$

The solid structure boundary conditions (V.7) also change to

$$T_s(x, y, 0) = T_{if}(x, y, 0), \quad \frac{\partial T_s}{\partial z}(x, y, 1) = 0 . \quad (\text{VI.18})$$

VI.5 Energy Transport in the Solid Base

After scaling, the heat conduction equation in the solid base-plate (V.8) becomes:

$$0 = \frac{1}{\hat{L}^2} \frac{\partial^2 T_b}{\partial x^2} + \frac{1}{\hat{W}^2} \frac{\partial^2 T_b}{\partial y^2} + \frac{1}{\hat{H}_b^2} \frac{\partial^2 T_b}{\partial z^2} . \quad (\text{VI.19})$$

Grouping of the scale factors into dimensionless parameters yields,

$$0 = \left(\frac{\hat{d}_h^2}{\hat{L}^2} \right) \frac{\partial^2 T_b}{\partial x^2} + \left(\frac{\hat{d}_h^2}{\hat{W}^2} \right) \frac{\partial^2 T_b}{\partial y^2} + \left(\frac{\hat{d}_h^2}{\hat{H}_b^2} \right) \frac{\partial^2 T_b}{\partial z^2} . \quad (\text{VI.20})$$

Equation (VI.20) can also be written as

$$0 = B_1 \frac{\partial^2 T_b}{\partial x^2} + B_2 \frac{\partial^2 T_b}{\partial y^2} + B_3 \frac{\partial^2 T_b}{\partial z^2} , \quad (\text{VI.21})$$

where B_1 , B_2 and B_3 are constants, defined as

$$B_1 = (\hat{d}_h^2 / \hat{L}^2), \quad B_2 = (\hat{d}_h^2 / \hat{W}^2), \quad B_3 = (\hat{d}_h^2 / \hat{H}_b^2). \quad (\text{VI.22})$$

Transformation to dimensionless form also changes the boundary conditions (V.9, V.10, V.11) to

$$\begin{aligned} \frac{\partial T_b}{\partial x}(0, y, z) = 0, \quad \frac{\partial T_b}{\partial x}(1, y, z) = 0, \\ \frac{\partial T_b}{\partial y}(x, 0, z) = 0, \quad \frac{\partial T_b}{\partial y}(x, 1, z) = 0, \\ T_b(x, y, -1) = 0, \quad \frac{\partial T_b}{\partial z}(x, y, 0) = \alpha_f \left(\frac{\lambda_f}{\lambda_s} \right) \frac{\partial T_f}{\partial z}(x, y, 0) + \alpha_s \left(\frac{H}{H_b} \right) \frac{\partial T_s}{\partial z}(x, y, 0) . \end{aligned} \quad (\text{VI.23})$$

VII. Galerkin Solution Method

The Galerkin method (GM) and the Finite Volume Method (FVM) are selected for solution of the separate phase porous media flow equations. Although FVM is a much more generally applicable method than the semi-analytical GM, the latter is used as a verification tool for numerical results.

In the past the GM was widely used for transport phenomena related problems (Catton, 1970, Catton, 1972, McDonough and Catton, 1982, Howle, 1996). Nevertheless, at present, the GM popularity decreases due to serious limitations in method applicability to more realistic geometries and boundary conditions.

This chapter explains implementation of the GM for heat transfer calculations in channel flow and in porous media flow.

VII.1 Channel Flow

Channel flow was investigated with the GM in order to compare its thermal effectiveness with the heat sink thermal effectiveness. This gives a clear picture of thermal enhancement due to the thermal conductive structure immersed into the coolant stream.

In the present case, the system of transport equations is further reduced to two dimensions. Although the reason for this spatial reduction is to simplify the GM calculation procedure, the flow variations in horizontal spanwise direction (y - direction) are indeed small enough that they can be neglected. Furthermore, as the solid-phase is not present in channel flow, $C_d = 0.0$ and therefore $M_3 = 0.0$. Thus, equation (VI.6) is reduced to

$$-M_2 \frac{\partial^2 u}{\partial z^2} = M_4 \quad (\text{VII.1})$$

and the boundary conditions are

$$u(0) = 0, \quad u(1) = 0. \quad (\text{VII.2})$$

The momentum transport equation (VII.1) is solved with integration in two stages. Thus, the fluid velocity is

$$u = \frac{M_4}{2M_2} z(1-z). \quad (\text{VII.3})$$

The energy transport equation for the fluid flow (VI.11) is reduced to

$$F_1 u \frac{\partial T_f}{\partial x} = F_4 \frac{\partial^2 T_f}{\partial z^2}, \quad (\text{VII.4})$$

where the diffusion terms in horizontal spanwise and streamwise directions are neglected. As the solid-phase is not present in the channel flow, the interphase heat transfer term is dropped. For the same reason the boundary conditions are

$$\begin{aligned} T_f(0,z) &= 1, & \frac{\partial T_f}{\partial x}(1,z) &= 0, \\ T_f(x,0) &= 0, & \frac{\partial T_f}{\partial z}(x,1) &= 0. \end{aligned} \quad (\text{VII.5})$$

The solution of the convection-diffusion equation (VII.4) can be approached with separation of variables:

$$T_f = X(x)Z(z). \quad (\text{VII.6})$$

Inserting (VII.6) into (VII.4) the following expression is obtained

$$u X' Z = \frac{F_4}{F_1} X Z'' . \quad (\text{VII.7})$$

Rearranging it to

$$\frac{X'}{X} = \frac{F_4}{F_1} \frac{Z''}{u Z} = -\beta, \quad (\text{VII.8})$$

yields differential equations for the x -direction:

$$X' + \beta X = 0 \quad , \quad (\text{VII.9})$$

and for the z -direction :

$$Z'' + \beta \frac{F_1}{F_4} u Z = 0 \quad . \quad (\text{VII.10})$$

The boundary conditions are

$$X(0) = 1, \quad \frac{\partial X}{\partial x}(1) = 0, \quad (\text{VII.11})$$

and the solution to (VII.9) is obtained with straightforward integration:

$$X = C \exp(-\beta x) \quad , \quad (\text{VII.12})$$

where C and β are constants.

For the z -direction dependence (VII.10), a solution is anticipated as a finite set of orthogonal functions

$$Z = A_n Z_n, \quad Z_n = \sin(\gamma_n z), \quad \gamma_n = \frac{2n-1}{2} \pi \quad (\text{VII.13})$$

that satisfy the boundary conditions

$$Z(0) = 0, \quad \frac{\partial Z}{\partial z}(1) = 0 \quad . \quad (\text{VII.14})$$

Inserting the series (VII.13) into (VII.10),

$$A_n Z_n'' + \beta \frac{F_1}{F_4} u A_n Z_n = \text{error} \quad , \quad (\text{VII.15})$$

necessary introduces an error into the approximation, due to the finite number of terms used in the series. As the *error* is also orthogonal to the set of basis function Z_n , multiplication by Z_m , ($m=1,n$) and further integration from 0 to 1 yields

$$A_n \int_0^1 Z_n'' Z_m dz + \beta_m \frac{F_1}{F_4} A_n \int_0^1 u Z_n Z_m dz = 0 \quad . \quad (\text{VII.16})$$

In matrix notation, the system of n equations given by (VII.16) can be written as an extended eigenvalue problem:

$$\left(I_{mn} + \beta_m \frac{F_1}{F_4} J_{mn} \right) A_n = 0 , \quad (\text{VII.17})$$

where I_{mn} and J_{mn} are integrals. The system of equations (VII.17) has a non-trivial solution, if

$$\text{Det} \left(I_{mn} + \beta_m \frac{F_1}{F_4} J_{mn} \right) = 0 . \quad (\text{VII.18})$$

From this condition the system eigenvalues β_m are determined. Each eigenvalue β_m then corresponds to a specific m vector of A_n .

Knowing β and A , the temperature field in channel flow can be represented by:

$$T_f = C_i X_i A_{in} Z_n , \quad (\text{VII.19})$$

where the coefficients C_i still must be determined. They are found from the initial condition $T_f(0, z) = 1$,

$$C_i A_{in} Z_n = 1 . \quad (\text{VII.20})$$

Following the same procedure by multiplying (VII.20) by Z_m , ($m=1,n$) and integrating from 0 to 1:

$$C_i A_{im} \int_0^1 Z_n Z_m dz = \int_0^1 Z_m dz \quad , \quad (\text{VII.21})$$

the orthogonality condition diagonalizes (VII.21) to

$$C_i A_{im} I_m = J_m \quad , \quad (\text{VII.22})$$

where I_m and J_m are integrals, respectively. Writing (VII.22) in a matrix form:

$$A_{im} C_i = \frac{J_m}{I_m} \quad , \quad (\text{VII.23})$$

coefficient vector C_i is calculated with inversion of the matrix system (VII.23).

VII.2 Porous Media Flow

The porous media transport equations are reduced to two dimensions as is done for channel flow. Further simplification is made by excluding the heat conductive base-plate from the calculation of temperature field. This approximation can be made, if the thickness of the base-plate is small and its heat conductivity is high enough. Using this

simplification, the lower thermal boundary is assumed to be isothermal.

Taking into account the spatial reduction, equation (VI.6) is written as

$$-M_2 \frac{\partial^2 u}{\partial z^2} + M_3 u^2 = M_4 , \quad (\text{VII.24})$$

where the velocity u changes in the vertical direction only. Furthermore, (VII.24) is linearized to

$$-M_2 \frac{\partial^2 u}{\partial z^2} + Ku = M_4 , \quad (\text{VII.25})$$

with $K = M_3 u$ being a constant. The boundary conditions for the velocity profile are:

$$u(0) = 0, \quad u(1) = 0 . \quad (\text{VII.26})$$

The solution to the momentum transport equation (VII.25) is expected to be of the form

$$u \sim \exp(\gamma z) , \quad (\text{VII.27})$$

where γ is a constant. Taking into account the boundary conditions given by (VII.26), the fluid velocity is:

$$u = A_1 \exp(\gamma z) + A_2 \exp(-\gamma z) + \frac{M_4}{K} , \quad (\text{VII.28})$$

where $\gamma = \sqrt{K/M_2}$, $A_1 = -\frac{M_4(1 - \exp(-\gamma))}{2K \sinh(\gamma)}$ and $A_2 = \frac{M_4(1 - \exp(\gamma))}{2K \sinh(\gamma)}$.

Neglecting thermal diffusion in the horizontal spanwise and streamwise directions, the energy transport equation for the fluid flow (VI.11) is written

$$F_1 u \frac{\partial T_f}{\partial x} = F_4 \frac{\partial^2 T_f}{\partial z^2} - F_5 (T_f - T_s) , \quad (\text{VII.29})$$

and the boundary conditions are:

$$T_f(0, z) = 1, \quad \frac{\partial T_f}{\partial x}(1, z) = 0, \quad (\text{VII.30})$$

$$T_f(x, 0) = 0, \quad \frac{\partial T_f}{\partial z}(x, 1) = 0 .$$

Heat transfer in the solid-phase is described with the separate energy transport equation given by (VI.16), repeated here for clarity,

$$0 = S_1 \frac{\partial^2 T_s}{\partial z^2} + S_2 (T_f - T_s) , \quad (\text{VII.31})$$

with the following boundary conditions:

$$T_s(x,0) = 0, \quad \frac{\partial T_s}{\partial z}(x,1) = 0. \quad (\text{VII.32})$$

where the lower boundary ($z = 0$) is taken as isothermal.

To find a solution to the system of energy transport equations (VII.30, VII.32), both equations are combined into the single expression:

$$uF_1 \frac{\partial T_s}{\partial x} + F_4 \frac{S_1}{S_2} \frac{\partial^4 T_s}{\partial z^4} - \left(F_5 \frac{S_1}{S_2} + F_4 \right) \frac{\partial^2 T_s}{\partial z^2} - uF_1 \frac{S_1}{S_2} \frac{\partial^3 T_s}{\partial x \partial z^2} = 0, \quad (\text{VII.33})$$

which can be written in more compact form as

$$D_1(z) \frac{\partial T_s}{\partial x} + D_2 \frac{\partial^4 T_s}{\partial z^4} - D_3 \frac{\partial^2 T_s}{\partial z^2} - D_4(z) \frac{\partial^3 T_s}{\partial x \partial z^2} = 0, \quad (\text{VII.34})$$

where $D_1(z) = uF_1$, $D_2 = F_4 S_1/S_2$, $D_3 = F_5 S_1/S_2 + F_4$ and $D_4(z) = uF_1 S_1/S_2$. Next, separation of variables in the following form is used to find a solution to (VII.34):

$$T_f = X(x)Z(z), \quad (\text{VII.35})$$

with boundary conditions

$$\begin{aligned} X(0) &= 1, \quad \frac{\partial X}{\partial x}(1) = 0, \\ Z(0) &= 0, \quad \frac{\partial Z}{\partial z}(1) = 0. \end{aligned} \quad (\text{VII.36})$$

When (VII.35) is inserted into (VII.34), following differential equation is obtained:

$$D_1 Z X' + D_2 Z^{IV} X - D_3 Z'' X - D_4 Z'' X' = 0. \quad (\text{VII.37})$$

A solution to the z -direction of (VII.34) is anticipated to be a finite set of orthogonal functions:

$$Z = A_n Z_n, \quad Z_n = \sin(\gamma_n z), \quad \gamma_n = \frac{2n-1}{2} \pi, \quad (\text{VII.38})$$

that satisfy boundary conditions (VII.36). Introducing (VII.38) into (VII.37) brings us to

$$D_1 X'(A_n Z_n) + D_2 X(A_n \gamma_n^4 Z_n) + D_3 X(A_n \gamma_n^2 Z_n) + D_4 X'(A_n \gamma_n^2 Z_n) = \text{error}, \quad (\text{VII.39})$$

and in a more compact form

$$X^l A_n \{D_1 + \gamma_n^2 D_4\} Z_n + X A_n \{\gamma_n^4 D_2 + \gamma_n^2 D_3\} Z_n = error . \quad (\text{VII.40})$$

As the series is finite, there is a certain discrepancy associated with the expansion. This *error* is orthogonal to the set of function used for the expansion and can be reduced with multiplication by Z_m , ($m=1,n$) and further integration from 0 to 1:

$$X^l A_n \int_0^1 \{D_1 + \gamma_n^2 D_4\} Z_n Z_m dz + X A_n \int_0^1 \{\gamma_n^4 D_2 + \gamma_n^2 D_3\} Z_n Z_m dz = 0 . \quad (\text{VII.41})$$

In more compact form, (VII.41) is written as

$$X^l A_n I_{nm} + X A_n J_{nm} = 0 , \quad (\text{VII.42})$$

where I_{nm} and J_{nm} are z dependent integrals. As the x and z dependent parts of (VII.42) can be separated:

$$\beta = -\frac{X^l}{X_m} = \frac{A_n J_{nm}}{A_n I_{nm}} , \quad (\text{VII.43})$$

a separate equation can be written for the x -direction:

$$X_m^l + \beta_m X_m = 0 , \quad (\text{VII.44})$$

and for the z -direction:

$$A_n J_{nm} - \beta_m A_n I_{nm} = 0 . \quad (\text{VII.45})$$

The solution of (VII.45) is obtained by integration:

$$X_m = C \exp(-\beta_m x) , \quad (\text{VII.46})$$

where C and β_m are arbitrary constants. Rearranging (VII.45), an extended eigenvalue problem can be formed as

$$(J_{nm} - \beta_m I_{nm}) A_n = 0 . \quad (\text{VII.47})$$

The system of equations (VII.47) has a non-trivial solution, if

$$\text{Det}(J_{mn} - \beta_m I_{mn}) = 0 . \quad (\text{VII.48})$$

From this condition, the system eigenvalues β_m are determined. Furthermore, each eigenvalue β_m corresponds to a specific m vector of A_n .

Using solutions of (VII.44, VII.48), one can construct the solid structure temperature field:

$$T_s = C_i X_i A_{in} Z_n , \quad (\text{VII.49})$$

and, by reintroducing (VII.31), the fluid temperature field is given by

$$T_f = C_i X_i A_{in} \left(1 + \frac{S_1}{S_2} \gamma_n^2 \right) Z_n . \quad (\text{VII.50})$$

The coefficients C_i are found from the initial condition $T_f(0,z)=1$:

$$C_i A_{in} \left(1 + \frac{S_1}{S_2} \gamma_n^2 \right) Z_n = 1 . \quad (\text{VII.51})$$

Again, using the same procedure, multiplying (VII.51) by Z_m , ($m=1,n$) and integrating from 0 to 1:

$$C_i A_{in} \left(1 + \frac{S_1}{S_2} \gamma_n^2 \right) \int_0^1 Z_n Z_m dz = \int_0^1 Z_m dz , \quad (\text{VII.52})$$

the orthogonality condition reduces (VII.52) to

$$C_i A_{im} \left(1 + \frac{S_1}{S_2} \gamma_m^2 \right) I_m = J_m \quad , \quad (\text{VII.53})$$

where I_m and J_m are integrals, respectively. Writing (VII.53) in a matrix form:

$$A_{im} C_i = \frac{J_m}{\left(1 + \frac{S_1}{S_2} \gamma_m^2 \right) I_m} \quad , \quad (\text{VII.54})$$

the unknown coefficients C_i are calculated with inversion of the matrix system (VII.54).

VIII. Finite Volume Solution Method

The Finite Volume Method (FVM) is much more robust than the Galerkin Method (GM), allowing the transport equations for porous media flow (VI.6, VI.11, VI.16, VI.21) to be solved without additional simplifications.

The momentum transport equation (VI.6):

$$-M_1 \frac{\partial^2 u}{\partial y^2} - M_2 \frac{\partial^2 u}{\partial z^2} + M_3 u^2 = M_4, \quad (\text{VIII.1})$$

with boundary conditions:

$$\begin{aligned} u(0, z) &= 0, & u(1, z) &= 0, \\ u(y, 0) &= 0, & u(y, 1) &= 0, \end{aligned} \quad (\text{VIII.2})$$

is discretized using the central-difference scheme in both spanwise directions (y- and z-direction).

$$\begin{aligned}
& -\left(\frac{M_1}{\Delta y} \Delta z\right) u^{n+1}(j-1, k) - \left(\frac{M_1}{\Delta y} \Delta z\right) u^{n+1}(j+1, k) \\
& -\left(\frac{M_2}{\Delta z} \Delta y\right) u^{n+1}(j, k-1) - \left(\frac{M_2}{\Delta z} \Delta y\right) u^{n+1}(j, k+1) \\
& + \left(\frac{2M_1}{\Delta y} \Delta z + \frac{2M_2}{\Delta z} \Delta y + M_3 u^n(j, k) \Delta y \Delta z\right) u^{n+1}(j, k) = (M_4 \Delta y \Delta z)
\end{aligned} \tag{VIII.3}$$

Although the matrix (VIII.3) is symmetrical, it has non-constant terms on the central diagonal, due to non-linearity arising from the drag force term.

Similarly, the energy transport equation for fluid flow (VI.11):

$$F_1 u \frac{\partial T_f}{\partial x} = F_2 \frac{\partial^2 T_f}{\partial x^2} + F_3 \frac{\partial^2 T_f}{\partial y^2} + F_4 \frac{\partial^2 T_f}{\partial z^2} - F_5 (T_f - T_s) , \tag{VIII.4}$$

with boundary conditions

$$\begin{aligned}
T_f(0, y, z) &= 1, & \frac{\partial T_f}{\partial x}(1, y, z) &= 0, \\
\frac{\partial T_f}{\partial y}(x, 0, z) &= 0, & \frac{\partial T_f}{\partial y}(x, 1, z) &= 0, \\
T_f(x, y, 0) &= T_{if}(x, y, 0), & \frac{\partial T_f}{\partial z}(x, y, 1) &= 0,
\end{aligned} \tag{VIII.5}$$

is discretized in all three dimension (x -, y - and z -direction) using the central-difference

scheme for diffusion terms and the upwind scheme for convection term, respectively.

This yields:

$$\begin{aligned}
& - \left(F_1 u^n(j,k) \Delta y \Delta z + \frac{F_2}{\Delta x} \Delta y \Delta z \right) T_f^{n+1}(i-1,j,k) - \left(\frac{F_2}{\Delta x} \Delta y \Delta z \right) T_f^{n+1}(i+1,j,k) \\
& - \left(\frac{F_3}{\Delta y} \Delta x \Delta z \right) T_f^{n+1}(i,j-1,k) - \left(\frac{F_3}{\Delta y} \Delta x \Delta z \right) T_f^{n+1}(i,j+1,k) \\
& - \left(\frac{F_4}{\Delta z} \Delta x \Delta y \right) T_f^{n+1}(i,j,k-1) - \left(\frac{F_4}{\Delta z} \Delta x \Delta y \right) T_f^{n+1}(i,j,k+1) \\
& + \left(F_1 u^n(j,k) \Delta y \Delta z + \frac{2F_2}{\Delta x} \Delta y \Delta z + \frac{2F_3}{\Delta y} \Delta x \Delta z + \frac{2F_4}{\Delta z} \Delta x \Delta y + F_5 \Delta x \Delta y \Delta z \right) T_f^{n+1}(i,j,k) = \\
& = \left(F_5 T_s^n(i,j,k) \Delta x \Delta y \Delta z \right)
\end{aligned} \tag{VIII.6}$$

In this case, the resulting seven-diagonal matrix system (VIII.6) is not symmetrical, due to the upwind discretization, nor does it have constant terms, due to the locally changing heat transfer coefficient h and consequently changing F_5 .

The energy transport equation for the solid structure (VI.16),

$$0 = S_1 \frac{\partial^2 T_s}{\partial z^2} + S_2 (T_f - T_s) \quad , \tag{VIII.7}$$

with boundary conditions

$$T_s(x, y, 0) = T_f(x, y, 0), \quad \frac{\partial T_s}{\partial z}(x, y, 1) = 0 \quad , \tag{VIII.8}$$

is discretized in the vertical (z -direction) using the central-difference scheme:

$$\begin{aligned} & -\left(\frac{S_1}{\Delta z} \Delta x \Delta y\right) T_s^{n+1}(i, j, k-1) - \left(\frac{S_1}{\Delta z} \Delta x \Delta y\right) T_s^{n+1}(i, j, k+1) \\ & + \left(\frac{2S_1}{\Delta z} \Delta x \Delta y + S_2 \Delta x \Delta y \Delta z\right) T_s^{n+1}(i, j, k) = \left(S_2 T_f^n(i, j, k) \Delta x \Delta y \Delta z\right) \end{aligned} \quad (\text{VIII.9})$$

The three-diagonal matrix (VIII.9) is symmetric with varying diagonal terms as a result of local variations in the heat transfer coefficient h and therefore in S_2 .

The central-difference scheme is also used to discretize the energy diffusion transport equation for the solid base-plate (VI.21),

$$0 = B_1 \frac{\partial^2 T_b}{\partial x^2} + B_2 \frac{\partial^2 T_b}{\partial y^2} + B_3 \frac{\partial^2 T_b}{\partial z^2} , \quad (\text{VIII.10})$$

with boundary conditions in all three-dimensions (x -, y - and z - direction),

$$\begin{aligned} \frac{\partial T_b}{\partial x}(0, y, z) = 0, \quad \frac{\partial T_b}{\partial x}(1, y, z) = 0, \\ \frac{\partial T_b}{\partial y}(x, 0, z) = 0, \quad \frac{\partial T_b}{\partial y}(x, 1, z) = 0, \\ T_b(x, y, -1) = 0, \quad \frac{\partial T_b}{\partial z}(x, y, 0) = \alpha_f \left(\frac{\hat{\lambda}_f}{\hat{\lambda}_s} \right) \frac{\partial T_f}{\partial z} + \alpha_s \frac{\partial T_s}{\partial z} , \end{aligned} \quad (\text{VIII.11})$$

to obtain the following:

$$\begin{aligned}
& -\left(\frac{B_1}{\Delta x} \Delta y \Delta z_b\right) T_b^{n+1}(i-1, j, k) - \left(\frac{B_1}{\Delta x} \Delta y \Delta z_b\right) T_b^{n+1}(i+1, j, k) \\
& -\left(\frac{B_2}{\Delta y} \Delta x \Delta z_b\right) T_b^{n+1}(i, j-1, k) - \left(\frac{B_2}{\Delta y} \Delta x \Delta z_b\right) T_b^{n+1}(i, j+1, k) \\
& -\left(\frac{B_3}{\Delta z_b} \Delta x \Delta y\right) T_b^{n+1}(i, j, k-1) - \left(\frac{B_3}{\Delta z_b} \Delta x \Delta y\right) T_b^{n+1}(i, j, k+1) \\
& + \left(\frac{2F_1}{\Delta x} \Delta y \Delta z_b + \frac{2F_2}{\Delta y} \Delta x \Delta z_b + \frac{2F_3}{\Delta z_b} \Delta x \Delta y\right) T_b^{n+1}(i, j, k) = 0
\end{aligned} \tag{VIII.12}$$

The resulting seven-diagonal matrix (VIII.12) is basically symmetrical. Nevertheless, the symmetry is spoiled due to the coupled boundary conditions on the top (VIII.8).

The system of discrete non-linear and asymmetric equations (VIII.3, VIII.6, VIII.9, VIII.12) is solved with an iteration procedure, where the Precondition Conjugate Gradient (PCG) method is applied as an elliptic-hyperbolic equation solver. The detailed description of PCG can be found in Ferziger and Perić (1996).

IX. Interphase Transfer Coefficients

In order to close the porous media transport equations (VI.6, VI.11, VI.16, VI.21) the interphase transfer coefficients like the local drag coefficient C_d (III.10) and the local heat transfer coefficient h (III.17) have to be determined. In the present case these coefficients are grouped into parameters M_3 (or K), F_5 and S_2 , which are therefore dependent on local flow conditions. Thus, the drag coefficient C_d and heat transfer coefficient h are functions of local Reynolds number Re_h , which is defined as

$$Re_h = \frac{\hat{u} \hat{d}_h}{\hat{v}_f} . \quad (\text{IX.1})$$

These coefficients can be determined from the Direct Numerical Simulation (DNS) or from the Large-Eddy Simulation (LES) of flow through REV. Likewise, the available experimental data can be used to obtain needed drag and heat transfer coefficients.

IX.1 Drag Coefficient

In the present work the experimental data from Lauder and Massey (1978) are used to construct a correlation for the local drag coefficient C_d as a function of the local Reynolds number Re_h :

for $Re_h \leq 126$,

$$f = 2 \cdot 10^{0.224581} \left(\frac{\hat{V}_f \hat{d}}{\hat{p}_x \hat{A}_{max} \hat{d}_h} Re_h \right)^{-0.644771}, \quad (IX.2)$$

$$C_d = 4 \frac{\hat{p}_y}{\pi \hat{d}} \left(\frac{\hat{V}_f}{\hat{p}_x \hat{A}_{max}} \right)^2 f,$$

where A_{max} is the maximum velocity flow area. In this case A_{max} is between pin-fins, diagonal to streamwise direction.

For higher Reynolds number the experimental data from Kay and London (1998) are applied for the same purpose:

for $Re_h > 126$,

$$f = 0.41 \left(\frac{4\hat{V}_f}{\pi \hat{d} \hat{h} \hat{d}_h} Re_h \right)^{-0.18}, \quad (IX.3)$$

$$C_d = \frac{\hat{p}_y \hat{h}}{\hat{A}_{max}} \left(\frac{\hat{V}_f}{\hat{p}_x \hat{A}_{max}} \right)^2 f.$$

IX.2 Heat Transfer Coefficient

A correlation based on the experimental data from Žukauskas and Ulinskas (1985) is used for the local heat transfer coefficient h at low Reynolds numbers Re_h :

$$\text{for } Re_h \leq 133, \quad h = 1.04 Pr^{0.36} \frac{\hat{\lambda}_f}{\hat{d}} \left(\frac{\hat{V}_f \hat{d}}{\hat{p}_x \hat{A}_{max} \hat{d}_h} Re_h \right)^{0.4}, \quad (\text{IX.4})$$

whereas for higher Reynolds numbers Re_h , the experimental data from Kay and London (1984) are more appropriate :

$$\text{for } Re_h > 133, \quad h = 0.41 Pr^{\frac{1}{3}} \frac{\hat{\lambda}_f \pi d h}{4 \hat{A}_{max} \hat{p}_x} \left(\frac{4 \hat{V}_f}{\pi \hat{d} \hat{d}_h} Re_h \right)^{0.6}. \quad (\text{IX.5})$$

X. Results

Simulations of the heat sink thermal behavior were performed for the pressure drops Δp and the boundary temperatures T_{in} and T_g summarized in tables X-1, X-2 and X-3. Calculations were performed at heating powers of 50W, 125W and 220W to match the experimental data obtained by Rizzi et al., 2001.

Table X-1: Boundary conditions at heating power $Q = 50\text{W}$.

No.	$\Delta p[\text{Pa}]$	$T_{in} [^{\circ}\text{C}]$	$T_g [^{\circ}\text{C}]$
1	5.0	23.00	54.90
2	10.0	23.00	43.43
3	20.0	23.00	37.20
4	40.0	23.00	33.00

No.	$\Delta p[\text{Pa}]$	$T_{in} [^{\circ}\text{C}]$	$T_g [^{\circ}\text{C}]$
5	74.72	23.02	30.30
6	175.6	23.02	27.90
7	266.5	23.04	27.30
8	368.6	22.90	26.64

Table X-2: Boundary conditions at heating power $Q = 125\text{W}$.

No.	$\Delta p[\text{Pa}]$	$T_{in} [^{\circ}\text{C}]$	$T_g [^{\circ}\text{C}]$
1	5.0	23.00	103.8
2	10.0	23.00	74.60
3	20.0	23.00	58.80
4	40.0	23.00	48.15

No.	$\Delta p[\text{Pa}]$	$T_{in} [^{\circ}\text{C}]$	$T_g [^{\circ}\text{C}]$
5	74.72	23.16	41.80
6	179.3	23.21	35.73
7	274.0	23.05	33.60
8	361.1	22.81	32.25

Table X-3: Boundary conditions at heating power $Q = 220\text{W}$.

No.	$\Delta p[\text{Pa}]$	$T_{in} [^{\circ}\text{C}]$	$T_g [^{\circ}\text{C}]$
1	5.0	23.00	168.0
2	10.0	23.00	114.8
3	20.0	23.00	87.00
4	40.0	23.00	68.00

No.	$\Delta p[\text{Pa}]$	$T_{in} [^{\circ}\text{C}]$	$T_g [^{\circ}\text{C}]$
5	74.72	23.07	56.40
6	180.6	22.96	45.20
7	280.2	22.97	42.30
8	361.1	22.90	40.40

X.1 Comparison of Whole-Section Values

The imposed pressure drop Δp causes airflow through the heated solid structure. As the structure is cooled, a steady temperature field is formed in the airflow as well as in the thermal conductive aluminum. Based on the calculated velocity and temperature fields, the whole-section drag coefficient

$$\overline{C}_d = \frac{2\Delta\hat{p}}{\hat{\rho}_f (\overline{\hat{u}})^2 \hat{L}\hat{S}}, \quad (\text{X.1})$$

and the whole-section Nusselt number

$$\overline{Nu} = \frac{\hat{Q}\hat{d}_h}{(\hat{T}_g - \hat{T}_{in})\hat{A}_g \hat{\lambda}_f}, \quad (\text{X.2})$$

are estimated as functions of Reynolds number Re_h , where the definition (IX.1) is based on a hydraulic diameter d_h of a hypothetical porous media channel.

Similarly, the thermal effectiveness Q/W , which is defined as the ratio between the heat transferred through the structure

$$\hat{Q} = \alpha_f \hat{p}_f \hat{c}_f \hat{u} (\bar{T}_{out} - \bar{T}_{in}) \hat{A}_\perp, \quad (\text{X.3})$$

and the mechanical pumping power expended to overcome fluid friction

$$\hat{W} = \alpha_f \Delta \hat{p} A_\perp \hat{u}, \quad (\text{X.4})$$

is obtained from the calculated velocity and temperature fields.

The whole-section values of the drag coefficient C_d , the Nusselt number Nu and the thermal effectiveness Q/W , calculated from Finite Volume Method (FVM) and Galerkin Method (GM) simulation results, are compared with the experimental data, which were taken in the Morrin-Martinelli-Gier Memorial Heat Transfer Laboratory at the University of California, Los Angeles (Rizzi et al., 2001). As the experimental methods cannot give a detailed picture of velocity and temperature fields, the comparisons of these whole-section values serve as the verification of the constructed physical model and validate the developed numerical code.

X.1.1 Thermal Power 50 W

Figures X-1, X-2 and X-3 show the whole-section drag coefficient C_d , the whole-section Nusselt number Nu and the test section thermal effectiveness Q/W as a function of Reynolds number Re_h at a thermal power of 50W.

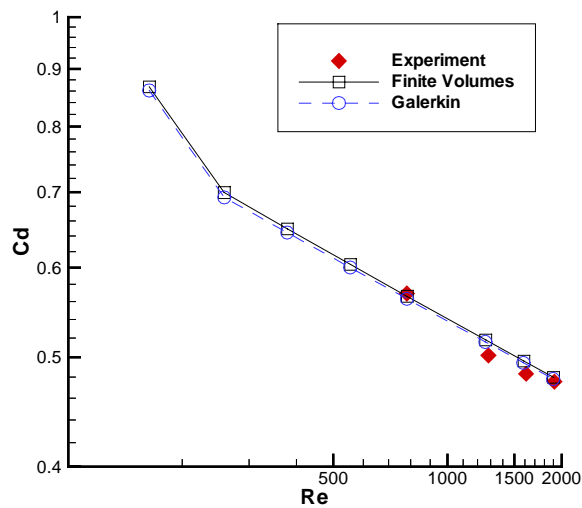


Figure X-1: Whole-section drag coefficient C_d , 50W of thermal power.

Figure X-1 shows that the results calculated with FVM (marked with Finite Volumes) are close to the results obtained by GM (marked with Galerkin) as well to experimental data (marked with Experiment). Slight discrepancy from the experimental data at higher Reynolds number is due to transition to turbulence, which is evident on experimental results, but does not influence the model.

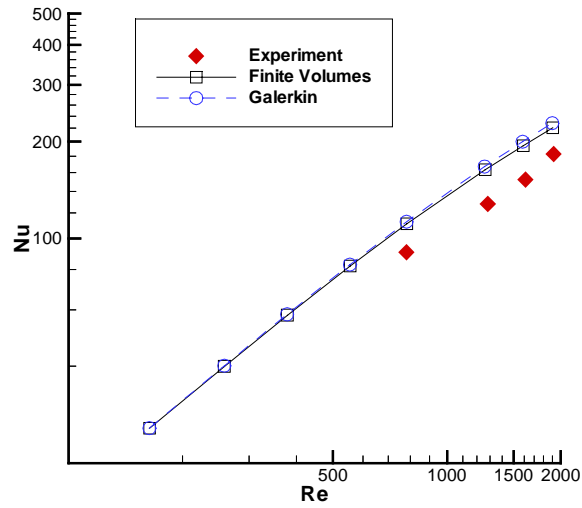


Figure X-2: Whole-section Nusselt number Nu , 50W of thermal power.

The Nusselt number Nu distributions in fig. X-2 show larger difference between the FVM and GM results on one side and the experimental data on the other. The difference of approximately 10% is steady throughout the whole range of tested Reynolds numbers. As the difference cannot be observed at higher thermal power (fig. X-5, fig. X-8), it is suspected to be a consequence of systematic modeling or experimental error.

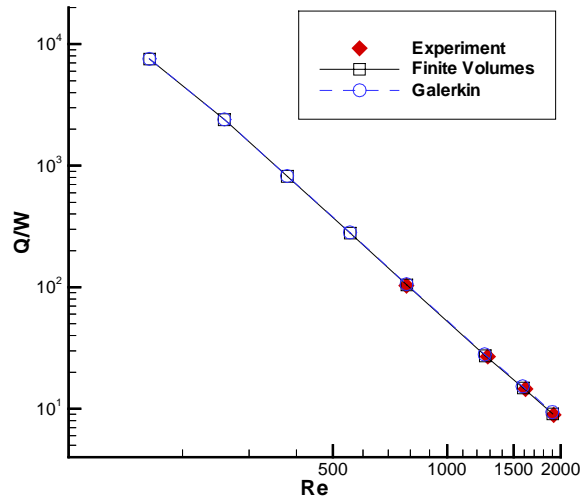


Figure X-3: Test section thermal effectiveness Q/W , 50W of thermal power.

The thermal effectiveness Q/W in fig. X-3 decreases with increasing Reynolds number Re_h . The comparison of results shows again an excellent agreement between the FVM and GM results and the experimental data.

X.1.2 Thermal Power 125 W

Figures X-4, X-5 and X-6 show the whole-section drag coefficient C_d , the whole-section Nusselt number Nu and the test section thermal effectiveness Q/W as a function of Reynolds number Re_h at a thermal power of 125W.

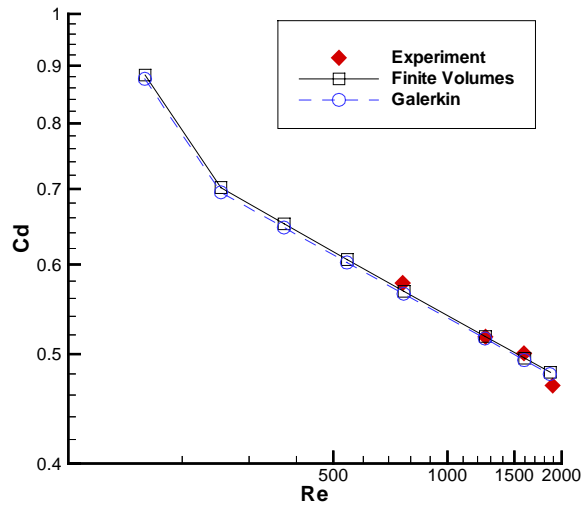


Figure X-4: Whole-section drag coefficient C_d , 125W of thermal power.

Figure X-4 shows good agreement between the FVM and GM results and the experimental data. The difference is visible only at the last experimental point ($Re_h = 1912$), where the transition effects are already present.

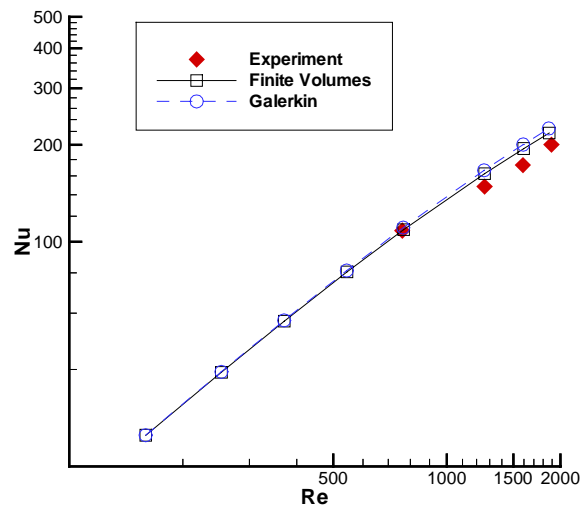


Figure X-5: Whole-section Nusselt number Nu , 125W of thermal power.

The calculated whole-section Nusselt number in fig. X-5 shows only a minor difference of approximately 5% between calculations and the experimental data as the Reynolds number increases from $Re_h = 762$ to $Re_h = 1893$.

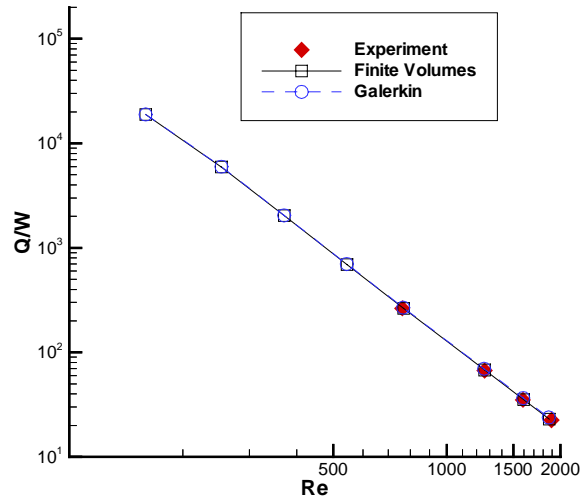


Figure X-6: Test section thermal effectiveness Q/W , 125W of thermal power.

As in the previous case, the calculated thermal effectiveness Q/W shows practically no discrepancy from experimental data (Rizzi et al., 2001).

X.1.3 Thermal Power 220 W

Figures X-7, X-8 and X-9 show the whole-section drag coefficient C_d , the whole-section Nusselt number Nu and the test section thermal effectiveness Q/W as a function of Reynolds number Re_h at a thermal power of 220W.

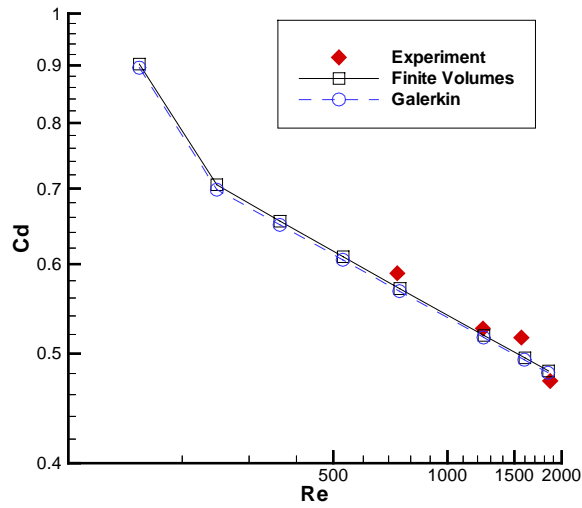


Figure X-7: Whole-section drag coefficient C_d , 220W of thermal power.

Although fig. X-7 still shows a good agreement between both models and experimental data, larger discrepancies are already visible. Namely, at thermal power 220W the air-flow through the heat sink is strongly influenced by thermal stratification, due to intensive heating at the bottom. The resulting buoyancy effects cause model deficiencies as well as problems with representation of collected experimental data.

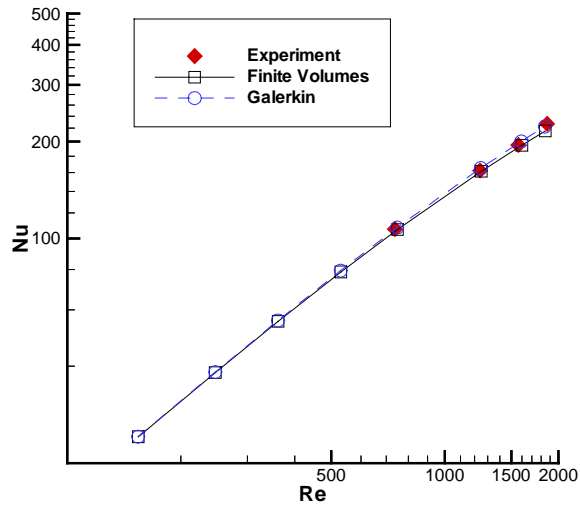


Figure X-8: Whole-section Nusselt number, 220W of thermal power.

The calculated values of the whole-section Nusselt number Nu in fig. X-8 and the test section thermal effectiveness Q/W in fig. X-9 show excellent agreement with the experimental data, where no systematic discrepancy is visible.

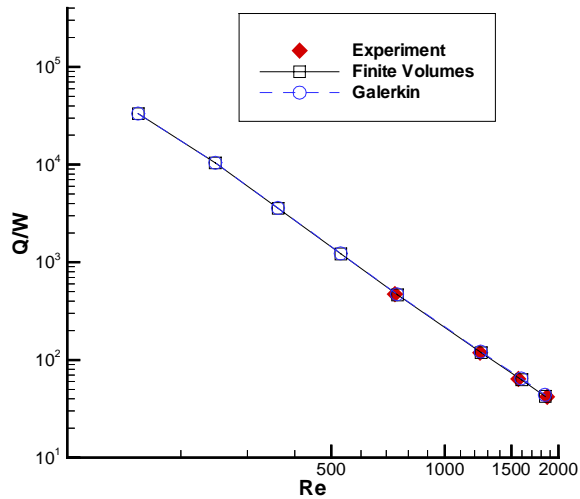


Figure X-9: Test section thermal effectiveness Q/W , 220W of thermal power.

X.2 Temperature Distribution in Heat Sink

The detailed temperature field at different Reynolds number Re_h , gives an insight into the heat transfer conditions in the studied heat sink. When FVM is used to calculate three-dimensional velocity and temperature fields in the air-flow and the solid structure, 34 x 34 x 140 mesh points are used in x -, y - and z -direction, respectively. For simulation of diffusion heat transfer in the solid base-plate 60 x 34 x 140 mesh points are used. When calculations are made with the two-dimensional GM, 34 x 140 mesh points are used in x - and z - direction to simulate heat transfer processes in fluid- and solid-phase. As the accuracy of the semi-analytical GM is essentially determined by the number of orthogonal function used for expansion (VII.38), 45 basis function are used in all presented cases.

It should be also noted that although different heating power (50W, 125W or 220W) is used on the base-plate, there exists a similarity in forced convection heat removal from the heat sink structure. Namely, higher heat input causes higher absolute temperature levels, whereas the form of isotherms changes only slightly, due to modification in air material properties. Therefore, this chapter presents the velocity profiles and temperature fields only for thermal power of 125 W. The complete set of calculation results is given in appendices A, B and C.

Figures X-10 and X-11 give velocity profiles of the air-flow at the middle of simulation domain ($y = 0.5W$) at different Reynolds numbers Re_h . The velocity profiles in fig. X-10 are calculated with two-dimensional GM, whereas the velocity profiles in fig. X-11 are obtained with three-dimensional FVM.

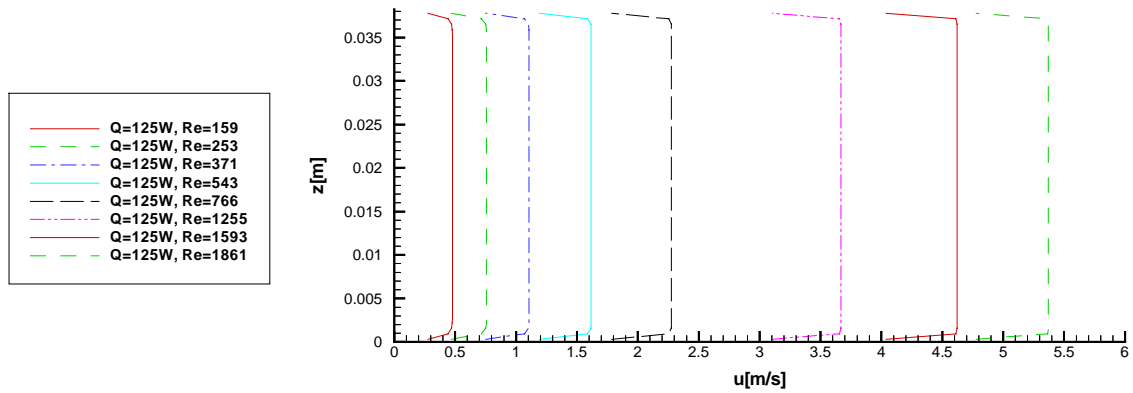


Figure X-10: Fluid velocity cross-section, $Q = 125W$, GM.

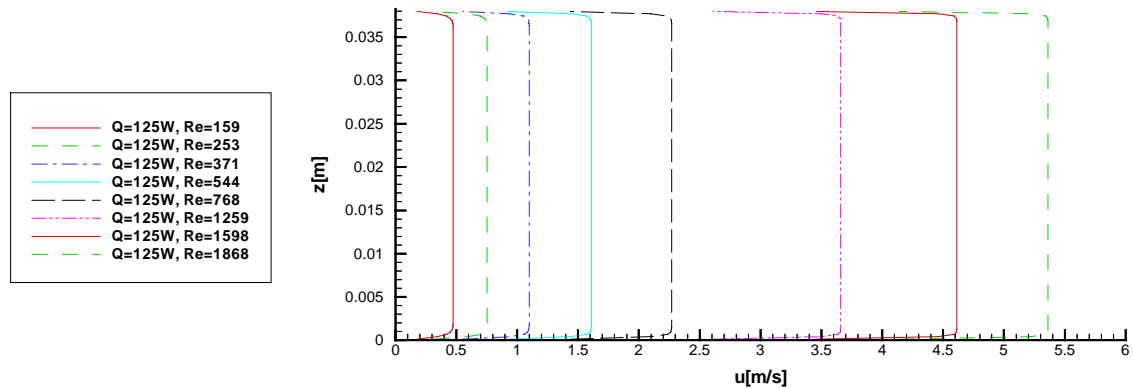
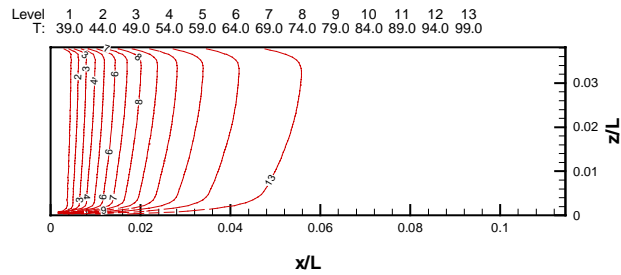


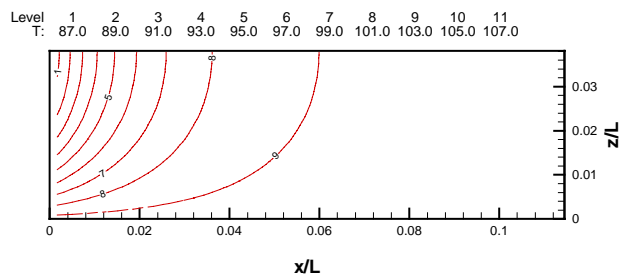
Figure X-11: Fluid velocity cross-section, $Q = 125W$, FVM.

As is evident, the absolute velocity in both calculations is the same. Nevertheless, GM (fig. X-10) cannot correctly resolve the boundary layer. Compare to FVM (fig. X-11) it over-predicts the thickness and therefore reduces the wall friction.

Figures from X-12 to X-25 show the temperature field cross-sections at different Reynolds numbers Re_h . The temperatures are in Celsius scale. Cross-sections of temperature field are taken at the middle of the simulation domain, $y = 0.5W$. The spatial coordinates x and y are given in meters, with L having a unit value.

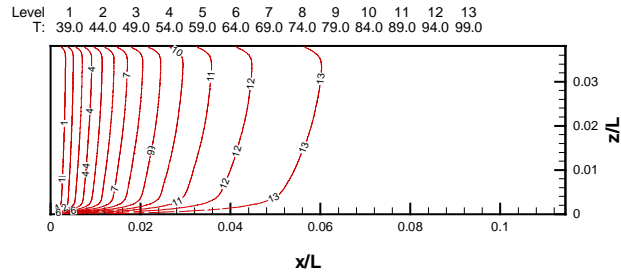


(a)

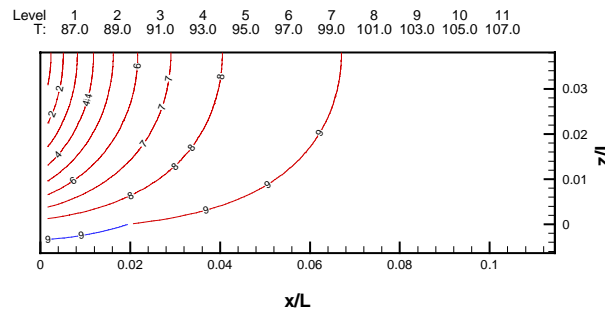


(b)

Figure X-12: Temperature field in fluid (a) and in solid (b), $Re_h = 159$, $Q = 125W$, GM.



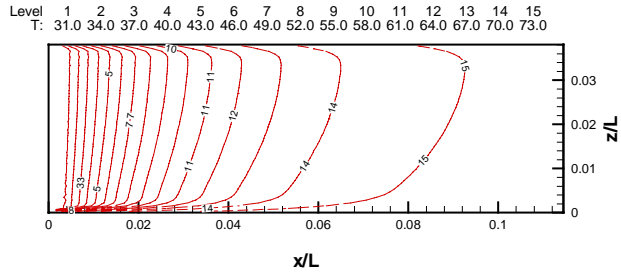
(a)



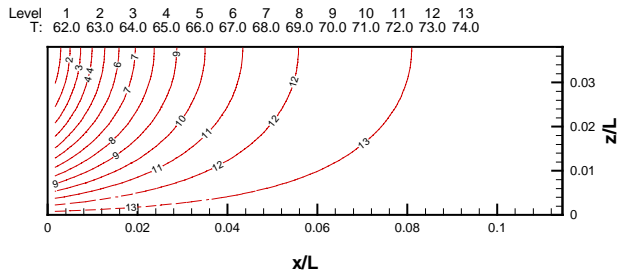
(b)

Figure X-13: Temperature field in fluid (a) and in solid (b), $Re_h = 159$, $Q = 125\text{W}$, FVM.

Figs X-12 and X-27 show that the lowest temperature in the air-stream is at the beginning of the heat sink; this is on the left side. The temperature raises as the air passes through the heat exchanging structure. Therefore, the highest temperatures are expected at the exit; this is on the right side. The temperature field in the solid structure is more horizontally stratified as the heat enters the structure from the bottom. As a consequence, the lowest temperature in the solid phase is in the upper left corner and the highest on the bottom, close to the base-plate.

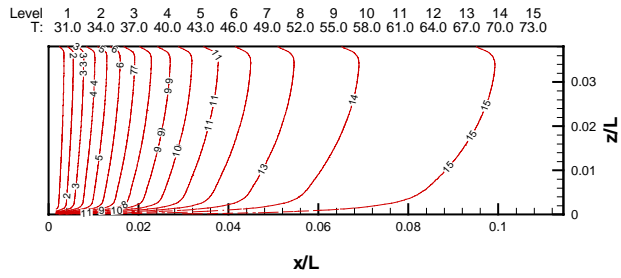


(a)

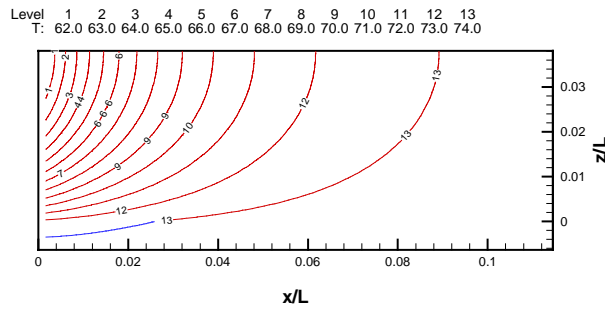


(b)

Figure X-14: Temperature field in fluid (a) and in solid (b), $Re_h = 253$, $Q = 125W$, GM.



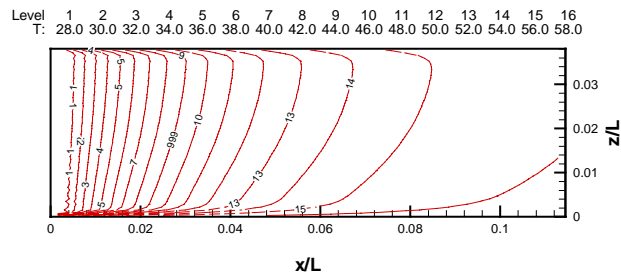
(a)



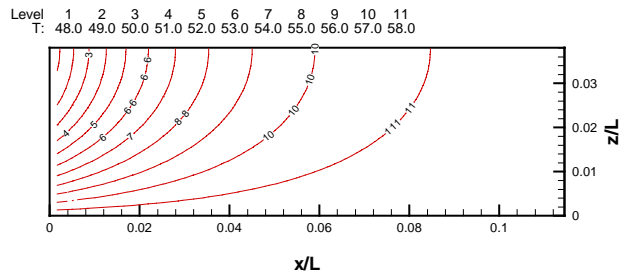
(b)

Figure X-15: Temperature field in fluid (a) and in solid (b), $Re_h = 253$, $Q = 125W$, FVM.

In fig. X-14, the temperature fields in the fluid flow (a) and the solid structure (b) obtained with GM are presented. For comparison fig. X-15 presents temperature field calculated with FVM, where thermal conduction in the base-plate is also included. Comparing figs. X-14 and X-15, it can be observed that the form of isotherms as well as the absolute temperatures are close together. Larger differences occur close to the bottom due to different thermal boundary conditions.

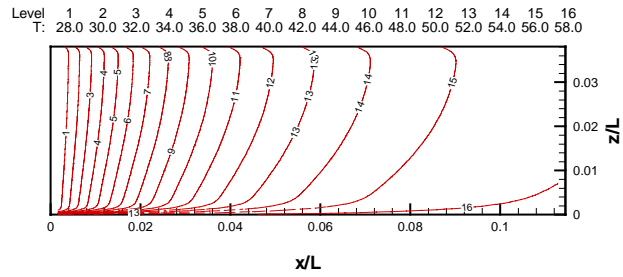


(a)

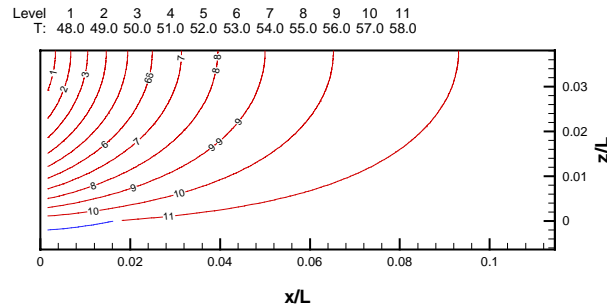


(b)

Figure X-16: Temperature field in fluid (a) and in solid (b), $Re_h = 371$, $Q = 125W$, GM.



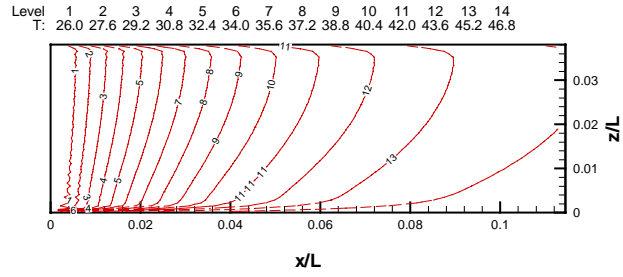
(a)



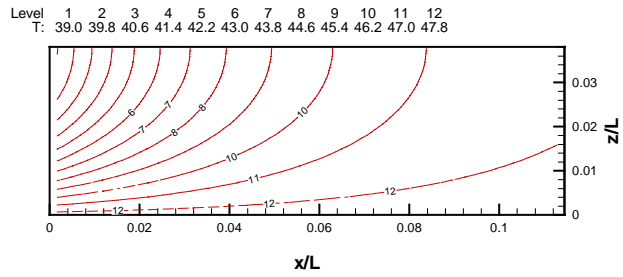
(b)

Figure X-17: Temperature field in fluid (a) and in solid (b), $Re_h = 371$, $Q = 125W$, FVM.

Because the heat flux is a vector perpendicular to the isotherms, a qualitative picture of heat flow can be extracted from the calculated temperature fields. It can be seen from figs. X-16 and X-17 that most of the heat is transferred from the solid to fluid in the first half of the test section. The highest heat fluxes appear in the lower left corner, where the temperature gradients are the largest. The second half of the heat sink still does not participate in the heat transfer process.

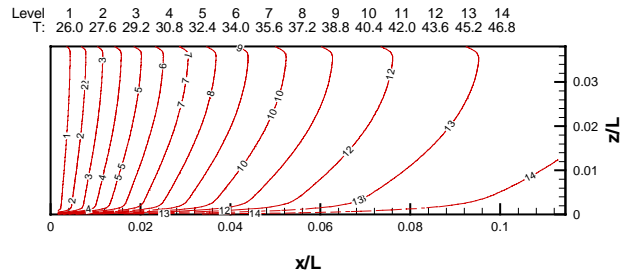


(a)

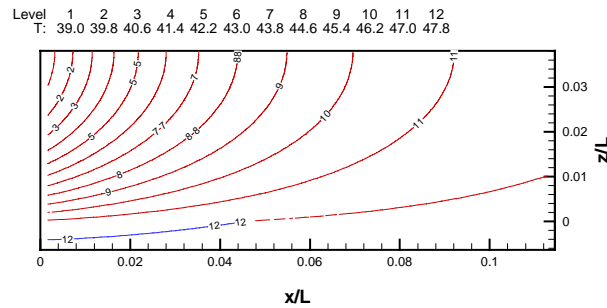


(b)

Figure X-18: Temperature field in fluid (a) and in solid (b), $Re_h = 543$, $Q = 125W$, GM.



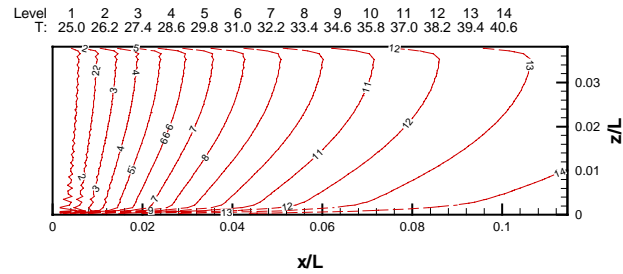
(a)



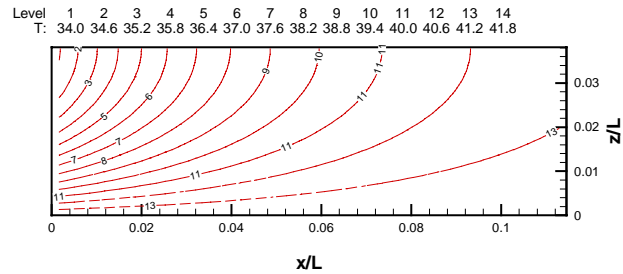
(b)

Figure X-19: Temperature field in fluid (a) and in solid (b), $Re_h = 544$, $Q = 125W$, FVM.

Figs. X-12 to X-19 reveal that at low Reynolds number Re_h , the temperature field is not fully developed. This means that the air, which enters the test section, is quickly heated due to its low velocity and leaves the heat sink at the temperature of the solid phase, unable to receive additional heat from the source. With increasing Reynolds number Re_h the state of thermal saturation diminishes (figs. X-18 and X-19). This heat transfer process also reduces the thermal effectiveness Q/W , presented on diagrams X-3, X-6 and X-9, as Reynolds number Re_h increases.

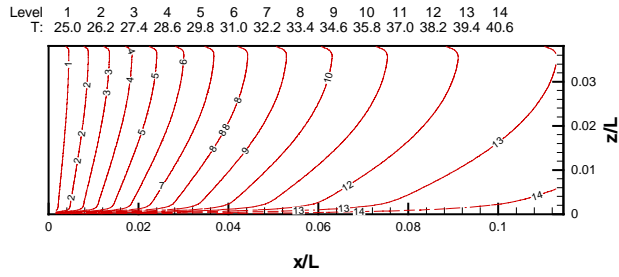


(a)

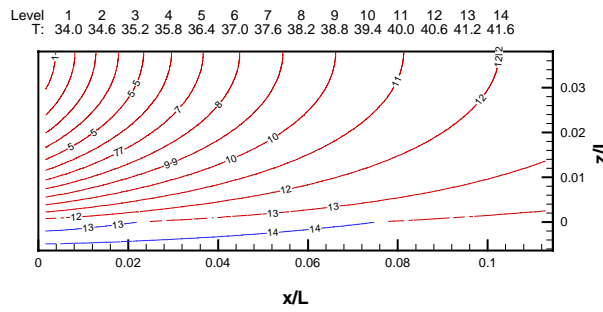


(b)

Figure X-20: Temperature field in fluid (a) and in solid (b), $Re_h = 766$, $Q = 125W$, GM.



(a)



(b)

Figure X-21: Temperature field in fluid (a) and in solid (b), $Re_h = 768$, $Q = 125W$, FVM.

The coolant flow lowers the temperature of heat conducting structure unequally. This directly changes the form of isotherms. The effect is not so evident at low Reynolds numbers (figs. X-12 to X-19). On the contrary, when the Reynolds number Re_h increases (figs. X-20 and X-21), the isotherms becomes tilted showing the increasing vertical thermal stratification of the coolant flow.

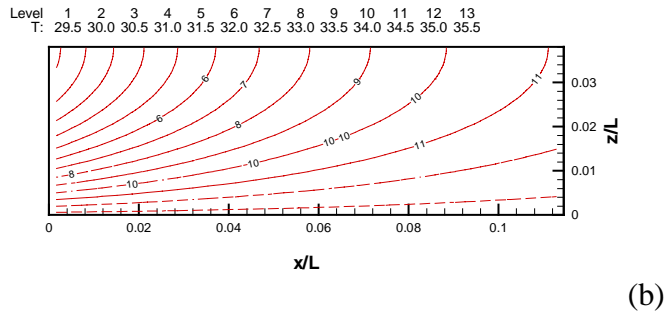
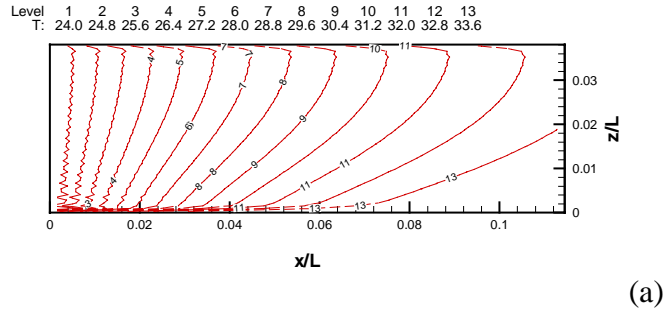


Figure X-22: Temperature field in fluid (a) and in solid (b), $Re_h = 1255$, $Q = 125W$, GM.

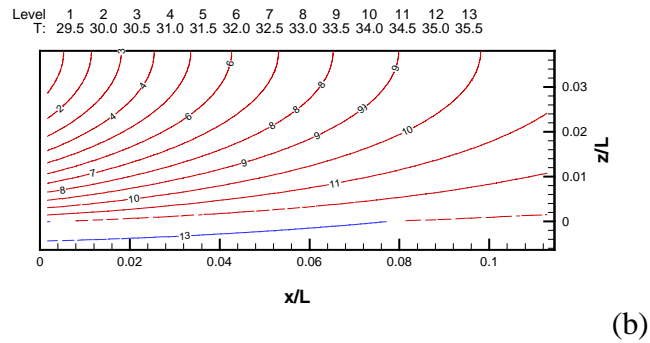
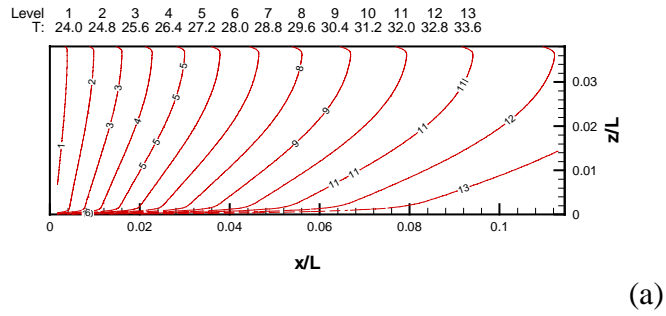
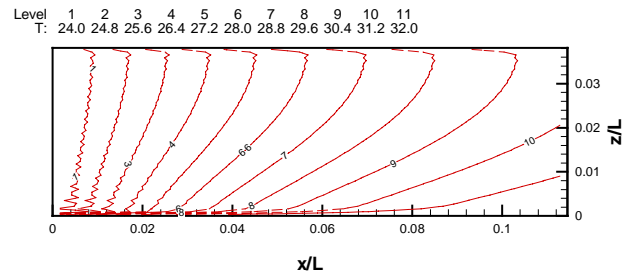
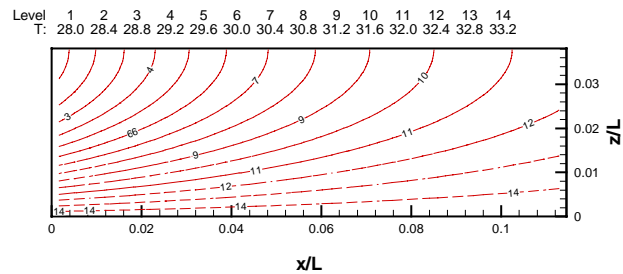


Figure X-23: Temperature field in fluid (a) and in solid (b), $Re_h = 1259$, $Q = 125W$, FVM.

Fig. X-22 (a) reveals that GM at current Reynolds numbers, already exhibits oscillations on the test section inflow. The oscillations originate from thermal boundary conditions (VII.30), which form a step function. Such function is not analytic, therefore the approximation with a series of trigonometric functions produces oscillations. As GM still predicts the temperature field with the same accuracy as FVM in the first half of the simulation domain, the increasing Reynolds number Re_h causes differences between both solutions toward the end of the test section (figs. X-22 and X-23). Nevertheless, the differences for the tested range of Reynolds numbers Re_h are not higher than 5% as shown by Horvat and Catton (2002).

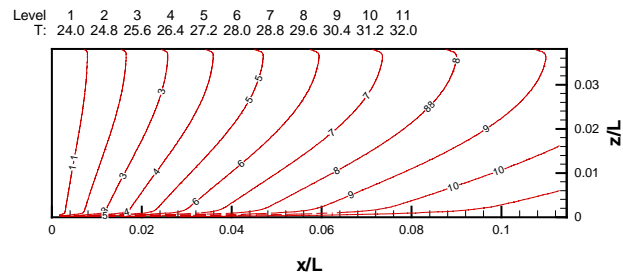


(a)

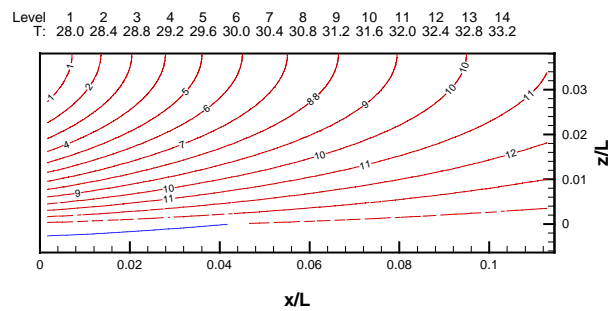


(b)

Figure X-24: Temperature field in fluid (a) and in solid (b), $Re_h = 1593$, $Q = 125W$, GM.



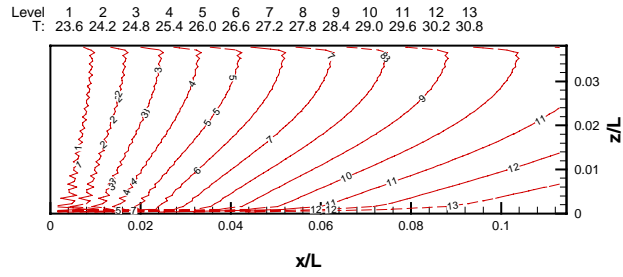
(a)



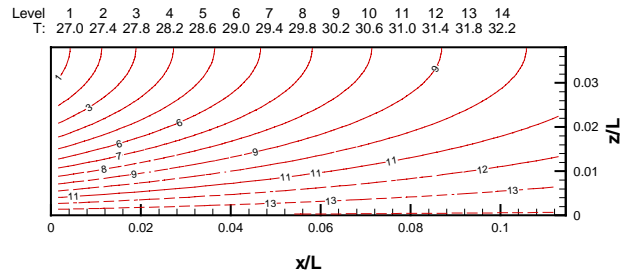
(b)

Figure X-25: Temperature field in fluid (a) and in solid (b), $Re_h = 1598$, $Q = 125W$, FVM.

Comparing the temperatures shown in figs. X-12 to X-27, it can be seen that despite increasing vertical thermal stratification, the flow field as well as the solid structure is getting increasingly isothermal. Namely, with the increasing Reynolds number Re_h the air flow leaves the heat sink at lower exit temperature. Such coolant flow is thermally unsaturated and still capable of heat removal. Nevertheless, as the average temperature decreases, the role of heat conducting base-plate increases. It causes further reduction in the air and structure temperatures at the simulation domain exit.

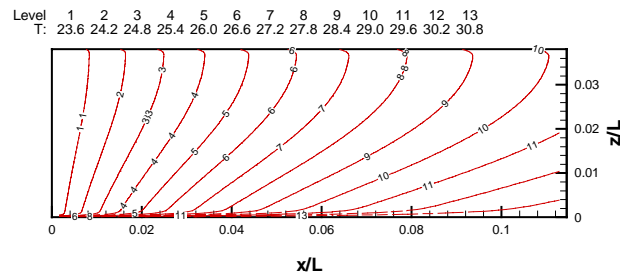


(a)

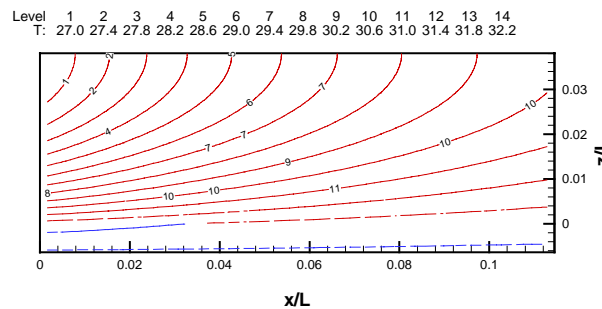


(b)

Figure X-26: Temperature field in fluid (a) and in solid (b), $Re_h = 1861$, $Q = 125W$, GM.



(a)



(b)

Figure X-27: Temperature field in fluid (a) and in solid (b), $Re_h = 1868$, $Q = 125W$, FVM.

X.3 Surface Augmentation and Heat Transfer Enhancement

Based on the models of porous media flow and channel flow described in the chapters V and VII, the comparison of heat transfer process in both cases can be performed. The comparison reveals the role of surface augmentation on heat transfer enhancement. As the calculation method for the channel and heat sink flow, GM is used. Simulations are made for eight different values of Reynolds number Re_h , which is again defined as

$$Re_h = \frac{\overline{\hat{u}} \hat{d}_h}{\hat{\nu}_f}, \quad (\text{X.5})$$

where velocity u is averaged over whole simulation domain. The inflow and bottom thermal boundary conditions are the same for all simulated cases. The initial values and boundary conditions are summarized in tables X-4 and X-5.

Table X-4: Boundary conditions for channel flow calculations.

No.	Re_h	T_{in} [°C]	T_g [°C]
1	164	23.00	30.3
2	256	23.00	30.3
3	379	23.00	30.3
4	553	23.00	30.3

No.	Re_h	T_{in} [°C]	T_g [°C]
5	819	23.00	30.3
6	1167	23.00	30.3
7	1741	23.00	30.3
8	2560	23.00	30.3

Table X-5: Boundary conditions for heat sink flow calculations.

No.	Re_h	T_{in} [°C]	T_g [°C]
1	164	23.00	30.3
2	258	23.00	30.3
3	378	23.00	30.3
4	554	23.00	30.3
5	812	23.00	30.3
6	1189	23.00	30.3
7	1742	23.00	30.3
8	2551	23.00	30.3

Coolant flow velocity profiles in the channel and the heat sink are presented in figs. X-28 and X-29. As the hydraulic diameter of the heat sink ($d_h = 0.005522$) is much smaller than the hydraulic diameter of the channel ($d_h = 0.05718$), the coolant velocity in the channel is much lower than in the heat sink at the same Reynolds number Re_h .

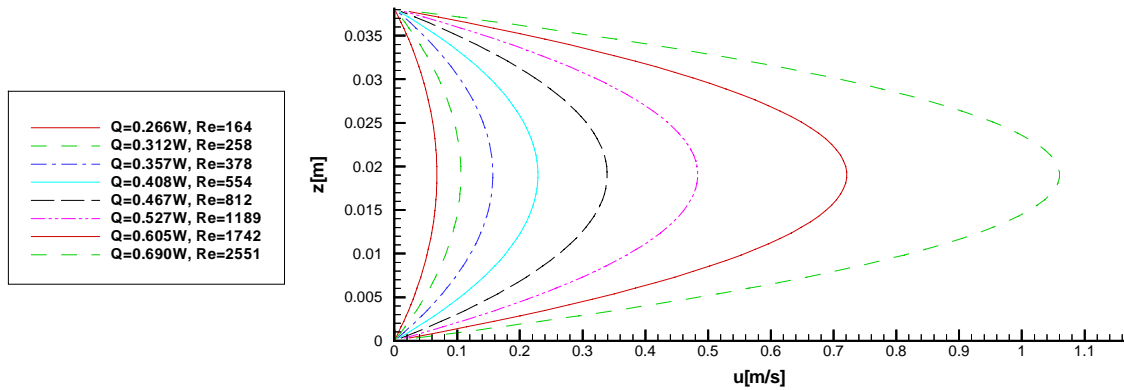


Figure X-28: Fluid velocity cross-section in channel flow.

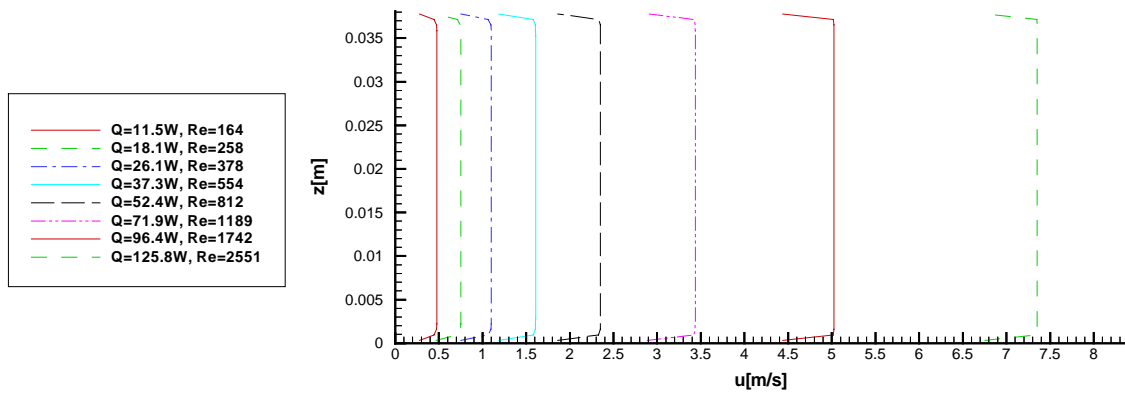


Figure X-29: Fluid velocity in heat sink.

Figs. X-28 and X-29 show that velocity profiles in the channel are parabolic, whereas in the heat sink the velocity profiles are flat with clearly visible boundary layer at upper and lower boundaries. The flat profile in the case of flow through the heat sink comes from additional drag caused by pin-fins. The pin-fins also cause reduction of the flow cross-section that is compensated with higher flow velocities.

Fig. X-30 presents temperature field in the channel flow at the Reynolds number $Re_h = 379$, whereas fig. X-31 shows the temperature field in the heat sink flow at the Reynolds number $Re_h = 378$. The temperature fields calculated at other examined Reynolds numbers (see tables X-4 and X-5) are summarized in the appendix D.

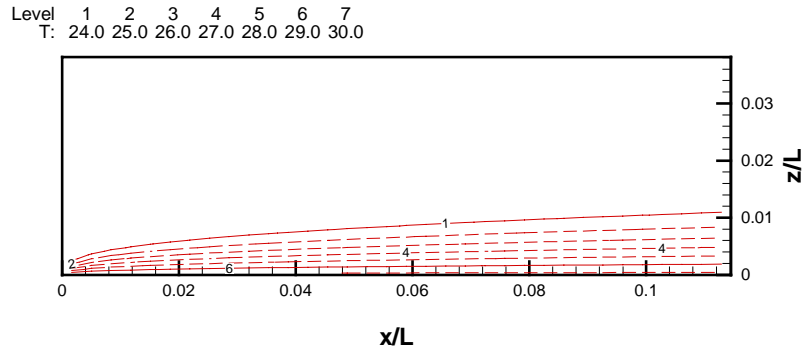


Figure X-30: Temperature field at $Re_h = 379$ in channel flow; $Q = 0.358W$

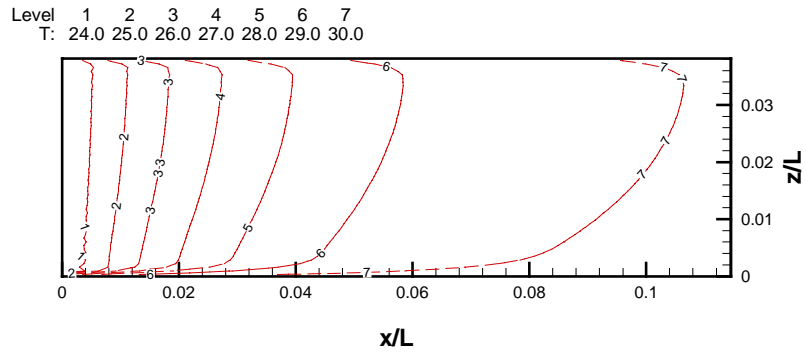


Figure X-31: Temperature field at $Re_h = 378$ in channel flow; $Q = 26.1W$

The presence of heat conducting internal structure causes essential difference between the compared temperature fields. As is evident in fig. X-30, the channel flow shows only a thermal boundary layer. In the case of flow through the heat sink, the heat is easily transported in the vertical direction by thermal conduction in the pin-fins. Such fast vertical transport causes the horizontal stratification of coolant flow, which modestly changes orientation at higher Reynolds numbers. Due to enhanced vertical heat transport, the thermal saturation of the flow through the heat sink is much higher than in the channel flow.

Based on these phenomenological observations some general conclusions can be drawn. The diagrams in figs. X-32, X-33 and X-34 show the whole-section heat flow Q (X.3), the Nusselt number Nu (X.2) and the thermal effectiveness Q/W as a function of Reynolds number Re_h (X.5). The comparisons are made for channel flow (marked with “Channel”) and flow through the heat sink structure (marked with “Structure”).

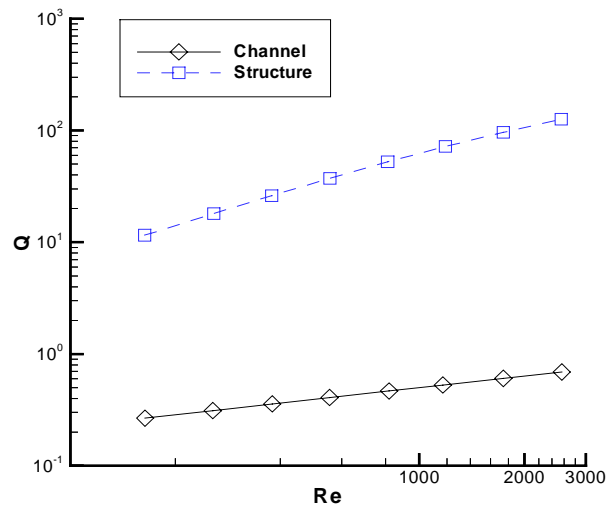


Figure X-32: Heat flow Q , $T_{in} = 23^\circ\text{C}$ and $T_g = 30.3^\circ\text{C}$.

Fig. X-32 reveals that the flow through the heat sink is capable of transferring much more thermal energy than the channel flow at the same Reynolds number Re_h . At the Reynolds number $Re_h \approx 164$, the heat sink transfers 43.4 times more thermal energy than the channel. With increasing Reynolds this ratio increases to 182.3 at the Reynolds number $Re_h \approx 2555$.

A diagram of the whole-section Nusselt number Nu (X.2) in fig. X-33 shows that values of the Nusselt number are higher in the case of the heat sink, although the hydraulic diameter d_h is much smaller.

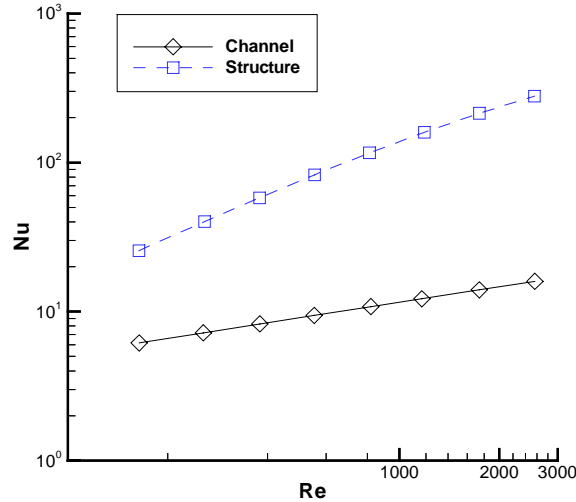


Figure X-33: Nusselt number Nu , $T_{in} = 23^{\circ}\text{C}$ and $T_g = 30.3^{\circ}\text{C}$.

Fig. X-33 also discloses that with the increasing Reynolds number Re_h , the heat transfer enhancement further increases. Namely, for the Reynolds number $Re_h \approx 164$ the Nusselt number of the heat sink is 4.2 times higher than in the channel flow, whereas for the Reynolds number $Re_h \approx 2555$ this Nusselt number ratio increases to 17.5.

Fig. X-34 shows the thermal effectiveness, which is defined as the ratio between removed heat flow Q (X.3) and mechanical power W (X.4) needed for force convection cooling. Although, the heat flow Q is more than 40 times higher in the case of the heat sink, the mechanical power expanded to overcome pin-fins drag is even much more substantial. Therefore, the thermal effectiveness Q/W of the channel is 3 orders of magnitude higher than for the examined heat sink.

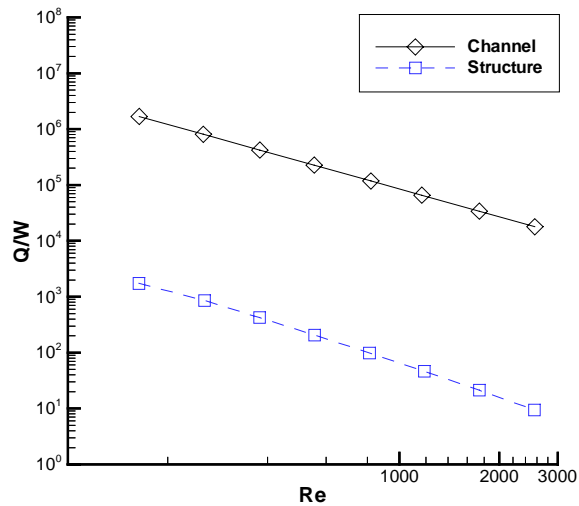


Figure X-34: Thermal effectiveness Q/W , $T_{in} = 23^{\circ}\text{C}$ and $T_g = 30.3^{\circ}\text{C}$.

Fig. X-34 illustrates the fact that a heat transfer enhancement requires a surface augmentation, which inevitable increases drag and therefore consumption of mechanical power W . Furthermore, the need for a mechanical power increases faster than the cooling power Q . Therefore, the insertion of structures in the coolant flow cannot increase the thermal effectiveness Q/W , although it brings significant heat transfer enhancement.

Often one wants to minimize the volume for a given amount of heat removal. Under circumstances where a criteria is reduced volume or weight, the heat sink with pins will be an improvement over the behavior of a flat surfaced channel.

XI. Conclusions

The thesis represents a contribution to conjugate heat transfer modeling. In this work the Volume Averaging Technique (VAT) was tested and further applied to a simulation of air-flow through aluminum (Al) chip heat sink. The constructed computational algorithm enables prediction of cooling capabilities for the selected geometry. It also offers possibility for geometry improvements to achieve higher thermal effectiveness.

In frame of the thesis work, a general model of homogeneous porous media flow was developed using the VAT basic rules. To understand a construction of the calculation model, the volume averaging procedure was described in details. As the flow variables are averaged over the representative elementary volume (REV), local momentum and thermal interactions between phases have to be replaced with additional closure models.

The same averaging procedure was used to develop a specific model for the channel flow and the flow through heat conducting structure of the heat sink. To close the system of transport equations, reliable data for intraphase transfer coefficients were found in Lauder and Massey (1978), Žukauskas and Ulinskas (1985), and Kays and London (1998). Using VAT, the computational algorithm is fast running, but still able to present a detailed picture of temperature fields in the air-flow as well as in the solid structure of the

heat sink. These characteristics enable the use of the developed algorithm for future optimization calculations of heat exchanger morphologies.

The geometry of the simulation domain and the boundary conditions followed the geometry of the experimental test section used in the Morrin-Martinelli-Gier Memorial Heat Transfer Laboratory at University of California, Los Angeles. The calculations were performed at three different heating powers: $Q = 50\text{W}$, 125W and 220W and eight different pressure drops. The imposed pressure drop achieved coolant flow of Reynolds number Re_h from 159 to 1904. As a calculation technique, a semi-analytical Galerkin Method (GM) and Finite Volume Method (FVM) were selected. Although GM is a well established technique, it hasn't been used for conjugate heat transfer problems in heat exchanger geometries.

The calculated whole-section drag coefficient C_d , Nusselt number Nu and thermal effectiveness Q/W were compared with experimental data (Rizzi et al., 2001) to verify the computational model and validate numerical code. The comparison shows a good agreement between GM and FVM results although different thermal boundary conditions at the bottom were used. The experimental data exhibit up to 10% difference through the whole computational range of Reynolds numbers Re_h , which is believed to be a consequence of systematic modeling or experimental error.

The detailed temperature fields in the coolant flow as well as in the heat conducting structure were also calculated. The calculations revealed that, when the temperature field develops with increasing Reynolds number Re_h , the flow thermal saturation decreases. The air flow leaves the heat sink at lower exit temperature, still capable of heat removal. This effect reduces the thermal effectiveness Q/W of the heat sink. It is also seen that increasing Reynolds number Re_h changes the temperature field from vertical to more horizontal stratification. As the plotted three-dimensional temperature fields reveal the local heat transfer conditions, they enable corrections and optimization of the heat sink geometry.

The optimization of the heat sink geometry will be performed in the future, when more interphase transfer coefficients are available for different surface morphologies. In order to obtain the local distributions of interphase transfer coefficients, Direct Numerical Simulations (DNS) or Large-Eddy Simulations (LES) of the flow through the heat exchanger REV will be performed.

To determine the role of surface augmentation on heat transfer enhancement, the channel flow was compared with the flow through the heat sink for the same Reynolds numbers. It is obvious that the heat sink is capable of transferring much more thermal energy than the channel. Furthermore, the Nusselt number is also much higher for the heat sink than for the channel. On the other hand, the calculations reveal that the thermal effectiveness of the heat sink is much lower than that of the channel. Namely, the

expenditure of mechanical power to move the fluid through heat sink structure is higher than the heat transfer enhancement due to the surface augmentation. Therefore, the increase in heat transferring surface do enhance the heat flow and enables more compact designs of heat exchangers, but nevertheless, due to the lower thermal effectiveness, the economics heat transfer process worsen.

The present results demonstrate that the selected VAT approach is appropriate for heat exchanger calculations where thermal conductivity of the solid structure has to be taken into account. The performed calculations also verify that the developed numerical code yields sufficiently accurate results to be applicable also in future optimization calculations for heat exchanger morphologies.

APPENDIX A : Heat Sink Velocity and Temperature Fields, 50W

A.1 Velocity Fields

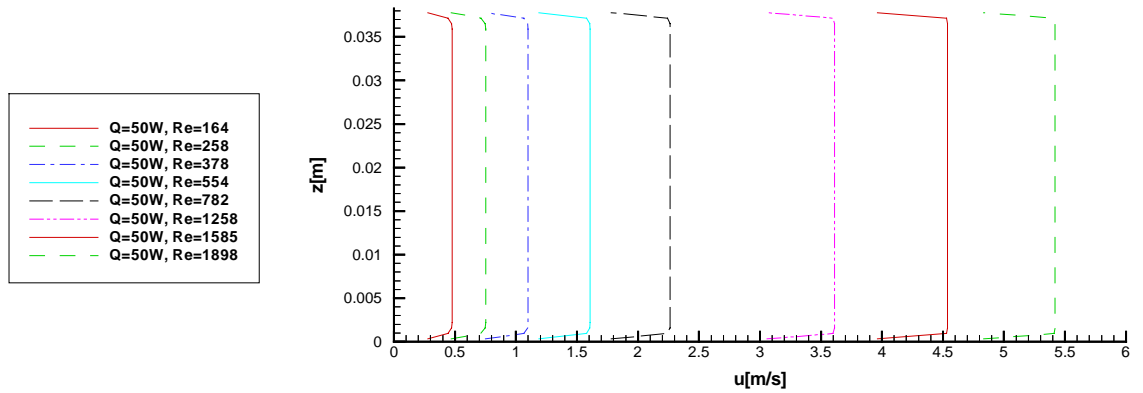


Figure A-1: Fluid velocity cross-section, $Q = 50$ W, GM.

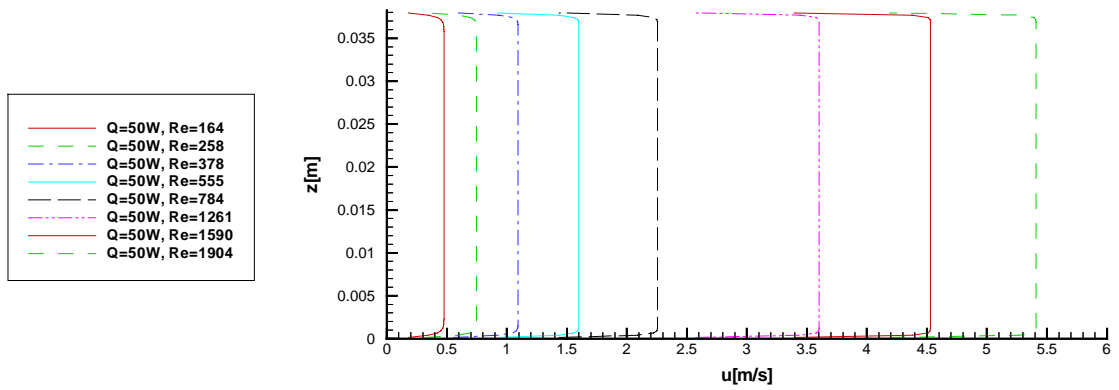


Figure A-2: Fluid velocity cross-section, $Q = 50$ W, FVM.

A.2 Temperature Fields

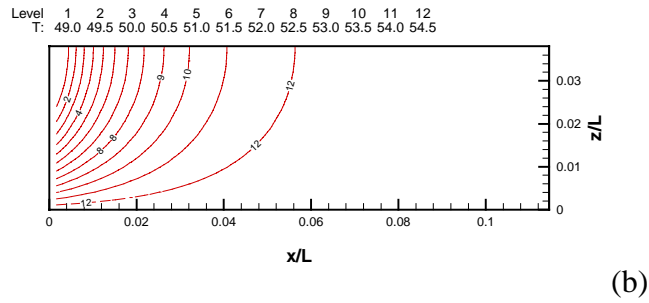
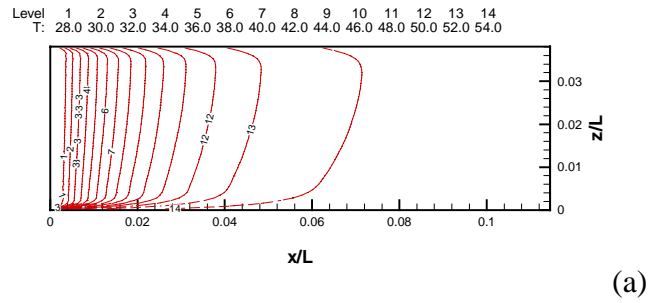


Figure A-3: Temperature in fluid (a) and in solid (b), $Q = 50W$, $Re_h = 164$, GM.

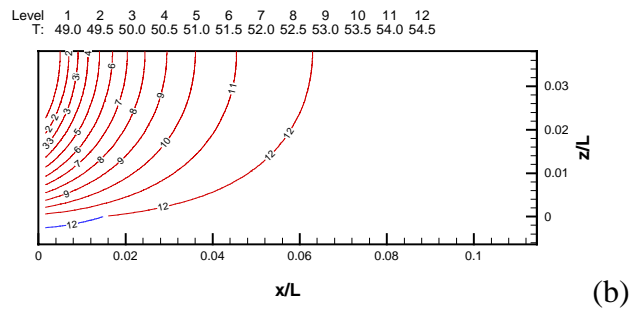
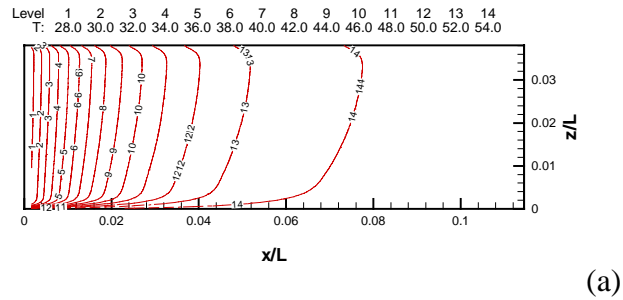
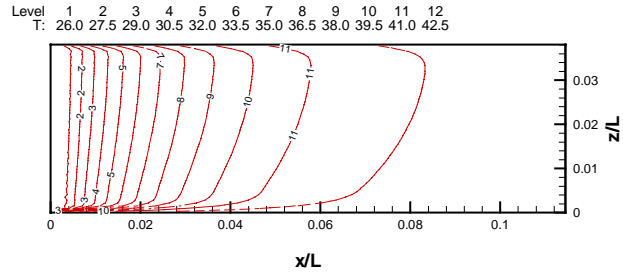
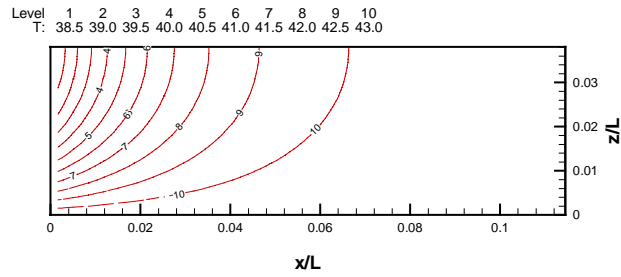


Figure A-4: Temperature in fluid (a) and in solid (b), $Q = 50W$, $Re_h = 164$, FVM.

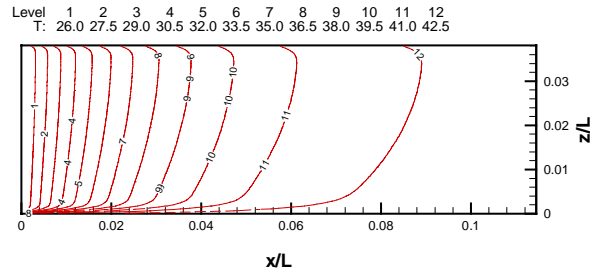


(a)

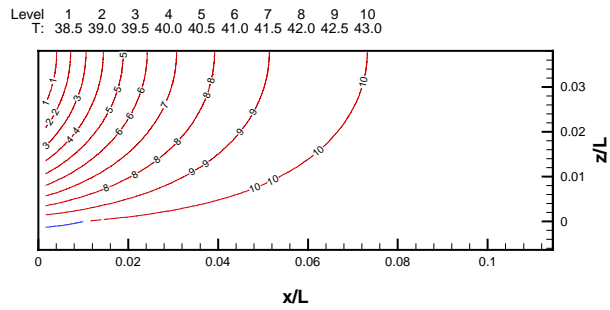


(b)

Figure A-5: Temperature in fluid (a) and in solid (b), $Q = 50W$, $Re_h = 258$, GM.

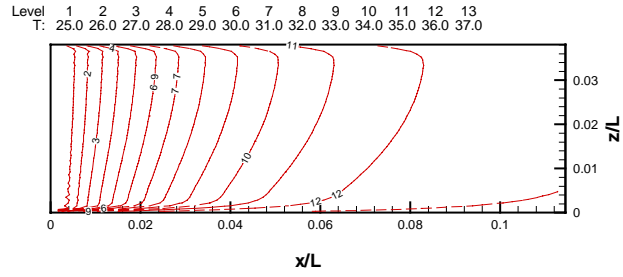


(a)

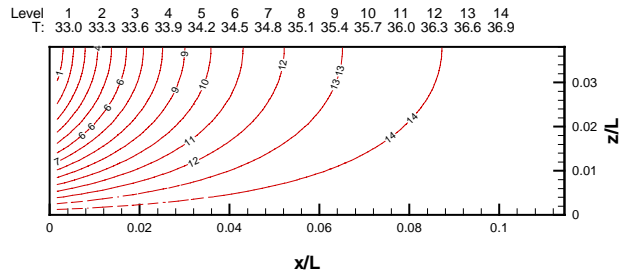


(b)

Figure A-6: Temperature in fluid (a) and in solid (b), $Q = 50W$, $Re_h = 258$, FVM.

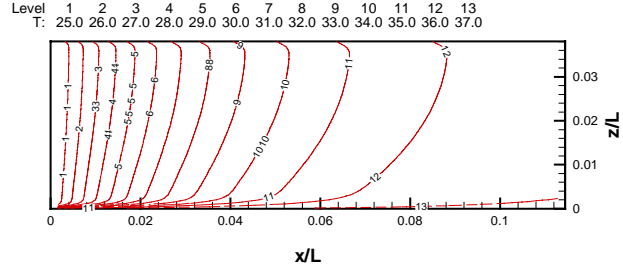


(a)

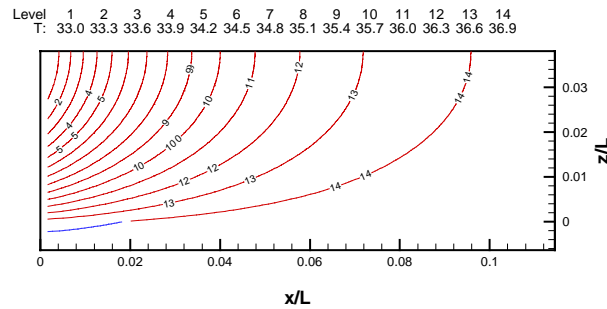


(b)

Figure A-7: Temperature in fluid (a) and in solid (b), $Q = 50\text{W}$, $Re_h = 378$, GM.

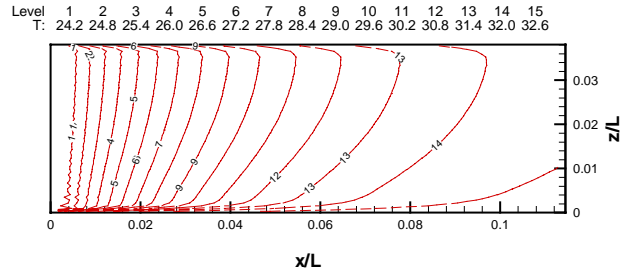


(a)

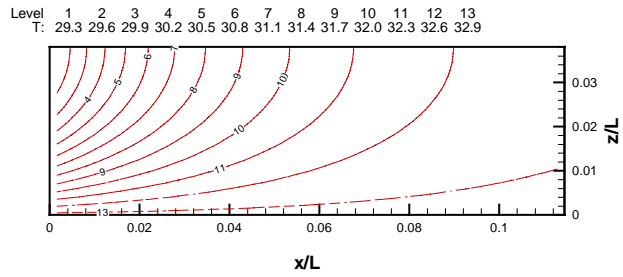


(b)

Figure A-8: Temperature in fluid (a) and in solid (b), $Q = 50\text{W}$, $Re_h = 379$, FVM.

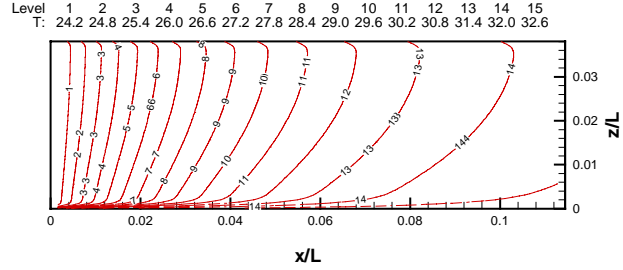


(a)

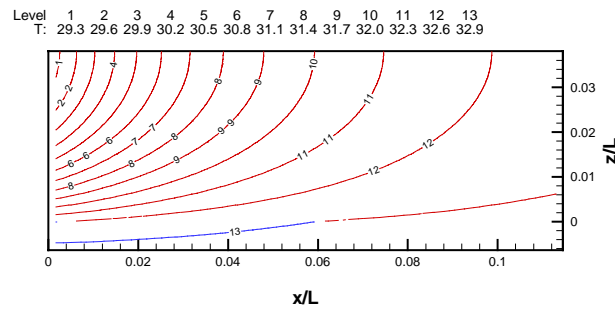


(b)

Figure A-9: Temperature in fluid (a) and in solid (b), $Q = 50W$, $Re_h = 554$, GM.

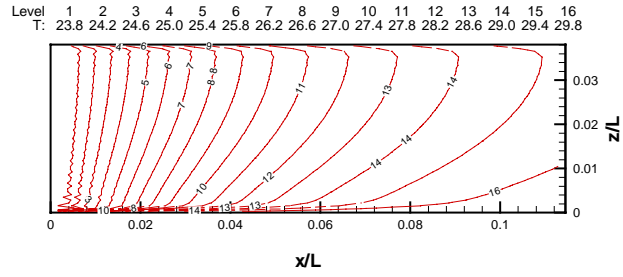


(a)

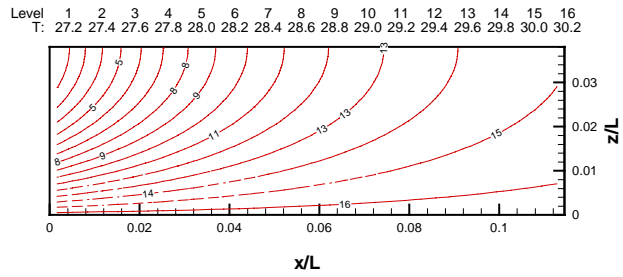


(b)

Figure A-10: Temperature in fluid (a) and in solid (b), $Q = 50W$, $Re_h = 555$, FVM.

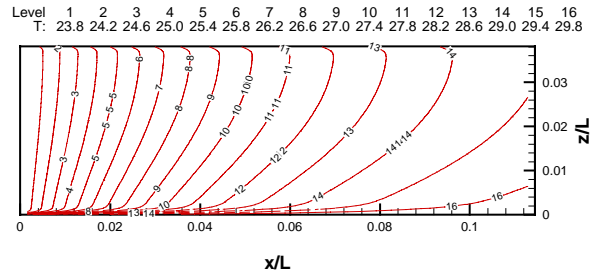


(a)

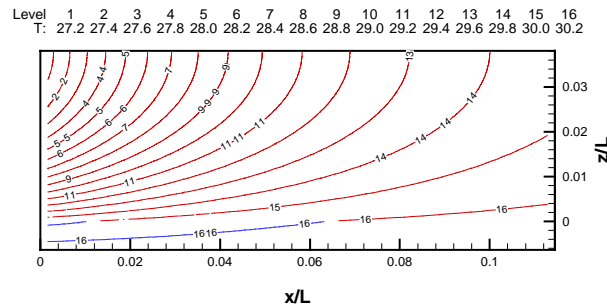


(b)

Figure A-11: Temperature in fluid (a) and in solid (b), $Q = 50\text{W}$, $Re_h = 782$, GM.

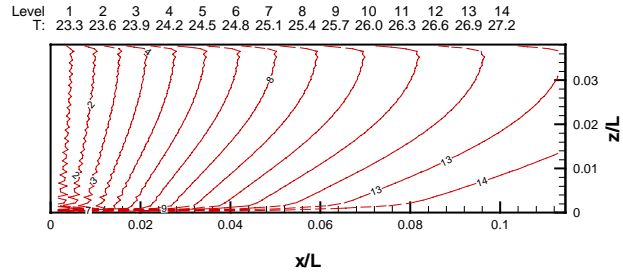


(a)

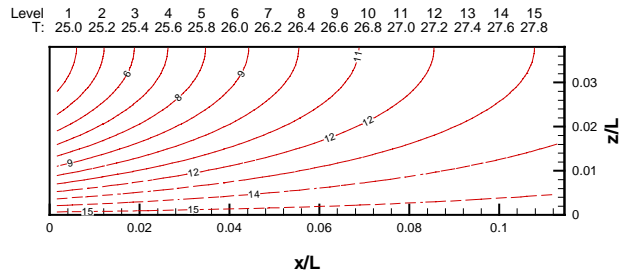


(b)

Figure A-12: Temperature in fluid (a) and in solid (b), $Q = 50\text{W}$, $Re_h = 784$, FVM.

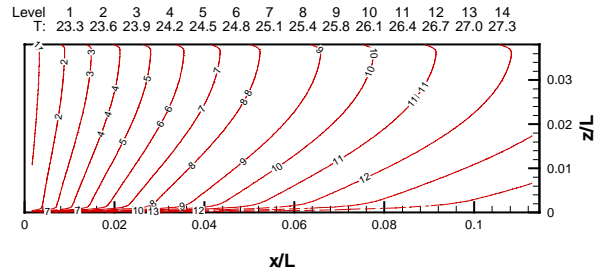


(a)

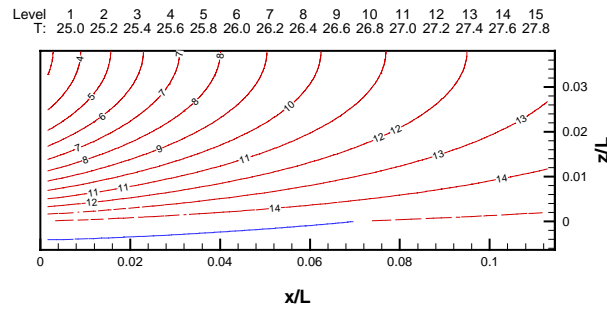


(b)

Figure A-13: Temperature in fluid (a) and in solid (b), $Q = 50\text{W}$, $Re_h = 1258$, GM.

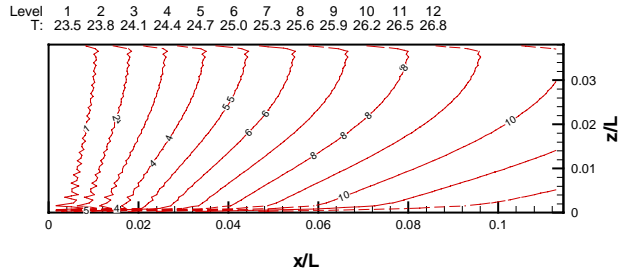


(a)

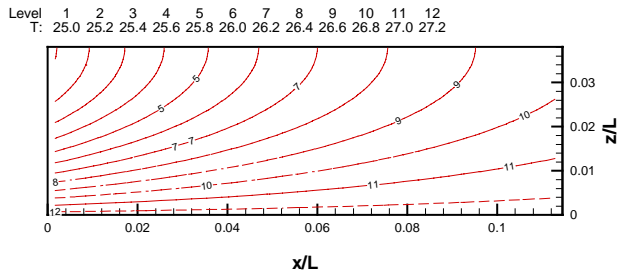


(b)

Figure A-14: Temperature in fluid (a) and in solid (b), $Q = 50\text{W}$, $Re_h = 1261$, FVM.

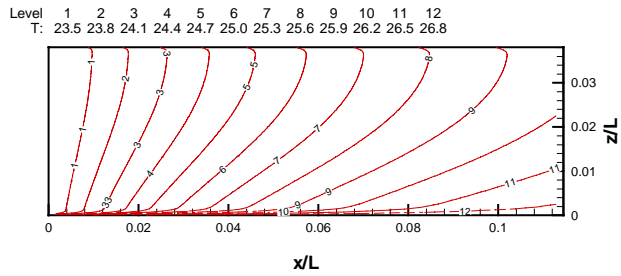


(a)

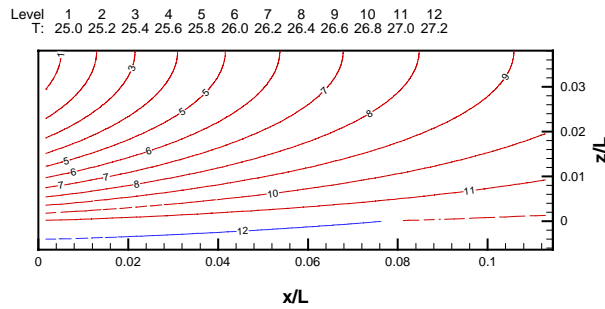


(b)

Figure A-15: Temperature in fluid (a) and in solid (b), $Q = 50\text{W}$, $Re_h = 1585$, GM.

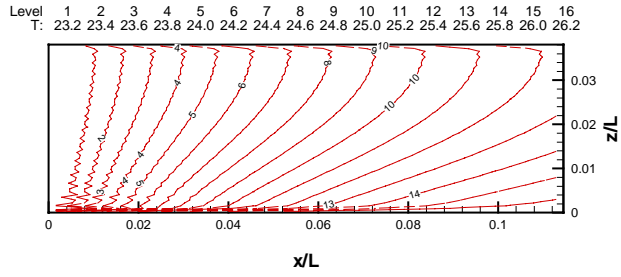


(a)

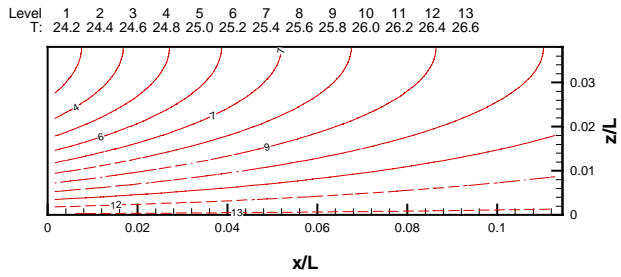


(b)

Figure A-16: Temperature in fluid (a) and in solid (b), $Q = 50\text{W}$, $Re_h = 1590$, FVM.

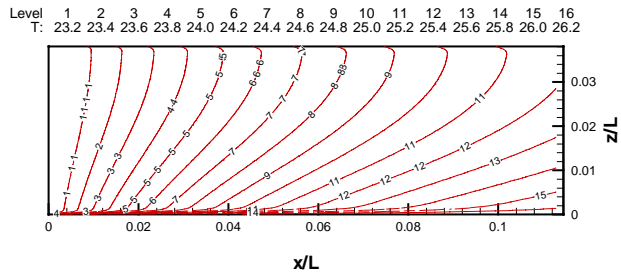


(a)

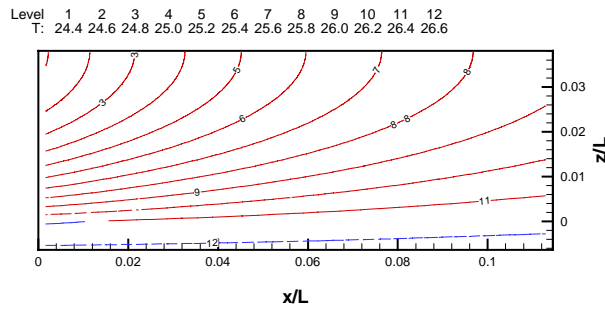


(b)

Figure A-17: Temperature in fluid (a) and in solid (b), $Q = 50\text{W}$, $Re_h = 1898$, GM.



(a)



(b)

Figure A-18: Temperature in fluid (a) and in solid (b), $Q = 50\text{W}$, $Re_h = 1904$, FVM.

APPENDIX B : Heat Sink Velocity and Temperature Fields, 125W

B.1 Velocity Fields

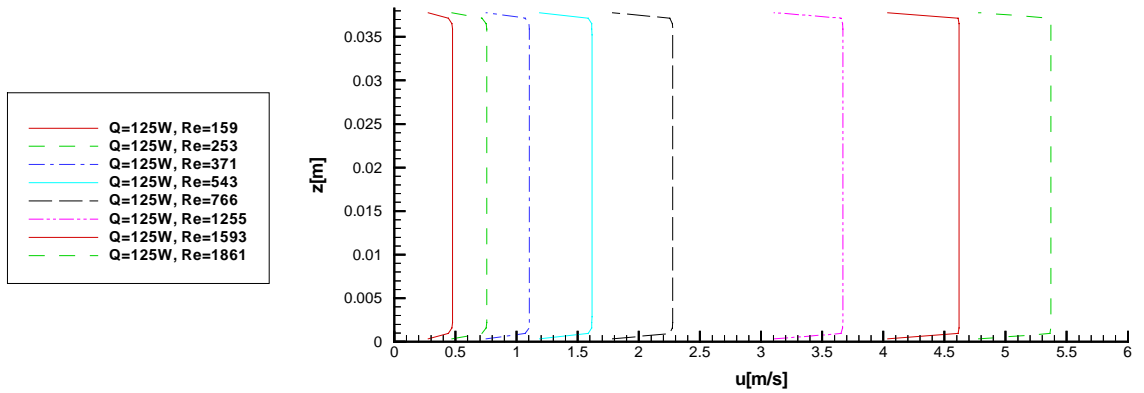


Figure B-1: Fluid velocity cross-section, $Q = 125$ W, GM.

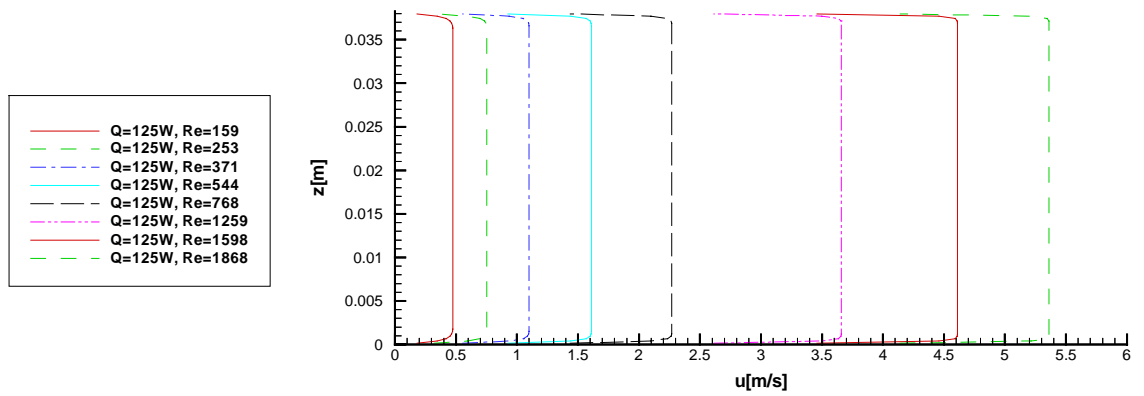


Figure B-2: Fluid velocity cross-section, $Q = 125$ W, FVM.

B.2 Temperature Fields

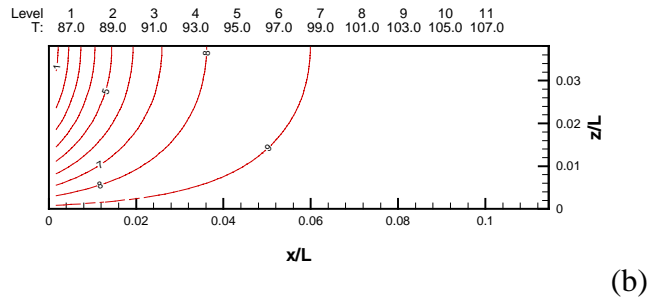
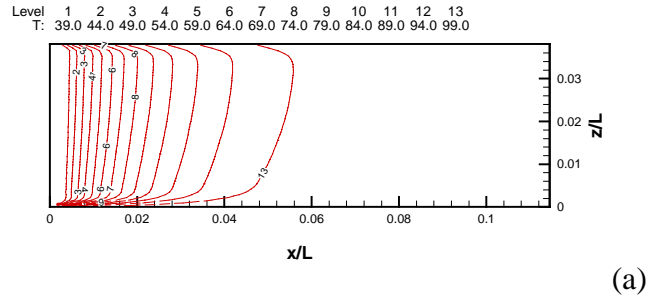


Figure B-3: Temperature in fluid (a) and in solid (b), $Q = 125\text{W}$, $Re_h = 159$, GM.

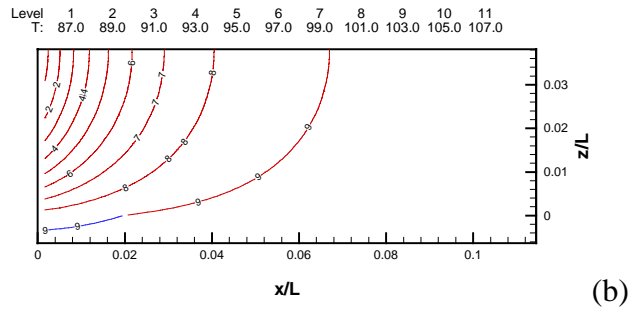
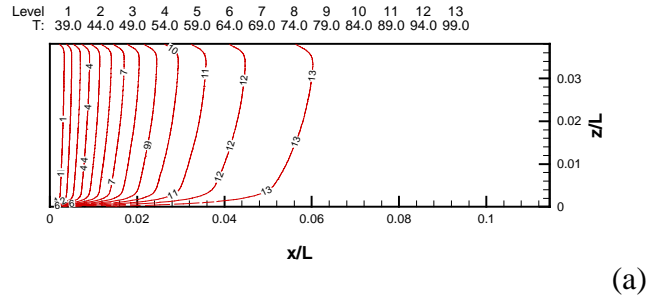
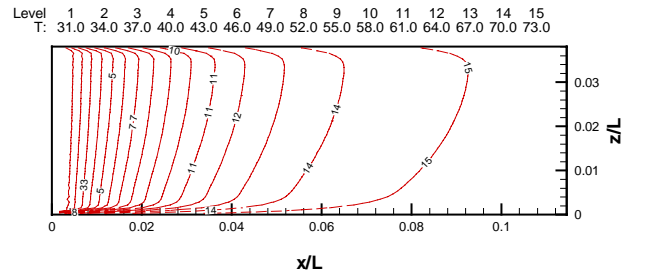
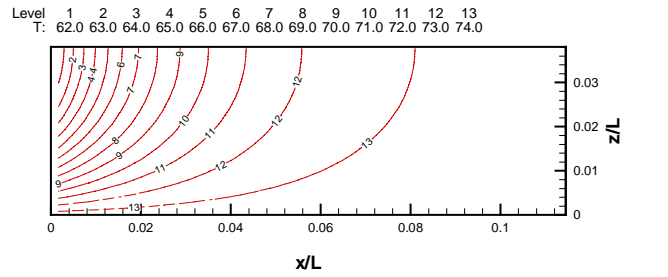


Figure B-4: Temperature in fluid (a) and in solid (b), $Q = 125\text{W}$, $Re_h = 159$, FVM.

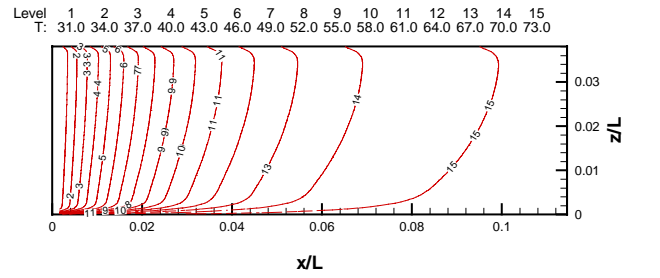


(a)

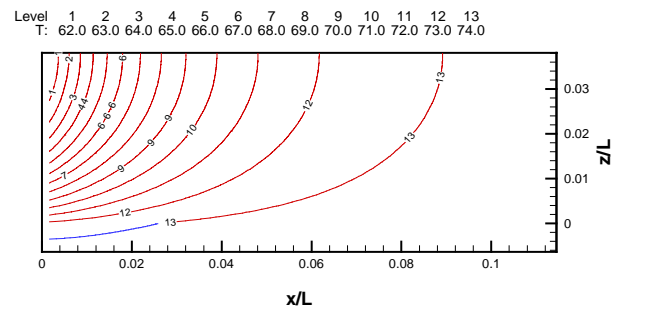


(b)

Figure B-5: Temperature in fluid (a) and in solid (b), $Q = 125\text{W}$, $Re_h = 253$, GM.



(a)



(b)

Figure B-6: Temperature in fluid (a) and in solid (b), $Q = 125\text{W}$, $Re_h = 253$, FVM.

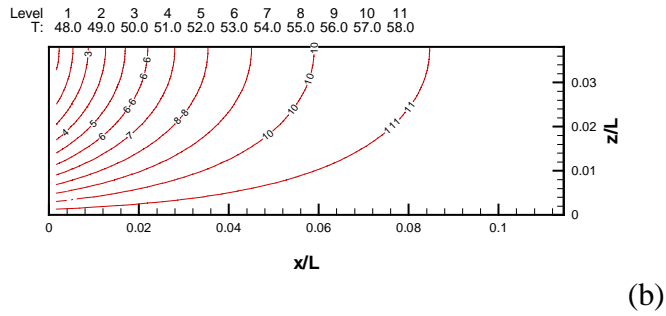
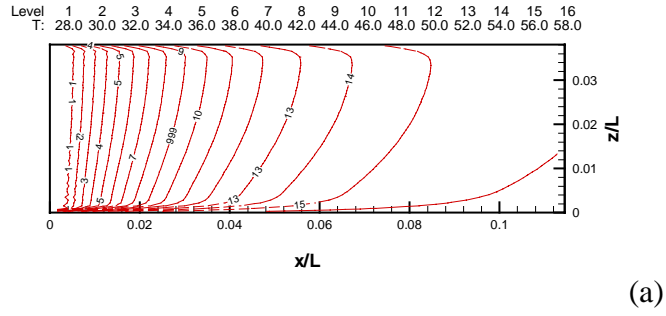


Figure B-7: Temperature in fluid (a) and in solid (b), $Q = 125\text{W}$, $Re_h = 371$, GM.

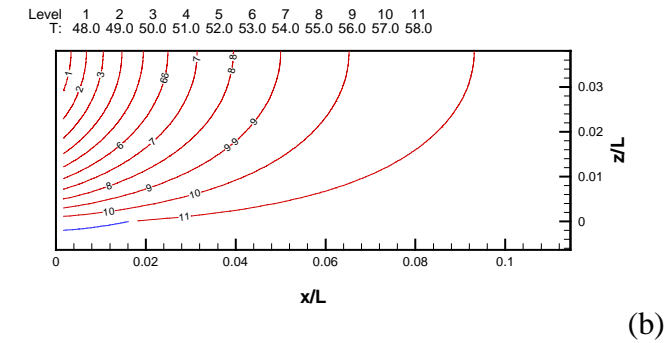
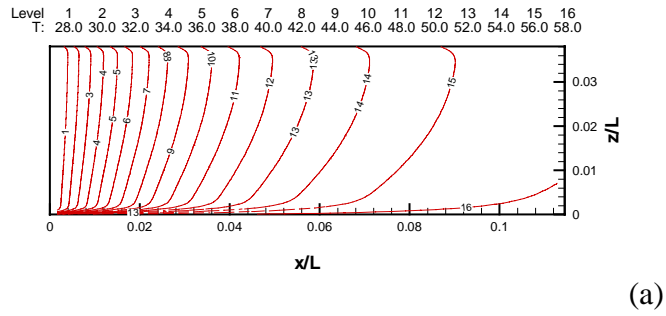


Figure B-8: Temperature in fluid (a) and in solid (b), $Q = 125\text{W}$, $Re_h = 371$, FVM.

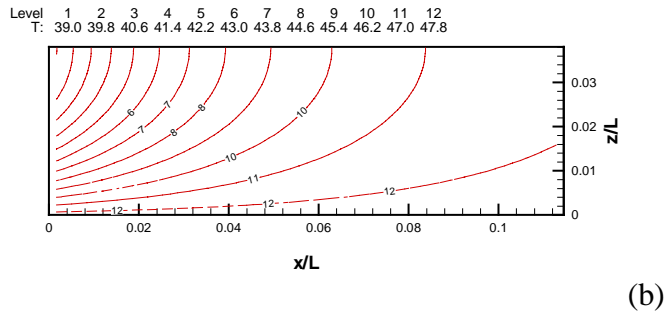
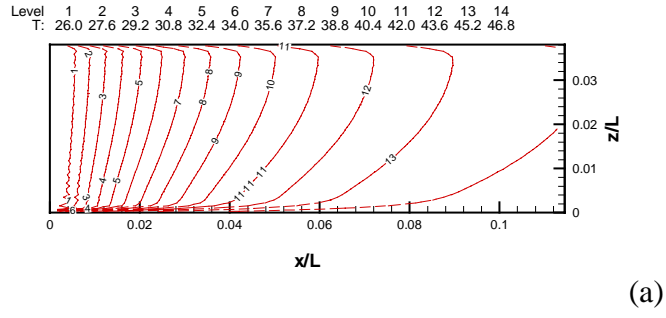


Figure B-9: Temperature in fluid (a) and in solid (b), $Q = 125\text{W}$, $Re_h = 543$, GM.

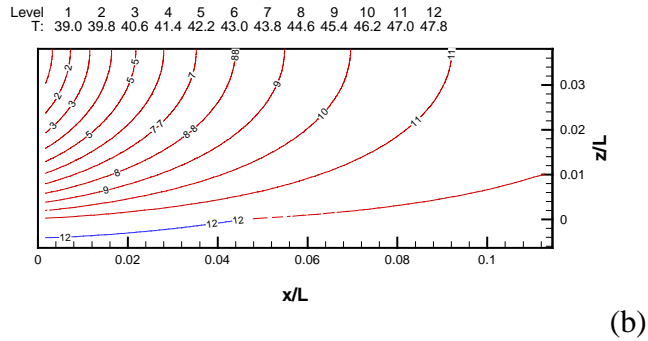
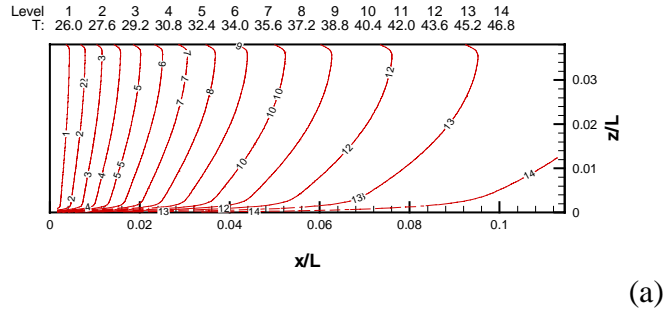


Figure B-10: Temperature in fluid (a) and in solid (b), $Q = 125\text{W}$, $Re_h = 544$, FVM.

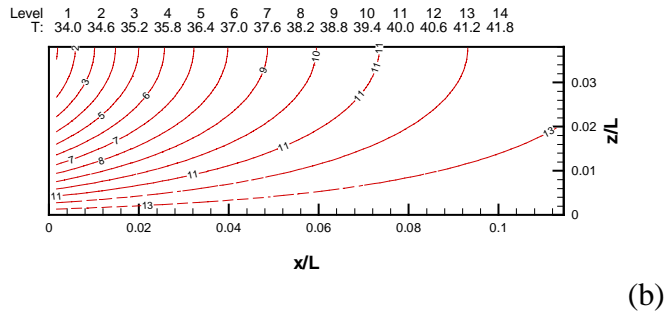
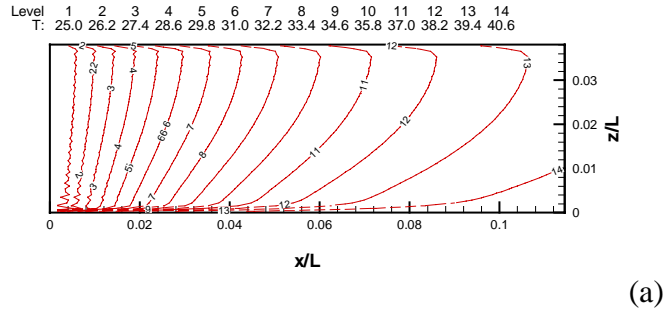


Figure B-11: Temperature in fluid (a) and in solid (b), $Q = 125W$, $Re_h = 766$, GM.

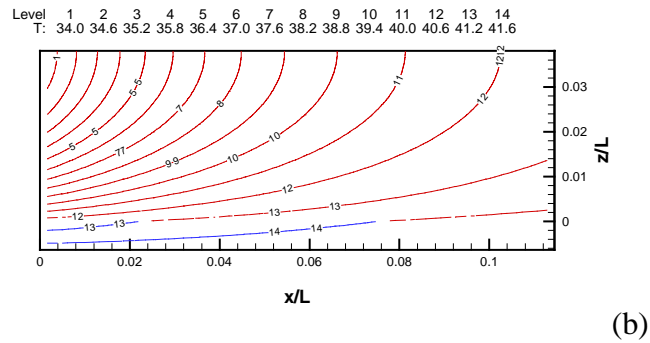
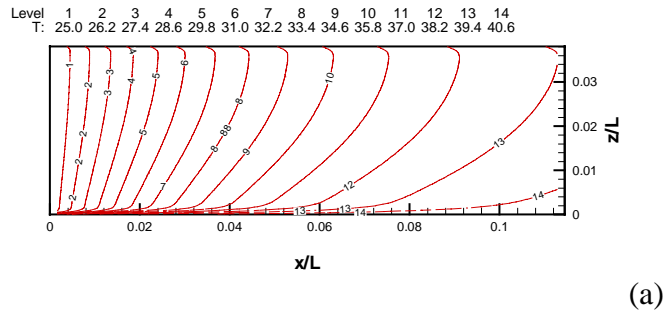


Figure B-12: Temperature in fluid (a) and in solid (b), $Q = 125W$, $Re_h = 768$, FVM.

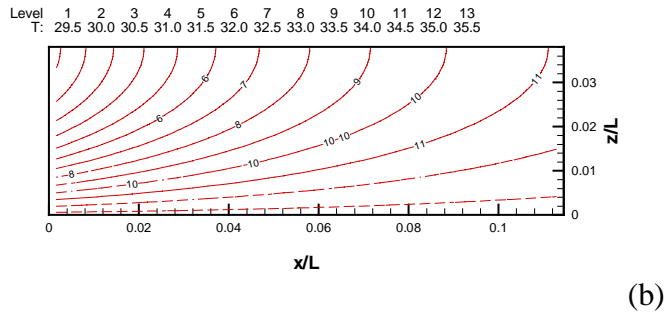
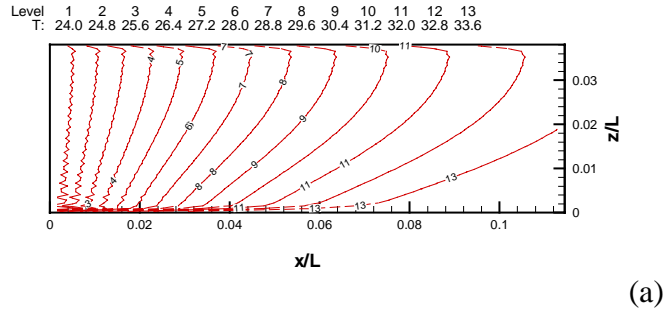


Figure B-13: Temperature in fluid (a) and in solid (b), $Q = 125\text{W}$, $Re_h = 1255$, GM.

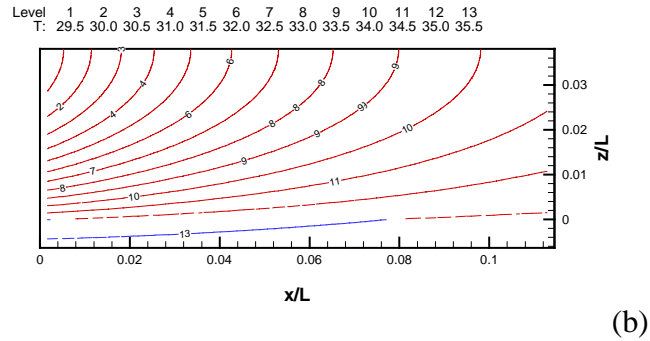
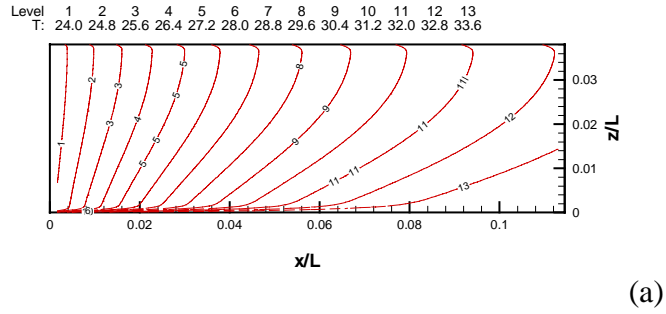


Figure B-14: Temperature in fluid (a) and in solid (b), $Q = 125\text{W}$, $Re_h = 1259$, FVM.

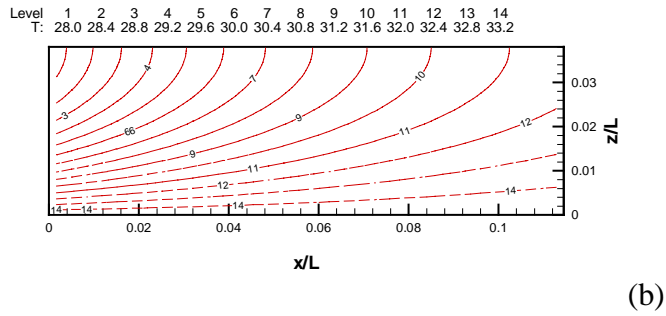
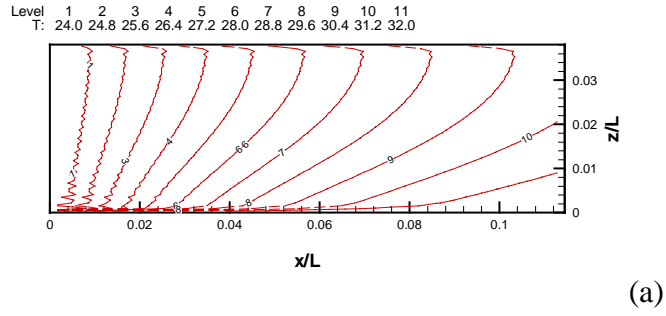


Figure B-15: Temperature in fluid (a) and in solid (b), $Q = 125\text{W}$, $Re_h = 1593$, GM.

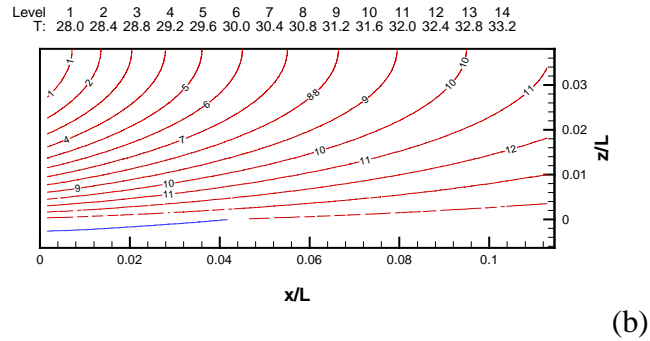
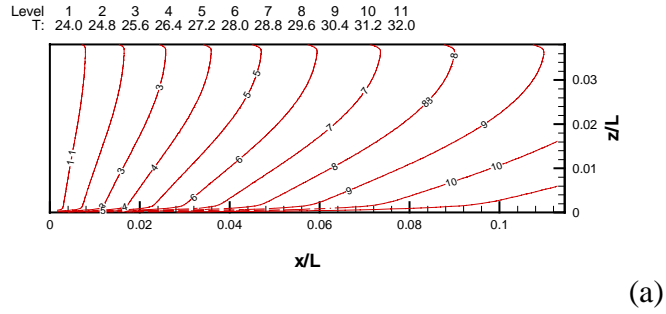
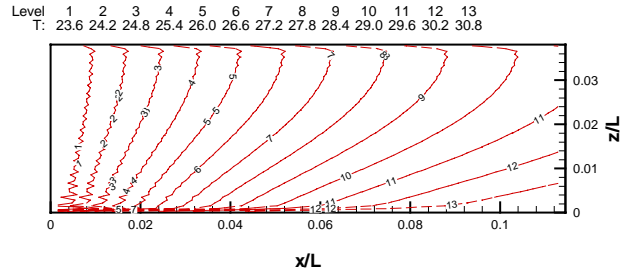
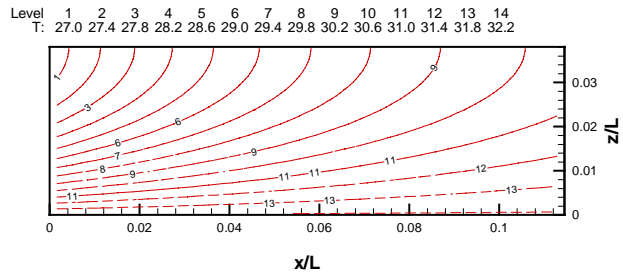


Figure B-16: Temperature in fluid (a) and in solid (b), $Q = 125\text{W}$, $Re_h = 1598$, FVM.

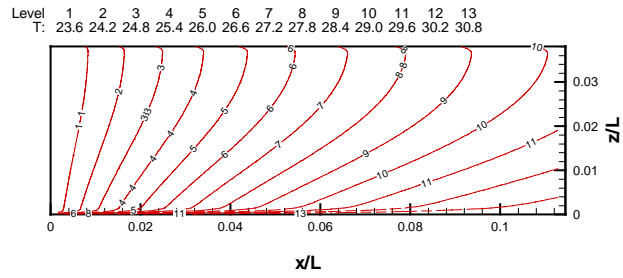


(a)

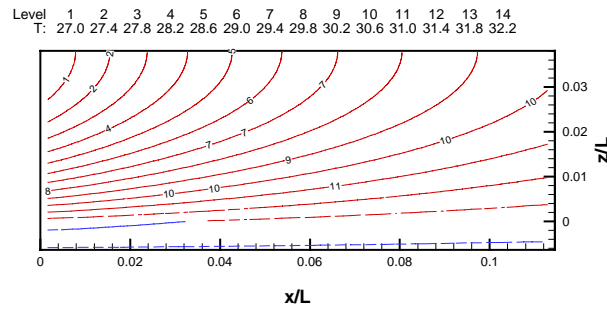


(b)

Figure B-17: Temperature in fluid (a) and in solid (b), $Q = 125\text{W}$, $Re_h = 1861$, GM.



(a)



(b)

Figure B-18: Temperature in fluid (a) and in solid (b), $Q = 125\text{W}$, $Re_h = 1868$, FVM.

APPENDIX C: Heat Sink Velocity and Temperature Fields, 220W

C.1 Velocity Fields

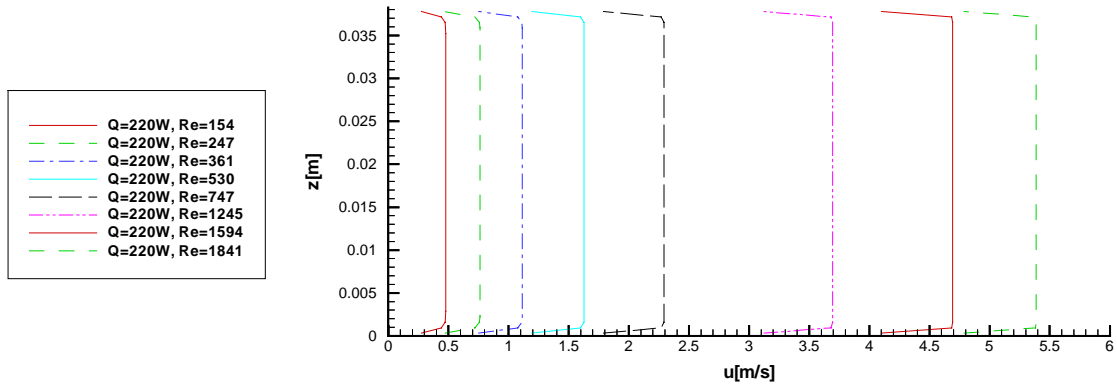


Figure C-1: Fluid velocity cross-section, $Q = 220\text{W}$, GM.

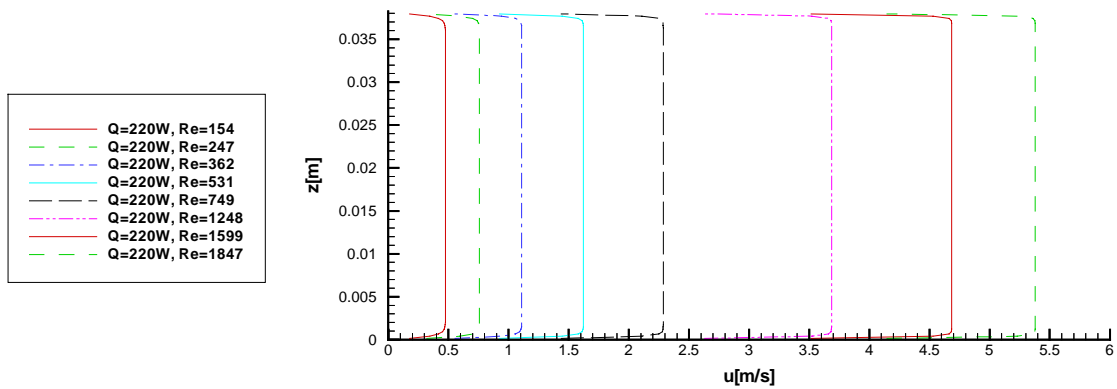
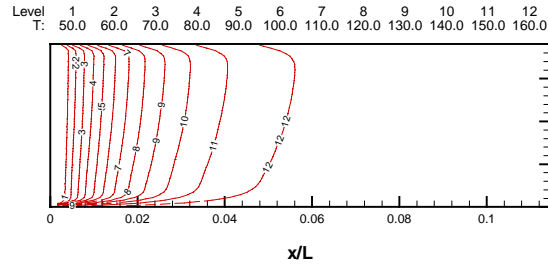
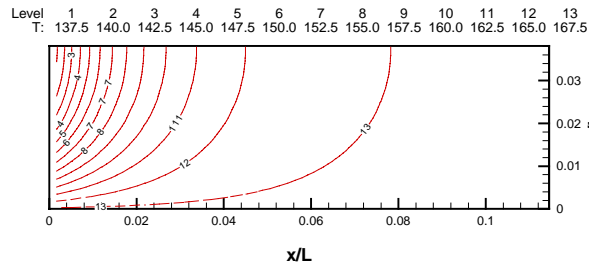


Figure C-2: Fluid velocity cross-section, $Q = 220\text{W}$, FVM.

C.2 Temperature Fields

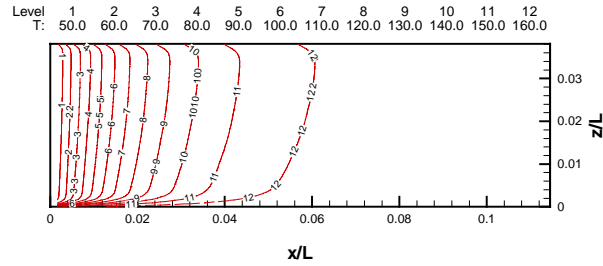


(a)

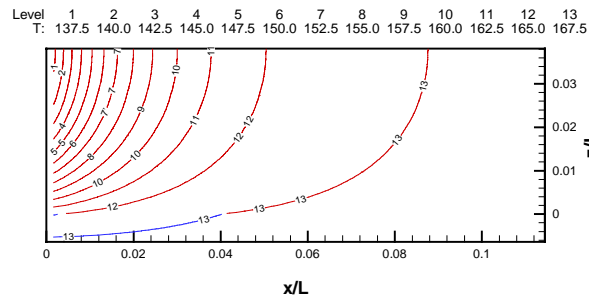


(b)

Figure C-3: Temperature in fluid (a) and in solid (b), $Q = 220\text{W}$, $Re_h = 154$, GM.

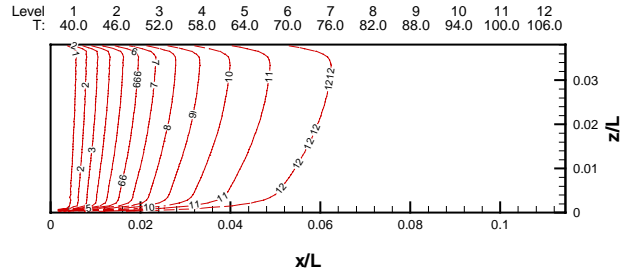


(a)

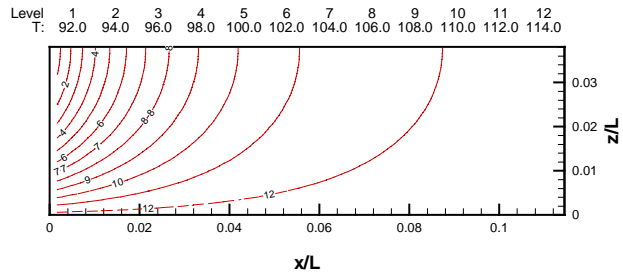


(b)

Figure C-4: Temperature in fluid (a) and in solid (b), $Q = 220\text{W}$, $Re_h = 154$, FVM.

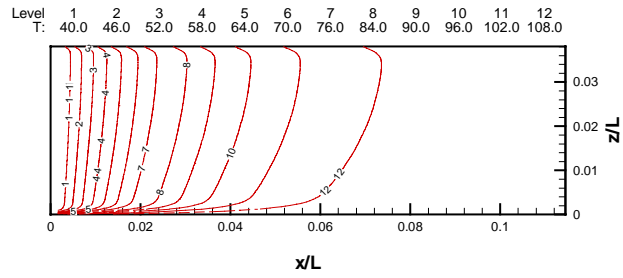


(a)

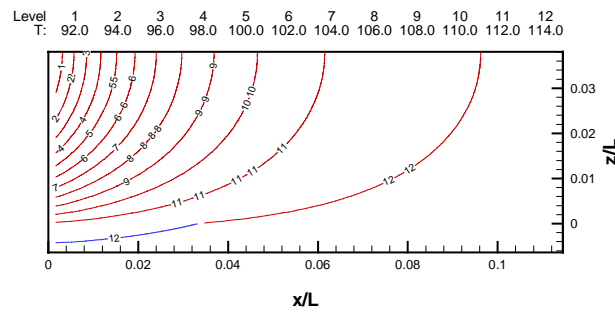


(b)

Figure C-5: Temperature in fluid (a) and in solid (b), $Q = 220\text{W}$, $Re_h = 247$, GM.

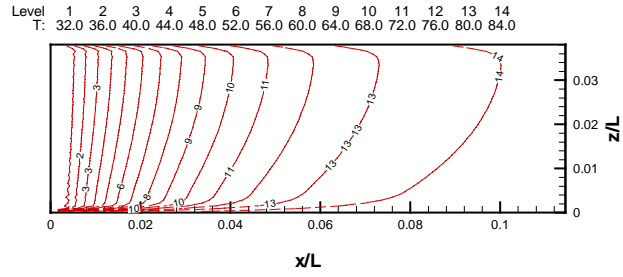


(a)

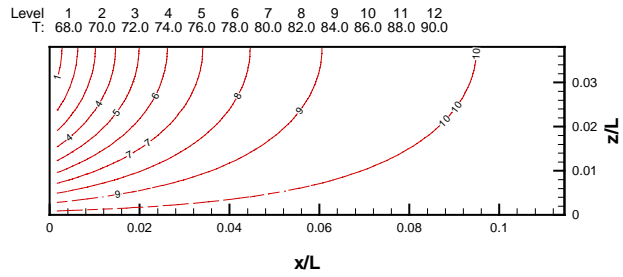


(b)

Figure C-6: Temperature in fluid (a) and in solid (b), $Q = 220\text{W}$, $Re_h = 247$, FVM.

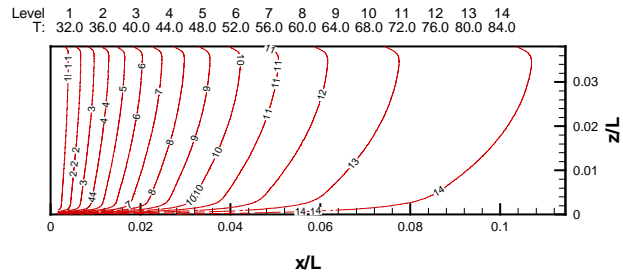


(a)

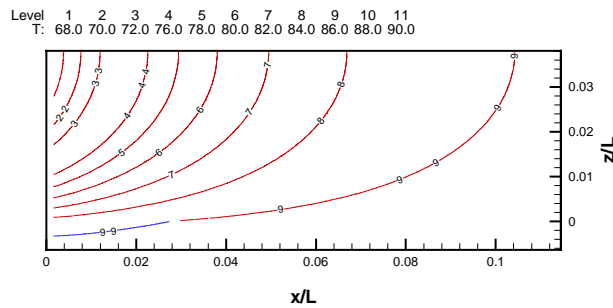


(b)

Figure C-7: Temperature in fluid (a) and in solid (b), $Q = 220\text{W}$, $Re_h = 361$, GM.

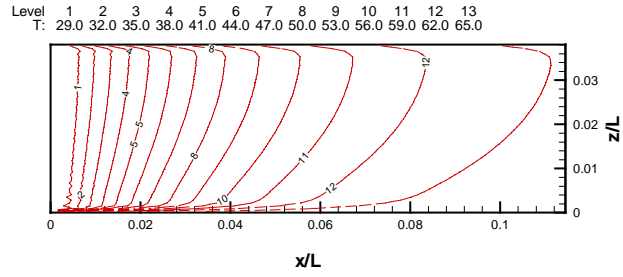


(a)

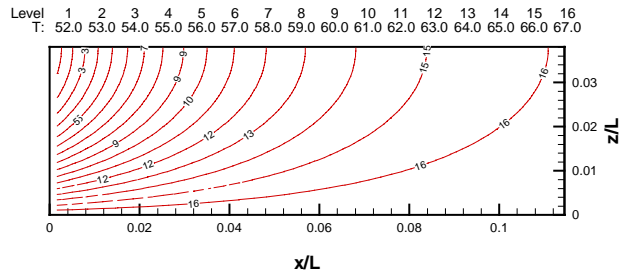


(b)

Figure C-8: Temperature in fluid (a) and in solid (b), $Q = 220\text{W}$, $Re_h = 362$, FVM.

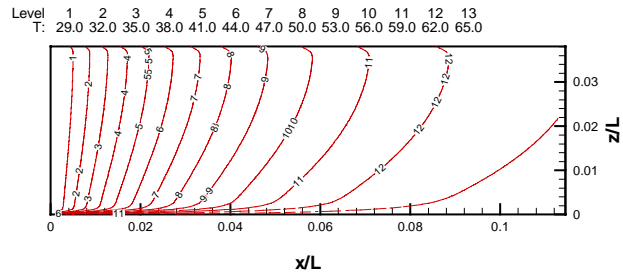


(a)

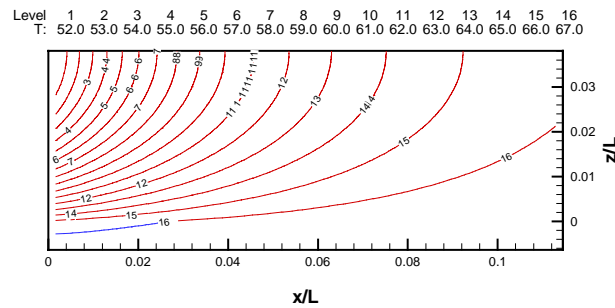


(b)

Figure C-9: Temperature in fluid (a) and in solid (b), $Q = 220\text{W}$, $Re_h = 530$, GM.

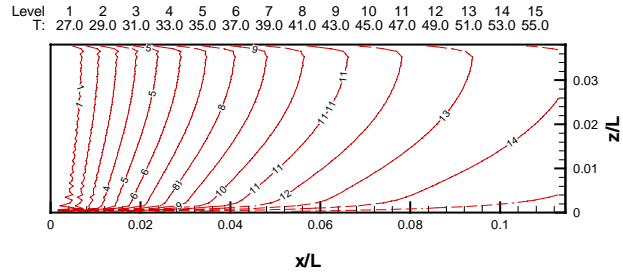


(a)

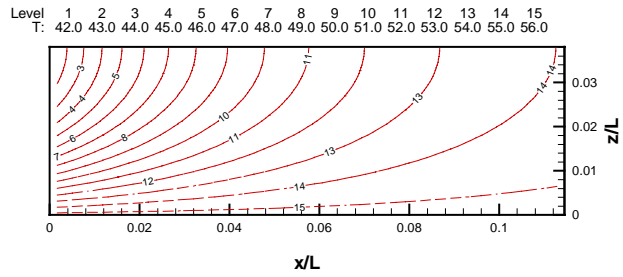


(b)

Figure C-10: Temperature in fluid (a) and in solid (b), $Q = 220\text{W}$, $Re_h = 531$, FVM.

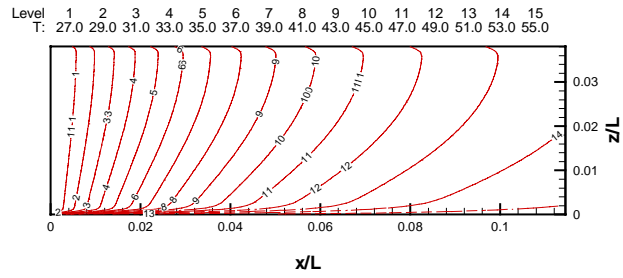


(a)

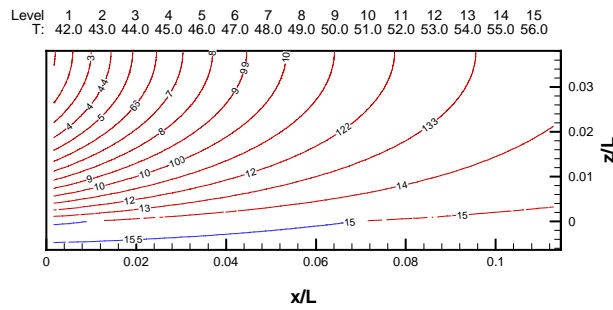


(b)

Figure C-11: Temperature in fluid (a) and in solid (b), $Q = 220\text{W}$, $Re_h = 747$, GM.

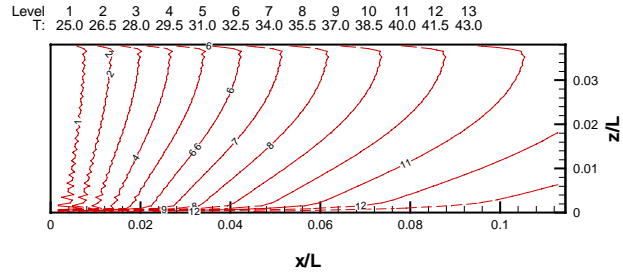


(a)

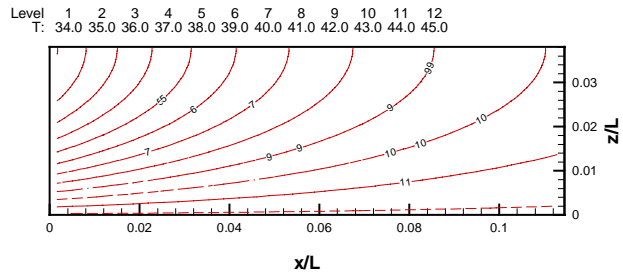


(b)

Figure C-12: Temperature in fluid (a) and in solid (b), $Q = 220\text{W}$, $Re_h = 749$, FVM.

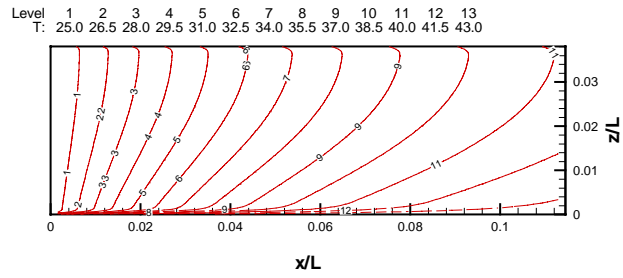


(a)

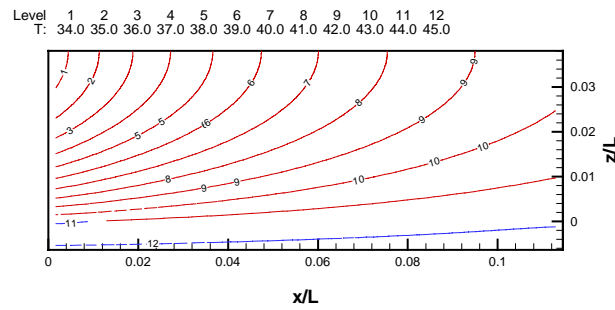


(b)

Figure C-13: Temperature in fluid (a) and in solid (b), $Q = 220\text{W}$, $Re_h = 1245$, GM.

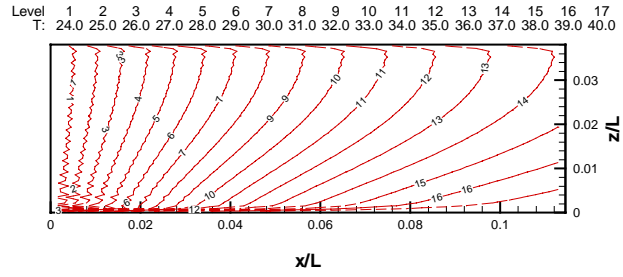


(a)

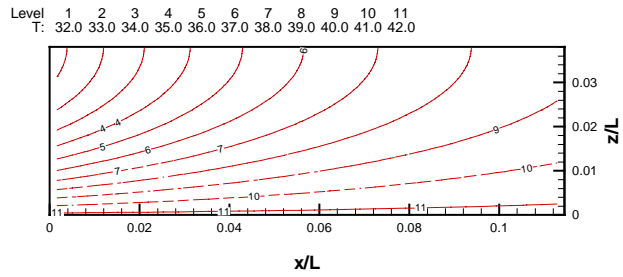


(b)

Figure C-14: Temperature in fluid (a) and in solid (b), $Q = 220\text{W}$, $Re_h = 1248$, FVM.

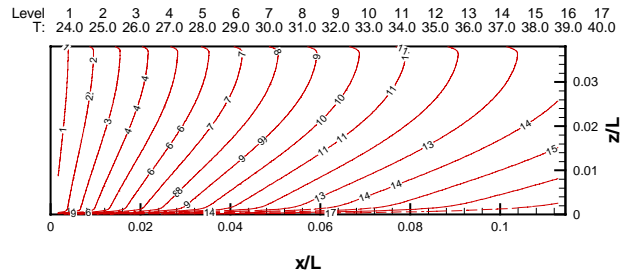


(a)

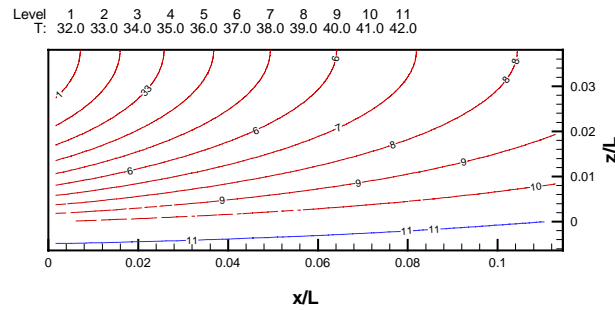


(b)

Figure C-15: Temperature in fluid (a) and in solid (b), $Q = 220\text{W}$, $Re_h = 1594$, GM.

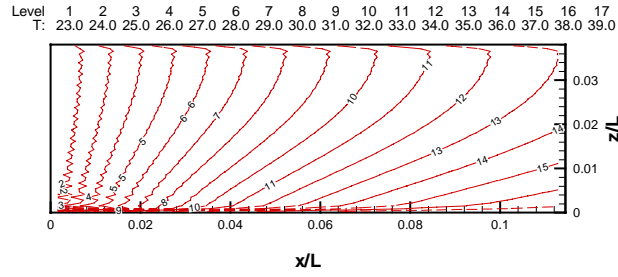


(a)

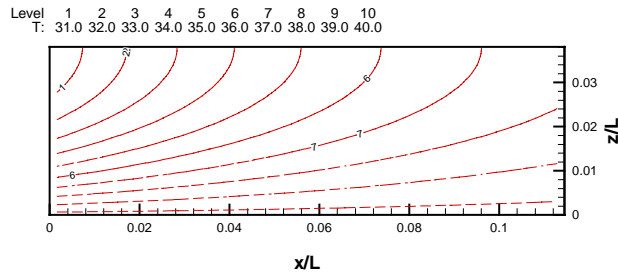


(b)

Figure C-16: Temperature in fluid (a) and in solid (b), $Q = 220\text{W}$, $Re_h = 1599$, FVM.

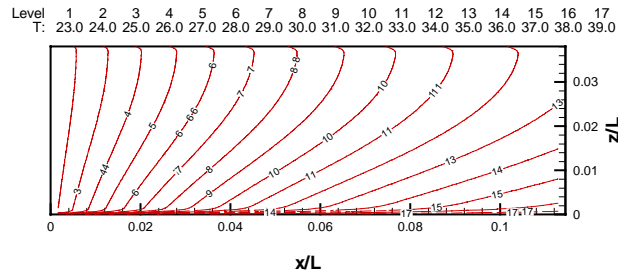


(a)

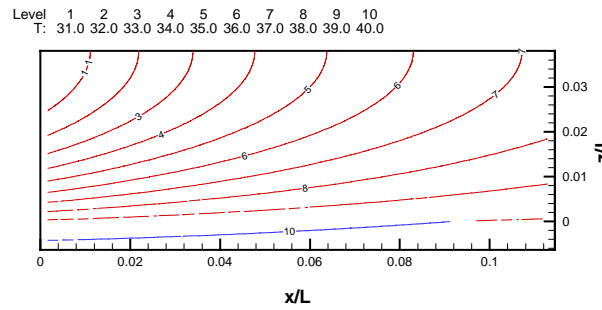


(b)

Figure C-17: Temperature in fluid (a) and in solid (b), $Q = 220\text{W}$, $Re_h = 1841$, GM.



(a)



(b)

Figure C-18: Temperature in fluid (a) and in solid (b), $Q = 220\text{W}$, $Re_h = 1847$, FVM.

APPENDIX D : Heat Transfer in Channel and Porous Media Flow

D.1 Velocity Fields

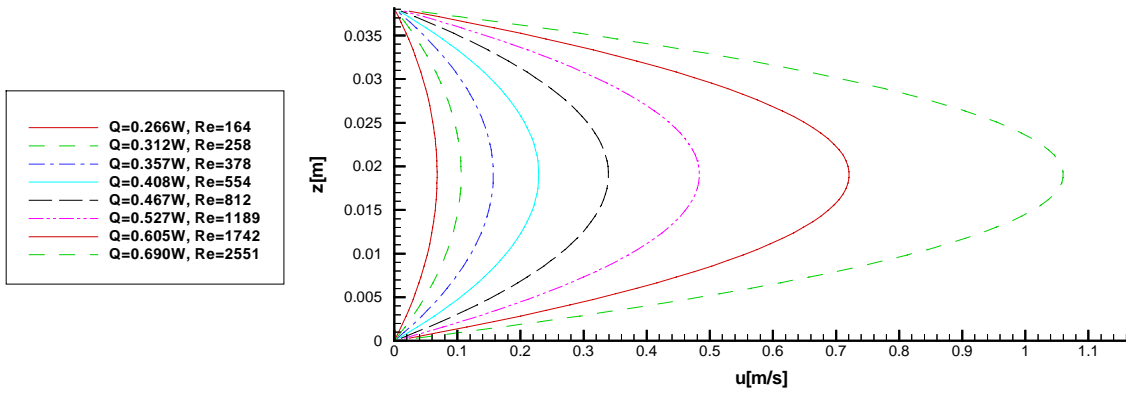


Figure D-1: Fluid velocity cross-section in channel flow.

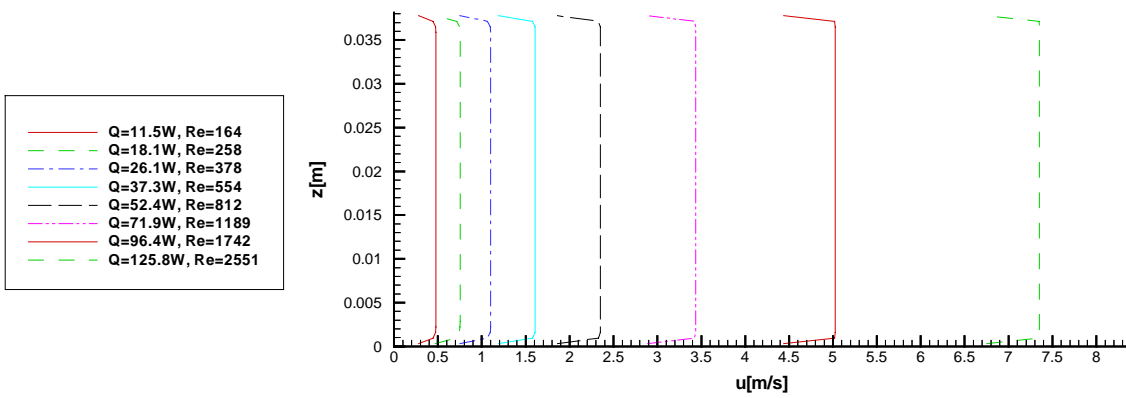


Figure D-2: Fluid velocity cross-section in porous media flow.

D.2 Temperature Fields

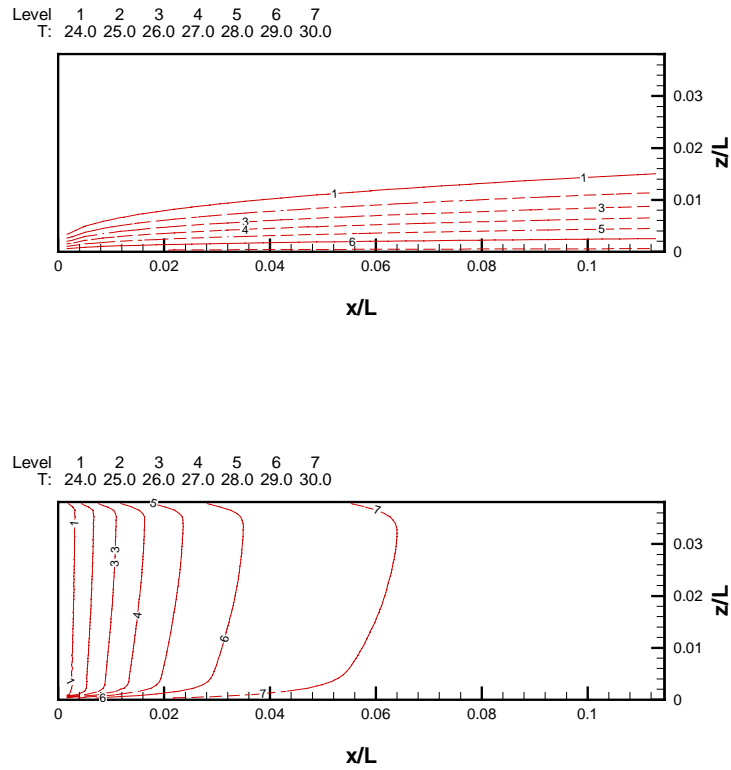


Figure D-3: Temperature field; channel flow (left), $Q = 0.266\text{W}$, $Re_h = 164$; porous media flow (right), $Q = 11.5\text{W}$, $Re_h = 164$.

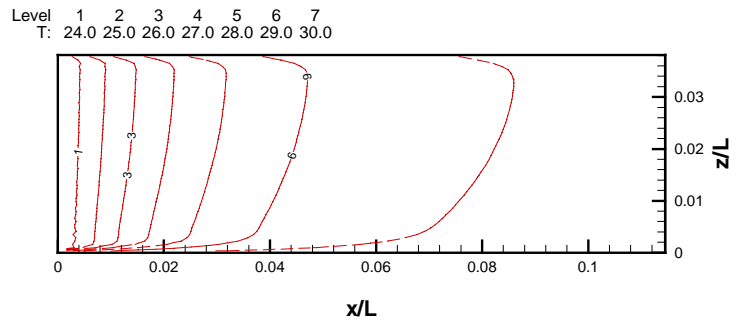
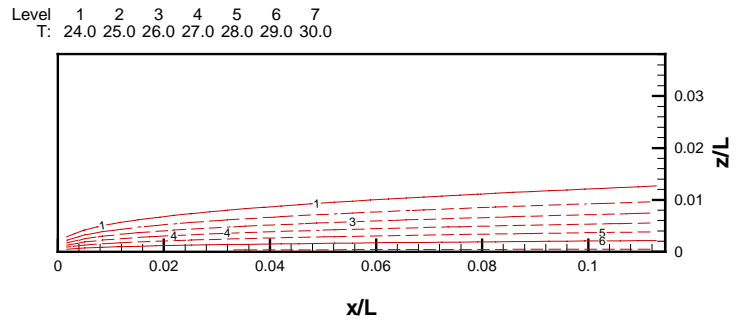


Figure D-4: Temperature field; channel flow (left), $Q = 0.312\text{W}$, $Re_h = 256$;
porous media flow (right), $Q = 18.1\text{W}$, $Re_h = 258$.

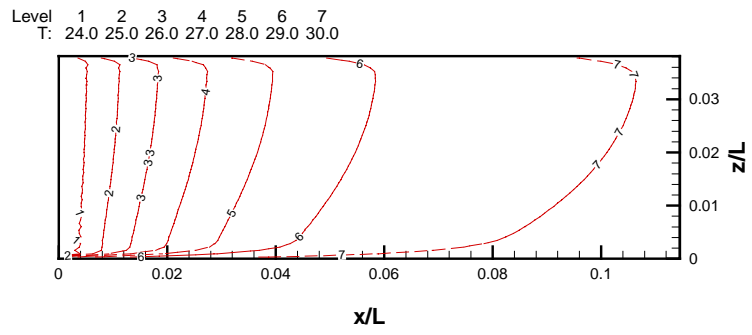
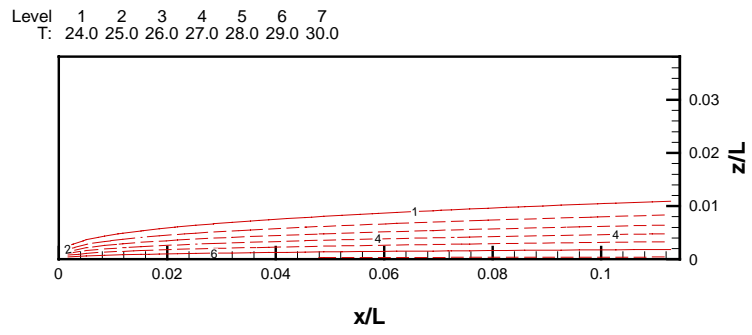


Figure D-5: Temperature field; channel flow (left), $Q = 0.358\text{W}$, $Re_h = 379$;
porous media flow (right), $Q = 26.1\text{W}$, $Re_h = 378$.

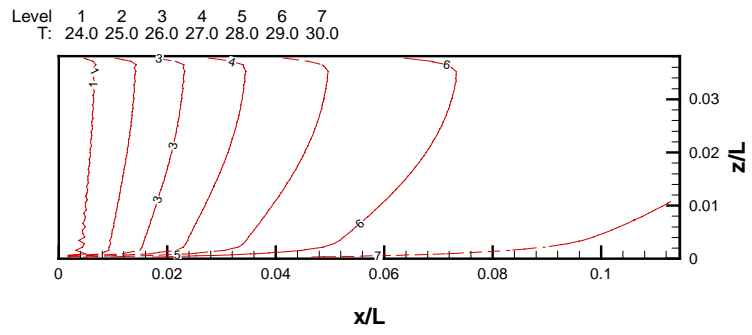
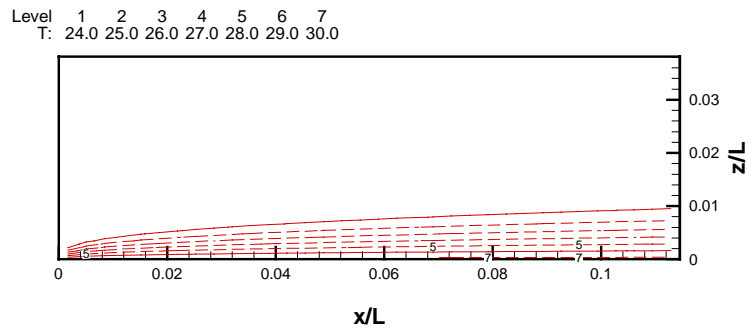


Figure D-6: Temperature field; channel flow (left), $Q = 0.408\text{W}$, $Re_h = 553$;
porous media flow (right), $Q = 37.3\text{W}$, $Re_h = 554$.

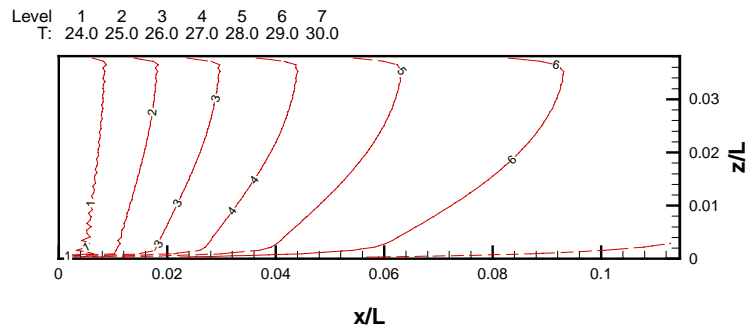
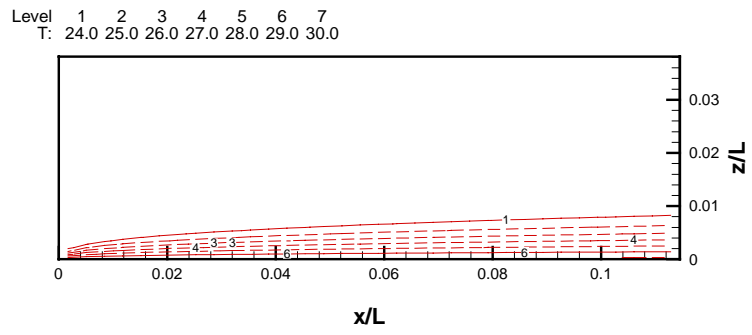


Figure D-7: Temperature field; channel flow (left), $Q = 0.467\text{W}$, $Re_h = 819$;
porous media flow (right), $Q = 52.4\text{W}$, $Re_h = 812$.

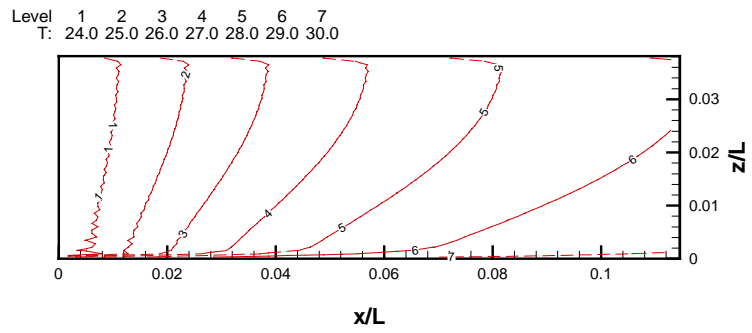
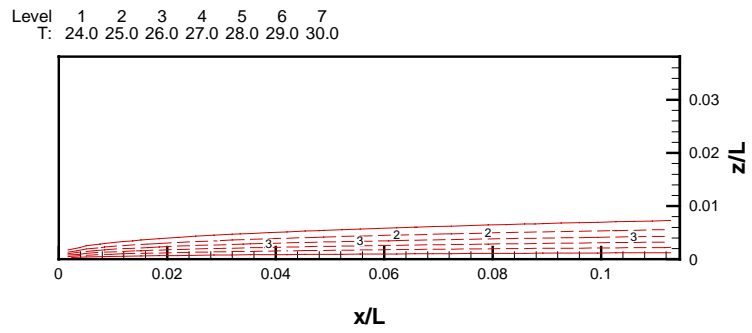


Figure D-8: Temperature field; channel flow (left), $Q = 0.527\text{W}$, $Re_h = 1167$; porous media flow (right), $Q = 71.9\text{W}$, $Re_h = 1189$.

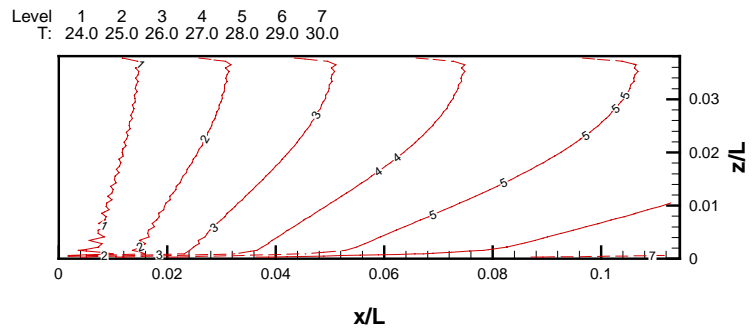
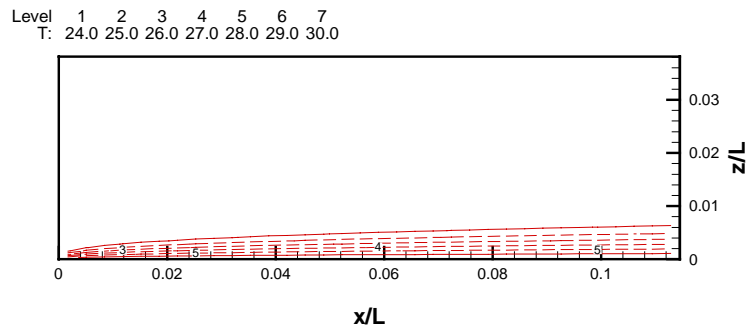


Figure D-9: Temperature field; channel flow (left), $Q = 0.605\text{W}$, $Re_h = 1741$; porous media flow (right), $Q = 96.4\text{W}$, $Re_h = 1742$.

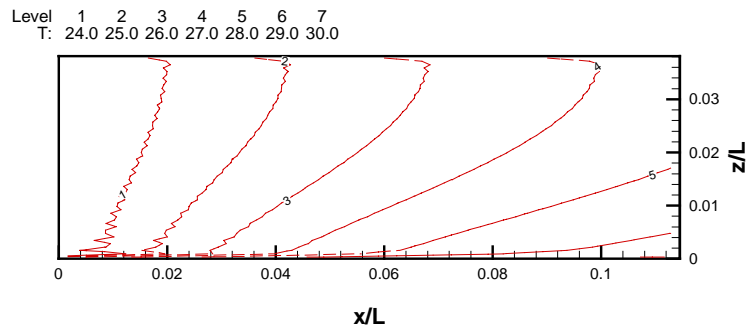
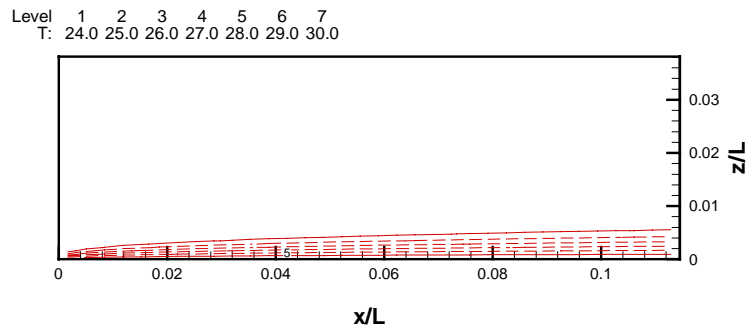


Figure D-10 : Temperature field; channel flow (left), $Q = 0.690\text{W}$, $Re_h = 2260$;
porous media flow (right), $Q = 125.8\text{W}$, $Re_h = 2551$.

References

- Adler, P.M., "Porous Media: Geometry and Transport", Butterworth-Heinemann, Stoneham, 1992.
- Al-Jamal, K., Khashashneh, H., "Experimental Investigation in Heat Transfer of Triangular and Pin Fins Arrays", Int. J. Heat and Mass Transfer, 34, pp. 159-162, 1998.
- Anderson, T.B., Jackson, R., "A Fluid Mechanical Description of Fluidized Beds", Int. Eng. Chem. Fundam., 6, pp. 527-538, 1967.
- Antonopoulos, K.A., "Prediction of Flow and Heat Transfer in Rod Bundles: Results", Ph.D. Thesis, Mechanical Engineering Department, Imperial College, London, UK, 1979.
- Barsamian, H.R., Hassan, Y.A., "Large Eddy Simulation of Turbulent Crossflow in Tube Bundles", Nuclear Engineering and Design Journal, Vol. 172, pp. 103-122, 1997.
- Bejan, A., "The Optimal Spacing for Cylinders in Crossflow Forced Convection", J. Heat Transfer, Vol. 117, pp. 767-770, 1995.
- Bejan, A., Sciubba, E., "The Optimal Spacing of Parallel Plates Cooled by Forced Convection", Int. J. Heat Mass Transfer, Vol. 35, No. 12, pp. 3529-3264, 1992.
- Catton, I., 1970, "Convection in a Closed Rectangular Region: The Onset of Motion", Trans. ASME, Feb., pp. 186-188.
- Catton, I., 1972, "Effect of Wall Conduction on the Stability of a Fluid in a Rectangular Region Heated from Below", Trans. ASME, Nov., pp. 446-452 .
- Dullien, F.A.L., "Porous Media Fluid Transport and Pore Structure", Academic Press, New York, 1979.
- Fabbri, G., "Optimum Performances of Longitudinal Convective Fins with Symmetrical and Asymmetrical Profiles", Int. J. Heat and Fluid Flow, Vol. 20, pp. 634-641, 1999.
- Ferziger, J.H., Perić, M., "Computational Method for Fluid Mechanics, Chapter 5: Solution of Linear Equation Systems". Springer Verlag, Berlin, pp. 85-127, 1996.
- Fujii, M., Fujii, T., Nagata, T., A Numerical Analysis of Laminar Flow and Heat Transfer of Air in an In-Line Tube Bank, Numerical Heat Transfer, Vol. 7, pp. 89-102, 1984.

- Horvat, A., Catton, I., "Development of an Integral Computer Code for Simulation of Heat Exchangers", The 8th Regional Meeting "Nuclear Energy in Central Europe", Portorož, Slovenia, 2001.
- Horvat, A., Rizzi, M., Catton, I., "Advanced Computational Methods in Heat Transfer VII: Numerical Investigation of Chip Cooling Using Volume Averaging Technique (VAT)", WIT Press, Southampton, UK, pp. 373-382, 2002.
- Horvat, A., Catton, I., "Modeling of Conjugate Heat Transfer Using Galerkin Approach", Procs. of Compact Heat Exchanger Symposium, Grenoble, 24. Aug., 2002.
- Howle, L.A., "A Comparison of the Reduced Galerkin and Pseudo-Spectral Methods for Simulation of Steady Rayleigh-Bénard Convection", Int. J. Heat Mass Transfer, Vol. 39, No. 12, pp. 2401-2407, 1996.
- Johnson, A.A., Tezduyar, T.E., Lion, J., "Numerical Simulations of Flows Past Periodic Arrays of Cylinders", Computational Mechanics, Vol. 11, pp. 371-383, 1983.
- Joseph, D.D., Nield, D.A., Papanicolaou, G., "Nonlinear Equation of Governing Flow in a Saturated Porous Medium", Water Resources Res., 18, pp. 1049-1052, 1982.
- Kays, W.S., London, A.L., "Compact Heat Exchangers", 3rd Ed., Krieger Publishing Company, Malabar, Florida, pp. 152-155, 1998.
- Kheifets, L.L., Neimark, A.V., "Multiphase Processes in Porous Media", Nadra, Moscow, 1982.
- Lauder, B.E., Massey, T.H., "The Numerical Prediction of Viscous Flow and Heat Transfer in Tube Banks", J. Heat Transfer, Vol. 100, pp. 565-571, 1978.
- Ledezma, G., Bejan, A., "Heat Sinks with Sloped Plate Fins in Natural and Forced Convection", Int. J. Heat Mass Transfer, Vol. 39, No. 9, pp. 1773-1783, 1996.
- Marle, C.M., "Ecoulements Monophasiques en Milieu Poreux", Rev. Inst. Francais du Petrole, 22, pp. 1471-1509, 1967.
- McDonough, J.M., Catton, I., "A Mixed Finite Difference-Galerkin Procedure for 2D Convection in a Square Box", Int. J. Heat Mass Transfer, 25, pp. 1137-1146, 1982.
- Nield, D.A., Bejan, A., "Convection in Porous Media: Mechanics of Fluid Flow through a Porous Medium", Springer-Verlag, New York, pp. 1-19, 1992.

- Noghrehkar, G.R., Kawaji, M., Chan, A.M.C., "Investigation of Two-Phase Flow Regimes in Tube Bundles under Cross-Flow Conditions", Int. J. Multiphase Flow, 25, pp. 857-874, 1999.
- Primak, A.V., Shcherban, A.N., Travkin, V.S., "Turbulent Transfer in Urban Agglomerations on the Basis of Experimental Statistical Models of Roughness Layer Morphological Properties", Trans. World Meteorological Org. Conf. on Air Pollution Modelling and its Application, WMO, Geneva, Switzerland, 2, pp. 259-266, 1986.
- Rizzi, M., Canino, M., Hu, K., Jones, S., Travkin, V., Catton, I., "Experimental Investigation of Pin Fin Heat Sink Effectiveness", Procs. of the 35th National Heat Transfer Conference, Anaheim, California, 2001.
- Sheherban, A.N., Primak, A.V., Travkin, V.S., "Mathematical Models of Flow and Mass Transfer in Urban Roughness Layer", Problemy Kontrolya i Zashchita Atmosfery or Zagryazneniya, 12, pp. 3-10, 1986.
- Slattery, J.C., "Flow of Viscoelastic Fluids Through Porous Media", AIChE J., 13, pp. 1066-1071, 1967.
- Travkin, V.S., Catton, I., "A Two Temperature Model for Fluid Flow and Heat Transfer in a Porous Layer", J. Fluid Engineering, Vol. 117, pp. 181-188, 1985.
- Travkin, V.S., Catton, I., "Models of Turbulent Thermal Diffusivity and Transfer Coefficients for a Regular Packed Bed of Spheres", Fundamentals of Heat Transfer in Porous Media, ASME HTD-193, pp. 15-23, 1992.
- Travkin, V.S., Catton, I., "Turbulent Transport of Momentum, Heat and Mass in a Two Levels Highly Porous Media", Procs. 10th Int. Heat Transfer Conference, 5, Chameleon Press, London, pp. 399-404, 1994.
- Travkin, V.S., Catton, I., "A Two-Temperature Model for Turbulent Flow and Heat Transfer in a Porous Layer", J. Fluids Eng., 117, pp. 181-188, 1995.
- Travkin, V., Catton, I., "Transport Phenomena in Heterogeneous Media Based on Volume Averaging Theory", Advans. Heat Trasfer, Vol. 34, pp. 1-143, 1999.
- Travkin, V.S., Catton, I., Gratton, L., "Single Phase Turbulent Transport in Prescribed Non-Isotropic and Stochastic Porous Media", Heat Transfer in Porous Media, ASME HTD-240, pp. 43-48, 1993.
- Travkin, V.S., Gratton, L., Catton, I., "A Morphological Approach for Two-Phase Porous Medium-Transport and Optimum Design Applications in Energy Engineering",

Procs. 12th Symp. Energy Engin. Sciences, Argonne National Laboratories, Conf.-9404137, pp. 48-55.

Travkin, V.S., Hu, K., Catton, I., "Turbulent Kinetic Energy and Dissipation Rate Equation Models for Momentum Transport in Porous Media", Procs. 3rd ASME/JSME Fluids Engineering Conf., FEDSM99-7275, ASME, San Francisco, 1999.

Whitaker, S., "Diffusion and Dispersion in Porous Media", AIChE J., 13, pp. 420-427, 1967.

Whitaker, S., "Flow in Porous Media: A Theoretical Derivation of Darcy's Law", Transport in Porous Media, Vol. 1, No. 1, pp. 3-25, 1986.

Yüncü, H., Anbar, G., "An Experimental Investigation on Performance of Rectangular Fins on a Horizontal Base in Free Convection Heat Transfer", Heat and Mass Transfer, Springer Verlag, 33, pp. 507-514, 1998.

Zolotarev, P.P., Redushkevich, LV., "The Equations for Dynamic Sorption in an Undeformed Porous Medium", Doklady Physical Chemistry, 182, pp. 643-646, 1968.

Žukauskas, A., "Heat Transfer from Tubes in Crossflow", Advances in Heat Transfer, Vol. 8, pp. 93-160, 1972.

Žukauskas, A., "Convective Heat Transfer in Cross Flow", Handbook of Single-Phase Convective Heat Transfer, Wiley & Sons, New York, 1987.

Žukauskas, A., Ulinskas, "Efficiency Parameters for Heat Transfer in Tube Banks", J. Heat Transfer Engineering, Vol. 5, No.1, pp. 19-25, 1985.